

# Chapter 6

## Distributions of Lyman $\alpha$ Lines

### 6.1 Introduction

Measuring the parameters of individual Lyman  $\alpha$  absorption lines reveals useful information about the physical conditions of single absorbing clouds. It is also illuminating to study the entire *population* of absorbers. By applying statistical analyses to the distributions of line parameters, an overall picture of the cloud properties may be formed.

Neutral hydrogen column densities of absorbers depend on a variety of factors:

- **The cloud mass.** The higher the mass, the more hydrogen is present, although this alone does not necessarily imply a higher  $N(\text{HI})$ .
- **The degree of ionisation.** A highly ionised cloud contains less neutral hydrogen than a less ionised cloud of the same mass. The ionisation level is dependent on the density of the cloud and the incident ionising flux. Also, if the cloud is large enough, the core may be shielded from ionising radiation by the surrounding regions, leaving it more neutral.
- **The cloud geometry.** The distribution of column density with impact parameter (the perpendicular distance between the cloud centre and the line of sight through it) depends on the shape of the cloud. For example, spherical clouds will show a monotonic decrease in  $N(\text{HI})$  with increasing impact parameter, while sheet-like clouds will have no such dependence.

The distribution of cloud column densities therefore provides information on all of these quantities, although extracting the details relies on interpretation and modelling.

The evolution of the cloud number density over time is dependent on whether the clouds are confined or not—and if so their method of confinement—and the interaction of the clouds with the evolving properties of the intergalactic medium and metagalactic ionising radiation. It is well-established that the number of observable Lyman  $\alpha$  clouds falls rapidly towards lower redshifts (Murdoch *et al.*, 1986), but whether this is a result of the clouds dispersing, becoming more ionised, or coalescing

to form other objects (*e.g.* star-forming galaxies) is not yet clear. A detailed study of the number density evolution may be able to identify further clues which can be used to constrain the various possibilities.

The velocity dispersion of absorbing clouds is a combination of thermal motions (indicating temperature) and macroscopic motions (see Equation 1.8). The distribution of velocity dispersions can supply constraints on cloud temperatures—and, through ionisation models, the degree of ionisation—and any regular motions, such as expansion.

In this Chapter, the distributions of the Lyman  $\alpha$  cloud parameters measured from the spectra of Q2206–199N (Pettini *et al.*, 1990), Q1101–264 and Q2348–147 are analysed. The data are compared with other data of similar spectral resolution from the literature and some conclusions based on the resulting body of work are drawn.

## 6.2 The Column Density Distribution

Carswell *et al.* (1984) were the first to attempt to fit a mathematical form to the column density distribution of Lyman  $\alpha$  lines. They noted that the exponential form used to fit the equivalent width distribution (Equation 1.11) did not give a satisfactory fit to their column density data for Q1101–264, observed at a spectral resolution of  $0.25 \text{ \AA}$  ( $20 \text{ km s}^{-1}$ ). Instead they fitted a power law of the form<sup>1</sup>

$$\frac{dN}{dN} = A_0 N^{-\beta}, \quad (6.1)$$

using the method of maximum likelihood (ML)<sup>2</sup>. Carswell *et al.*'s best estimate of the power law slope was  $\beta = 1.68 \pm 0.10$ . This was for the lines in their sample with  $\log N > 13.0$  and  $z_{\text{abs}} \sim 2.0$ . In the calculation of  $\beta$  it is essential to impose a lower limit on  $\log N$  because the line sample becomes incomplete at low column densities.

Incompleteness occurs because weak lines have small equivalent widths and become difficult to detect in data of limited S/N ratio. In noisy data the minimum detectable observed equivalent width  $W$  (and hence column density  $N$ ) is also relatively high. This is not a uniform effect, because the shape of absorption lines of identical  $W$  (governed by the velocity dispersion  $b$  for weak lines because they are on the linear part of the curve-of-growth) also plays a role in their detectability. Narrow lines are more likely to be detected than broad ones of equal  $W$  because, although the S/N ratio per pixel may be identical, a broad line covers more pixels and so has a lower integrated S/N level than a narrow line.

In determining the value of  $\beta$ , it is critical to make a good estimate of the completeness limit of the data, and to use only the data above that limit. The

<sup>1</sup>Equation 6.1 also appears as Equation 1.12.

<sup>2</sup>The ML method is often chosen for fitting distribution functions because it has maximal efficiency and does not require binning of data. All of the  $\beta$  estimates mentioned in this Section employed ML calculations.

inclusion of weaker lines, where only a fraction of the lines in a given  $N$  (or  $W$ ) range are detected, will bias the calculations and give spuriously low  $\beta$  values. Fortunately it is not difficult to determine a reasonable completeness limit simply by examining a plot of the column density distribution.

### Other Measurements of $\beta$

Since the first study of Carswell *et al.* (1984), there have been several other determinations of  $\beta$ . Atwood *et al.* (1985) used a  $0.5 \text{ \AA}$  ( $33 \text{ km s}^{-1}$ ) resolution spectrum of Q0420–388 to calculate  $\beta = 1.89 \pm 0.14$  for Lyman  $\alpha$  lines with  $14.0 < \log N < 16.7$  at  $z_{\text{abs}} \sim 2.9$ .

Carswell *et al.* (1987) combined their  $0.6 \text{ \AA}$  ( $35 \text{ km s}^{-1}$ ) resolution data for the QSO 2000–330 ( $z_{\text{abs}} \sim 3.6$ ) with those of Atwood *et al.* to form a larger line sample. With this, they found a value of  $\beta = 1.71$  (with no uncertainty quoted) above their adopted completeness limit of  $\log N = 13.75$ . However, a Kolmogorov goodness-of-fit test indicated that there was only a 0.04 probability of the observed distribution being generated by a simple power law. Carswell *et al.* noted that the column density distribution appeared to flatten at low values of  $\log N$  and found an adequate fit to the form:

$$\begin{aligned} d\mathcal{N} &\propto d\log N && \text{for } 13.75 < \log N < 14.35, \\ d\mathcal{N} &\propto N^{-1}d\log N && \text{for } \log N \geq 14.35. \end{aligned} \quad (6.2)$$

Such a “knee” in the  $\log N$  distribution would be a valuable tool for tracing the evolution of the Lyman  $\alpha$  clouds because the evolution of the knee would track the behaviour of  $N(\text{H I})$  for clouds of similar total masses at different redshifts. Under some reasonable assumptions, this allows the determination of relative cloud densities at any observed redshift.

Carswell *et al.* had some reservations about the reality of the knee in their  $\log N$  distribution. By applying a correction for line blanketing similar to the one described in Section 2.3.2, they found that a simple power law with index  $\beta = 1.76$  (no uncertainty quoted) had a 0.09 Kolmogorov probability of producing the observed distribution. This result, which should be a more accurate measure of the true distribution than the 0.04 probability fit of  $\beta = 1.71$ , is not strong evidence that a simple power law is inapplicable. Carswell *et al.* insisted, however, that their results provided at least tentative evidence for a knee in the  $\log N$  distribution.

Hunstead *et al.* (1987) reported a preliminary finding from independent observations of Q2000–330 at a similar resolution to the data of Carswell *et al.* that  $\beta = 1.57 \pm 0.05$  at  $z_{\text{abs}} \sim 3.6$ . A Kolmogorov goodness-of-fit test indicated a good fit to this power law, but no probability level was quoted. This was the first measurement to be inconsistent with any previous measurements, falling outside the  $1\sigma$  uncertainty estimates of Atwood *et al.* (1985), who found  $\beta = 1.89 \pm 0.14$  at  $z_{\text{abs}} \sim 2.9$ . This could have been taken as evidence for a steepening of the distribution function at lower redshifts, but no comments to this effect have been made in

the literature. The conflicting result of Carswell *et al.* for the same object shows that the formal uncertainties may well be underestimates because of the difficulties inherent in the spectral analysis procedures. In particular, the deblending of a dense Lyman  $\alpha$  forest with many saturated lines cannot be done with confidence unless several lines in the Lyman series can be seen for each absorbing cloud. This was the case for the data of both Carswell *et al.* and Hunstead *et al.*, but the data analysis procedures were different.

Hunstead (1988) presented a brief review of the  $\beta$  measurements to that date, including a discussion of the differences between the results of Hunstead *et al.* (1987) and Carswell *et al.* (1987). Where Carswell *et al.* found an apparent flattening of the distribution at  $\log N < 14.35$ , the result from Hunstead *et al.* (1987), although consistent with a simple power law, hinted at a flattening in the range  $14.0 < \log N < 15.4$ , with steeper slopes beyond both ends of this range. The differences were attributed to differences in the analysis procedures and the determinations of line parameters by the authors. Hunstead (1988) concluded that although evidence for a distribution more complex than a power law was weak, the prospects of using future data to uncover a more complex form and using it to study the evolution of Lyman  $\alpha$  clouds were good.

Carswell *et al.* (1991) (CLPW) published the first results on the column density distribution using high-resolution spectra. They observed Q1101–264 at a resolution of  $0.11 \text{ \AA}$  ( $9 \text{ km s}^{-1}$ ) and used a sample of 61 lines to calculate  $\beta = 1.7 \pm 0.1$  for lines with  $\log N > 13.0$  at  $z_{\text{abs}} \sim 2.0$ . They also stated that the power law was a good fit to the data, but gave no details.

### Constraining $\beta$ by Other Means

Barcons and Webb (1991) attempted to reconcile the differences between the rest equivalent width distributions of Lyman  $\alpha$  lines observed in intermediate-resolution spectra and those simulated from the column density distributions derived from high-resolution spectra. With the value  $\beta = 1.7$  taken from CLPW and other high-resolution work, Barcons and Webb produced simulated intermediate-resolution spectra and compared the  $W_0$  distribution with that seen in real data. Finding a significant difference, they postulated two possible explanations:

1. That the Lyman  $\alpha$  clouds are weakly clustered, with two-point correlation function<sup>3</sup>  $\xi \sim 0.5$  on velocity scales  $\lesssim 150 \text{ km s}^{-1}$ .
2. That the assumed value of  $\beta = 1.7$  was too high. An “extreme” value of  $\beta = 1.5$  was shown to produce a better fit to the  $W_0$  distribution—a value slightly below this would have provided the best fit, but this was not explored.

The second option was rejected out of hand as unrealistic and the result used to argue the case for small-scale clustering of Lyman  $\alpha$  clouds<sup>4</sup>.

<sup>3</sup>The two-point correlation function is described in detail in Section 7.2.

<sup>4</sup>The paper of Barcons and Webb (1991) is an important one in the study of Lyman  $\alpha$  cloud clustering properties, and is discussed again in this context in Section 7.1.1.

In a search for the Gunn-Peterson effect (see Section 1.4.1) in the spectrum of the  $z_{\text{em}} = 4.11$  QSO 0000–263, Webb *et al.* (1992) analysed the distribution of residual pixel intensities. At such a high redshift, there are vast numbers of Lyman  $\alpha$  lines and profile fitting is virtually impossible because of the line blending. Nevertheless, the distribution of pixel intensities can be modelled by combining the expected contributions from a given distribution of Lyman  $\alpha$  cloud column densities and a continuous Gunn-Peterson absorption component. Adopting a power law column density distribution with  $\beta = 1.7$  (from CLPW) implied a significant Gunn-Peterson effect, while assuming no Gunn-Peterson absorption required a flattening of the column density distribution below  $\log N = 13.75$  to  $\beta \sim 1.3$ . Webb *et al.* were unable to distinguish between these two possibilities with their data<sup>5</sup>.

### Recent Developments

Rauch *et al.* (1992) observed the  $z_{\text{em}} = 3.38$  QSO 0014+813 at a spectral resolution of  $0.4 \text{ \AA}$  ( $23 \text{ km s}^{-1}$ ). They found  $\beta = 1.72 \pm 0.05$  for the 189 lines stronger than their completeness limit of  $\log N = 13.3$ . A Kolmogorov test gave the probability of the distribution fitting this power law as 0.51, indicating a good fit (and hence not requiring a break or knee in the power law). By comparison with previous results (ignoring that of Hunstead *et al.*, 1987), Rauch *et al.* concluded the column density distribution maintained a power law shape with the same index over the redshift range  $2 \lesssim z_{\text{abs}} \lesssim 3.5$  for  $\log N \gtrsim 13.5$ .

In a re-analysis of the  $0.09 \text{ \AA}$  ( $7 \text{ km s}^{-1}$ ) resolution spectrum of Q2206–199N from Pettini *et al.* (1990) (PHSM), Rauch *et al.* (1993) found a value of  $\beta = 1.62 \pm 0.08$  at  $z_{\text{abs}} \sim 2.3$ . PHSM had not performed this calculation themselves, but I have done so using their original data in Section 6.2.1 below.

Petitjean *et al.* (1993b) assembled a sample of 10 QSOs observed at intermediate resolution ( $20\text{--}35 \text{ km s}^{-1}$ ) as well as data on Lyman limit and damped Lyman  $\alpha$  systems to explore the column density distribution over the range  $13.70 \leq \log N \leq 21.80$ . Their main result was to show that a single power law was a poor fit to the data over the entire  $\log N$  range, but they also demonstrated that a single power law for  $13.70 \leq \log N \leq 16.00$  (with best estimate  $\beta = 1.83 \pm 0.06$ ) gave a Kolmogorov probability of  $< 0.01$  of producing the observed distribution. They concluded that there was probably a flattening of the distribution at values of  $\log N < 14.0$ , but did not make a strong claim since their incompleteness limit was close to this value. Petitjean *et al.* then presented a four-component model, using models developed by Petitjean *et al.* (1992) and Petitjean *et al.* (1993a), to explain the structure seen in the distribution function, including two distinct populations of Lyman  $\alpha$  forest clouds.

Giallongo *et al.* (1993) observed the  $z_{\text{em}} = 3.27$  QSO PKS 2126–158 at a resolution of  $0.3 \text{ \AA}$  ( $14 \text{ km s}^{-1}$ ) and determined  $\beta = 1.76 \pm 0.08$  for all the Lyman  $\alpha$  lines

<sup>5</sup>Jenkins and Ostriker (1991) had performed a similar study on a sample of QSOs, but using an empirically determined equivalent width distribution in their simulations instead of a column density distribution. See Section 1.4.1 for details.

above their completeness limit of  $\log N = 13.3$ . They also pointed out that there appeared to be a systematic trend towards lower estimates of  $\beta$  when high column density lines were removed from several different samples collected from the literature. A careful inspection by Giallongo *et al.* of their spectrum suggested that most of the saturated Lyman  $\alpha$  lines with  $\log N \gtrsim 14.5$  could be unresolved blends. Using this as a justification for excluding such lines from their analysis, they concluded that the value  $\beta = 1.63 \pm 0.13$  for the sample with  $13.3 \leq \log N \leq 14.8$  was a better estimate of the true column density distribution. They then performed a similar analysis on a combined sample of lines from PKS 2126–158, Q0014+813 (Rauch *et al.*, 1992), and Q1101–264 (CLPW), finding a poor fit (Kolmogorov probability 0.02) to a power law with  $\beta = 1.74 \pm 0.01$  for all lines with  $\log N \geq 13.3$ , but a good fit (probability 0.72) with  $\beta = 1.53 \pm 0.02$  for the lines with  $13.3 \leq \log N \leq 14.8$ . Giallongo *et al.* concluded that the true value of  $\beta$  for Lyman  $\alpha$  forest clouds was more likely to be  $\sim 1.5$  than the  $\sim 1.7$  quoted by many previous authors, and it was certainly the case that  $\beta \sim 1.5$  below  $\log N \sim 15$ . This result was almost precisely what Barcons and Webb (1991) concluded must be true if the Lyman  $\alpha$  clouds are not weakly clustered on small scales—an option they rejected in their argument in favour of such clustering. It could also partially explain the observations of Webb *et al.* (1992) without invoking significant Gunn-Peterson absorption at  $z_{\text{abs}} \sim 4$ .

Cristiani *et al.* (1995) supported the findings of Giallongo *et al.* when they observed the  $z_{\text{em}} = 3.66$  QSO 0055–269 at a resolution of  $0.3 \text{ \AA}$  ( $14 \text{ km s}^{-1}$ ). They found  $\beta = 1.80 \pm 0.03$  with a full sample of Lyman  $\alpha$  lines above their completeness limit of  $\log N = 13.3$ , but this was a poor fit to the data. When they restricted the range to  $13.3 \leq \log N \leq 14.5$ , the value became  $\beta = 1.38 \pm 0.08$ . Cristiani *et al.* then combined their data with those from the three objects analysed by Giallongo *et al.* and Q2206–199N (Rauch *et al.*, 1993). Lines with  $\log N \geq 13.3$  gave a poor fit to a single power law with  $\beta = 1.74 \pm 0.04$ , but restricting the sample to  $13.3 \leq \log N \leq 14.5$  gave a good fit to a power law with  $\beta = 1.42 \pm 0.05$ .

Songaila *et al.* (1995) presented data from the  $z_{\text{em}} = 3.286$  QSO 0302–003 taken with the HIRES echelle spectrograph on the 10 m Keck Telescope, at a resolution of  $0.13 \text{ \AA}$  ( $8 \text{ km s}^{-1}$ ). With the high S/N ratio of their data, the completeness limit is  $\log N \sim 12.3$ . They found  $\beta = 1.46$  (no uncertainty quoted) for the lines with  $12.3 \leq \log N \leq 14.5$ , showing that the column density distribution maintains a good fit to a power law down to at least  $\log N \sim 12.3$ .

Several published estimates of  $\beta$  are summarised in Table 6.2 in Section 6.2.2, together with the measurements from this work.

### 6.2.1 Determinations of $\beta$

The column density distributions of the Lyman  $\alpha$  clouds observed in the high-resolution UCLES data of the QSOs 2206–199N, 1101–264, and 2348–147 were investigated. The value of  $\beta$  was determined for various  $\log N$ -limited samples of clouds for each object using the maximum likelihood method of Section 2.3.2. The results are shown in Table 6.1.

**Table 6.1** Results of ML calculations for the column density distribution in the three high-redshift QSOs. The parameters  $A_0$  and  $\beta$  are as defined in Equation 6.1. The value  $\beta'$  is the estimated value of  $\beta$  after correction for the line blanketing effect, described in Section 6.2.1. The corresponding  $A'_0$  values have been omitted for space reasons.

Object	log $N$ range	No. lines	$A_0$	$\beta$	$\beta'$	
Q2206–199N	12.50–14.25	41	$3.3 \times 10^1$	$1.03 \pm 0.13$	$1.03 \pm 0.13$	
	12.75–14.25	39	$3.9 \times 10^4$	$1.26 \pm 0.16$	$1.26 \pm 0.16$	
	( $z_{\text{abs}} =$	13.00–14.25	32	$1.5 \times 10^7$	$1.45 \pm 0.22$	$1.45 \pm 0.22$
	2.07–2.56)	13.25–14.25	24	$3.2 \times 10^{11}$	$1.77 \pm 0.33$	$1.77 \pm 0.33$
	13.50–14.25	14	$7.7 \times 10^{13}$	$1.94 \pm 0.57$	$1.94 \pm 0.57$	
Q1101–264	12.25–14.50	70	$1.5 \times 10^3$	$1.15 \pm 0.08$	$1.16 \pm 0.08$	
	12.50–14.50	65	$7.4 \times 10^4$	$1.28 \pm 0.10$	$1.29 \pm 0.09$	
	( $z_{\text{abs}} =$	12.75–14.50	60	$8.5 \times 10^7$	$1.50 \pm 0.12$	$1.51 \pm 0.12$
	1.79–2.15)	13.00–14.50	47	$2.9 \times 10^{10}$	$1.69 \pm 0.17$	$1.70 \pm 0.16$
	13.25–14.50	34	$2.4 \times 10^{14}$	$1.97 \pm 0.25$	$2.00 \pm 0.24$	
Q2348–147	12.25–15.00	330	$7.3 \times 10^3$	$1.16 \pm 0.03$	$1.18 \pm 0.03$	
	12.50–15.00	324	$5.0 \times 10^5$	$1.29 \pm 0.04$	$1.32 \pm 0.03$	
	12.75–15.00	284	$1.1 \times 10^7$	$1.39 \pm 0.04$	$1.42 \pm 0.04$	
	( $z_{\text{abs}} =$	13.00–15.00	240	$5.8 \times 10^8$	$1.51 \pm 0.05$	$1.55 \pm 0.05$
	2.07–2.94)	13.25–15.00	179	$5.1 \times 10^9$	$1.58 \pm 0.07$	$1.62 \pm 0.07$
	13.50–15.00	127	$7.8 \times 10^{10}$	$1.66 \pm 0.10$	$1.69 \pm 0.10$	

For each object, a fixed upper limit on log  $N$  was adopted. There were lines stronger than the chosen limits, but such lines were saturated<sup>6</sup>. Saturated lines in the spectra of Q2206–199N and Q1101–264 could not have their column densities determined accurately, so the line samples are effectively incomplete at high column densities. Some saturated lines in the spectrum of Q2348–147 have corresponding Lyman  $\beta$  lines available to constrain the line parameters. However, because Lyman  $\beta$  data are not available for all the saturated lines there is still some incompleteness at log  $N > 15.0$ . To avoid biasing the calculations of  $\beta$ , the upper log  $N$  limits were restricted to the smallest integral multiple of 0.25 (corresponding to the bin sizes in Figures 6.1, 6.2, and 6.3) which included all the non-saturated lines. The ML calculations correctly accounted for the upper cut-offs when estimating  $\beta$ .

Histograms of the column density distributions for each of the three QSOs are shown in Figures 6.1, 6.2, and 6.3. For each object, a correction was made for the line blanketing effect. This decreases the numbers of weak lines seen in the spectrum because of obscuration by stronger lines. The effect is discussed in Section 2.3.2 and a formula for estimating a corrected value for  $\mathcal{N}$  in each bin is given by Equation 2.8. The corrected estimates for  $\mathcal{N}$  are shown in the Figures as dotted histograms.

Quantitative estimates of the value of  $\beta$  after correction for line blanketing were also made, following the procedure described in Section 2.3.2. These estimates are

<sup>6</sup>Saturated lines are noted in the line lists given in Appendix B.

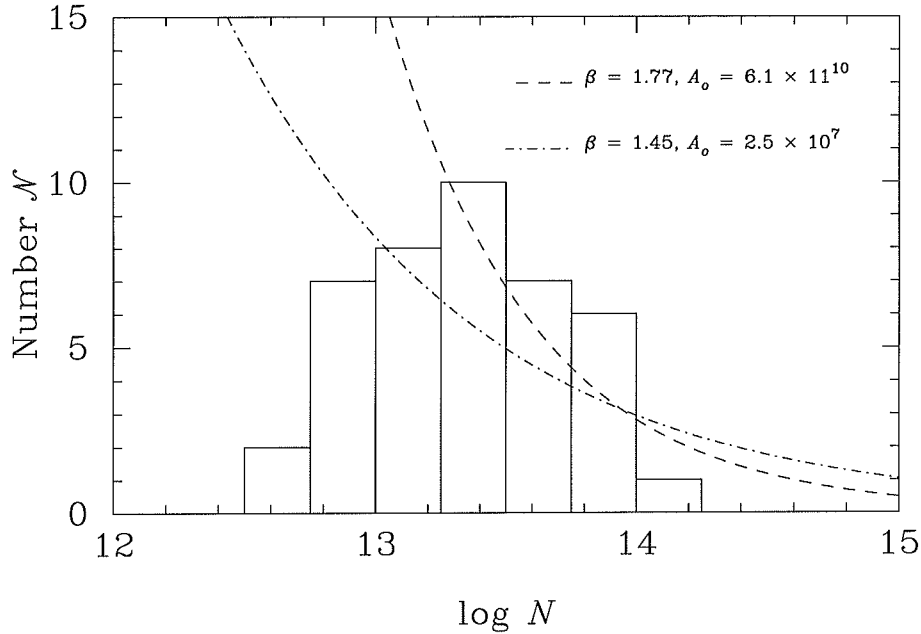


**Figure 6.1** Number density histogram of the  $\log N$  values for the Q2206–199N Lyman  $\alpha$  lines. The histogram shows the actual number of lines observed in each bin; the numbers after correction for the blanketing effect, given by Equation 2.8, are the same as the actual numbers. The curved lines show two of the ML parameter fits to the observed distribution (solid histogram) from Table 6.1.

shown in the  $\beta'$  column of Table 6.1.

The results of the column density distribution calculations for each of the three QSOs are discussed individually below.

### Q2206–199N

The line blanketing correction calculations for Q2206–199N do not result in any change of the histogram shown in Figure 6.1. This also means that the value of  $\beta'$  is identical to the value of  $\beta$  for each  $\log N$  range. The reason the blanketing correction produces no changes is that the numbers of lines in each  $\log N$  bin are too small to be increased when Equation 2.8 is applied and the result rounded off. Line blanketing is therefore an insignificant effect in the sample of lines from the Q2206–199N spectrum.

The uncertainties in the calculations of  $\beta$  for this object are large. An examination of Figure 6.1 shows the paucity of lines in the spectrum. The power law fits shown in the Figure do not appear to be particularly good (note that the dashed line is a fit only to the data with  $\log N > 13.25$  and the dot-dashed line a fit to the data with  $\log N > 13.0$ ), but the counts in the bins are too small to reach any conclusions on the acceptability of the power law form.

From Figure 6.1, and assuming a power law is a valid description of the  $\log N$

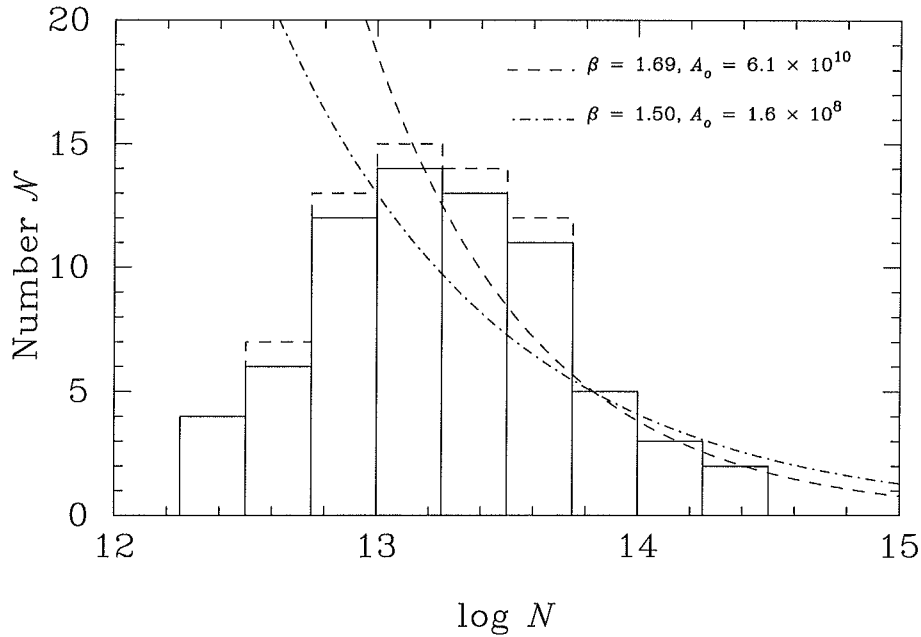


**Figure 6.2** Number density histogram of the  $\log N$  values for the Q1101–264 Lyman  $\alpha$  lines. The solid histogram shows the actual number of lines observed in each bin; the dashed histogram shows the number after correction for the blanketing effect, given by Equation 2.8. The curved lines show two of the ML parameter fits to the observed distribution (solid histogram) from Table 6.1.

distribution (at least for lines with  $\log N > 13.0$ ), it appears that incompleteness is present for lines with  $\log N \lesssim 13.25$ . This limit corresponds to a rest equivalent width limit of  $W_0 \sim 80 \text{ m}\text{\AA}$ , for  $b > 10 \text{ km s}^{-1}$ , consistent with the limit inferred from the measurement of the absorption features. The completeness limit is higher than those for Q1101–264 and Q2348–147 because of the relatively poor S/N ratio of the Q2206–199N data. Adopting this completeness limit, the best estimate of the column density distribution power law index is  $\beta = 1.77 \pm 0.33$ .

### Q1101–264

In the case of Q1101–264, the line blanketing correction makes only small changes to the  $\log N$  distribution histogram shown in Figure 6.2. The corrected counts in five bins are one higher than the raw counts. This correction also has only a minor effect on the power law index— $\beta'$  is greater than  $\beta$  by only  $\sim 0.1$  times the uncertainty estimate for each  $\log N$  range.

From an inspection of Figure 6.2, it appears the completeness limit for the Lyman  $\alpha$  lines in the Q1101–264 spectrum is  $\log N \sim 13.0$ . This limit corresponds to a rest equivalent width limit of  $W_0 \sim 50 \text{ m}\text{\AA}$ , for  $b > 10 \text{ km s}^{-1}$ , equal to the  $W_0$  completeness limit inferred from the line measurements. Kolmogorov goodness-of-fit tests were applied to determine which  $\log N$  cut-off produces the best fit to a single

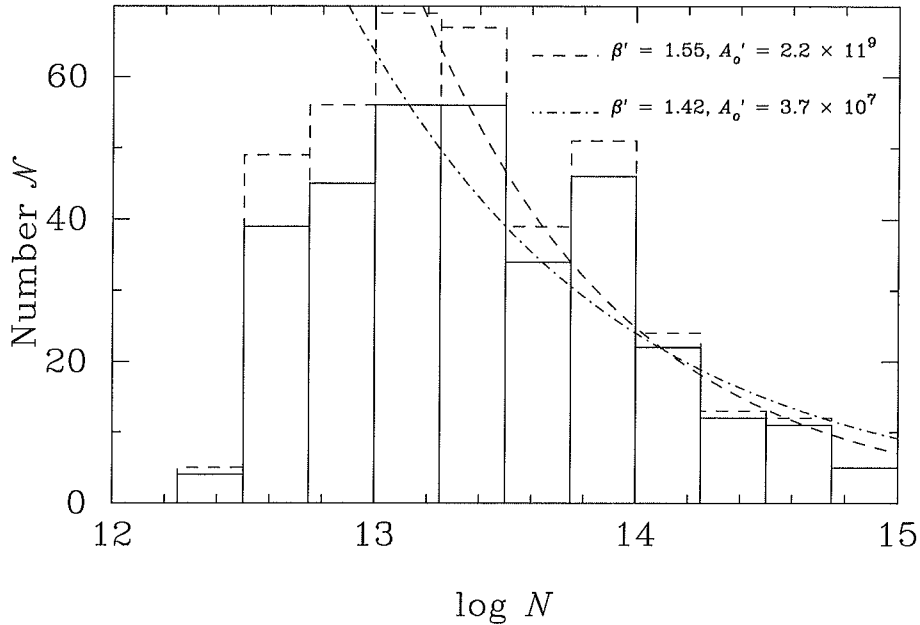


**Figure 6.3** Number density histogram of the  $\log N$  values for the Q2348–147 Lyman  $\alpha$  lines. The solid histogram shows the actual number of lines observed in each bin; the dashed histogram shows the number after correction for the blanketing effect, given by Equation 2.8. The curved lines show two of the ML parameter fits to the observed distribution (solid histogram) from Table 6.1.

power law. The  $\log N > 13.0$  cut-off gave a probability of 0.95 that the data were drawn from the power law distribution with parameters as given in Table 6.1, while the  $\log N > 12.75$  cut-off gave a probability of 0.78. These results indicate that the power law fits are good fits to the data, but the number of lines is not large so the probabilities are somewhat unreliable.

If a completeness limit of  $\log N > 13.0$  is assumed, the best estimate for the value of  $\beta$  is  $1.69 \pm 0.17$ . Higher Kolmogorov probabilities can be produced by raising the adopted completeness limit further, but this becomes artificial because the range over which the power law is fitted becomes small.

### Q2348–147

The Q2348–147 spectrum contains many more absorption lines than those of the other two objects. Consequently, the uncertainties in the values of  $\beta$  are relatively small. Also, the line blanketing correction gives substantial changes to the number of lines per  $\log N$  bin in Figure 6.3. The column density power law index after correction is increased over the uncorrected value of  $\beta$  by  $\sim$  half the formal uncertainty for each  $\log N$  range.

The completeness limit for this spectrum is  $\log N \sim 13.0$ . Again this corresponds to the known rest equivalent width completeness limit of  $W_0 \sim 50 \text{ m}\text{\AA}$ , for  $b > 10 \text{ km s}^{-1}$ . In this case there are enough lines for a Kolmogorov test to be a useful

indicator of the goodness-of-fit. The probability that the lines with  $\log N > 13.0$  are drawn from the power law distribution given in Table 6.1 is 0.06, indicating a marginal but acceptable fit. The Kolmogorov probability for the same  $\log N$  limit after correction for the line blanketing effect is considerably higher at 0.36. This indicates that a power law distribution which is not corrected for line blanketing will give lower goodness-of-fit probabilities than might be expected, similar to the finding of Carswell *et al.* (1987) discussed in Section 6.2.

In this case, it is certainly better to give the value of  $\beta' = 1.55 \pm 0.05$  for lines above the completeness limit after correction for the line blanketing effect as the best estimate of the column density power law index.

### 6.2.2 Discussion of $\beta$ Results

The best estimates of  $\beta$  for each of the three objects studied (given in Table 6.2, along with estimates from other authors) are consistent with each other, indicating no obvious change in the power law slope over the redshift range covered ( $1.8 < z_{\text{abs}} < 2.9$ ).

The  $\beta$  estimates are not, however, consistent with all of the previous values. The tightest constraint is placed by the Q2348–147 data, giving  $\beta = 1.55 \pm 0.05$ , after correction for line blanketing. This is lower than the generally accepted value of  $\sim 1.7$ , with which most published values have been consistent.

Giallongo *et al.* (1993) pointed out that it may not be valid to include lines with  $\log N \gtrsim 15$  in an analysis of the column density distribution because an inspection of their data suggested that most such lines could really be unresolved blends. They produced a best estimate of  $\beta = 1.53 \pm 0.02$  using a sample of lines from three QSO spectra. In this analysis, lines with  $\log N > 15$  were excluded for completeness reasons, and the best estimate of  $\beta$  is in agreement with the value of Giallongo *et al.*. These are also consistent with the value of Hunstead *et al.* (1987), alone amongst earlier work. Hunstead *et al.* made careful use of transitions in the Lyman series other than Lyman  $\alpha$  to constrain fits to saturated Lyman  $\alpha$  lines in their spectrum of Q2000–330. This technique allows the deconvolution of blends which would appear as single saturated lines in Lyman  $\alpha$  alone, so their work may be considered more accurate than other studies including lines with  $\log N \geq 15$ .

Cristiani *et al.* (1995) also reported a better fit to a power law when high column density clouds were excluded and Songaila *et al.* (1995) showed that a power law fit extended from  $\log N = 14.5$  to column densities as low as  $\log N = 12.3$ . The best estimates of these authors were both slightly lower than that of Giallongo *et al.* and those reported here. Some of this discrepancy may be explained by the line blanketing effect.

### The Effect of Line Blanketing

For all three objects, the line blanketing correction was found not to compensate fully for the lack of lines detected below the completeness limits. This was also

**Table 6.2** Collected estimates of  $\beta$  from this work and other references.

Object	Resolution ( $\text{km s}^{-1}$ )	$z_{\text{abs}}$ range	$\log N$ range	No. Lines	$\beta$	Ref. <sup>8</sup>
Q1101–264	20	1.87–2.14	13.00–16.00 <sup>1</sup>	45	$1.68 \pm 0.10$	a
Q0420–388	33	2.73–3.11	14.00–16.70 <sup>1</sup>	38	$1.89 \pm 0.14$	b
Q2000–330	35	3.30–3.75	13.75–16.50 <sup>1</sup>	60	$1.71^2$	c
Q2000–330	33	3.43–3.78	13.25–16.50 <sup>1</sup>	149	$1.57 \pm 0.05$	d
Q1101–264	9	1.84–2.15	13.00–16.20 <sup>1</sup>	61	$1.7 \pm 0.1$	e
Q0014+813	23	2.70–3.38	13.30–15.70 <sup>1</sup>	189	$1.72 \pm 0.06$	f
Q2206–199N	7	2.07–2.56	13.30–16.00 <sup>1</sup>	55	$1.62 \pm 0.08$	g
10 objects	20–35	1.89–3.70	13.70–16.00 <sup>3</sup>	474	$1.83 \pm 0.06$	h
PKS 2126–158	14	2.91–3.17	13.30–17.00 <sup>1</sup>	71	$1.76 \pm 0.08$	j
			13.30–14.80 <sup>4</sup>	68	$1.63 \pm 0.13$	
3 objects <sup>5</sup>	9–23	1.84–3.30	13.30–17.00 <sup>1</sup>	285	$1.74 \pm 0.01$	
			13.30–14.80 <sup>4</sup>	275	$1.53 \pm 0.02$	
Q0055–269	14	2.96–3.54	13.30–16.50 <sup>1</sup>	178	$1.80 \pm 0.03$	k
			13.30–14.50 <sup>4</sup>	170	$1.38 \pm 0.08$	
5 objects <sup>6</sup>	7–23	1.84–3.54	13.30–17.00 <sup>1</sup>	507	$1.74 \pm 0.04$	
			13.30–14.50 <sup>4</sup>	464	$1.42 \pm 0.05$	
Q0302–003	8	? <sup>7</sup> –3.2	12.30–14.50 <sup>4</sup>	? <sup>7</sup>	1.46	l
Q2206–199N	7	2.07–2.56	13.25–14.25 <sup>4</sup>	24	$1.77 \pm 0.33$	m
Q1101–264	7	1.79–2.15	13.00–14.50 <sup>4</sup>	47	$1.69 \pm 0.17$	
Q2348–147	7	2.07–2.94	13.00–15.00 <sup>4</sup>	252	$1.55 \pm 0.05$	

Notes:

<sup>1</sup> The upper limit on  $\log N$  is an indication of the largest column density line seen in the spectrum. In practice, no lines above this limit were excluded from the sample, because none were detected.<sup>2</sup> This value refers to the combined line sample of the two objects of Carswell *et al.* (1987) and Atwood *et al.* (1985). No uncertainty was given for this value.<sup>3</sup> This upper limit is a cut-off imposed by the authors. They had data extending to  $\log N \sim 21.5$ , but were investigating the fit of a double power law, broken at  $\log N = 16.0$ . See Section 6.2 for details.<sup>4</sup> Upper limit is a cut-off above which there are lines detected, but these lines are saturated and so accurate  $\log N$  values cannot be determined.<sup>5</sup> Sample included Q0014+813 (Rauch *et al.*, 1992), Q1101–264 (CLPW), and PKS 2126–158.<sup>6</sup> Sample included the three objects listed under <sup>5</sup>, plus Q2206–199N (Rauch *et al.*, 1993), and Q0055–269.<sup>7</sup> The numbers indicated by question marks cannot be determined from the cited reference. The reference cites a more detailed paper, in preparation, which should contain this information.<sup>8</sup> References: (a) Carswell *et al.* (1984). (b) Atwood *et al.* (1985). (c) Carswell *et al.* (1987). (d) Hunstead *et al.* (1987). (e) CLPW. (f) Rauch *et al.* (1992). (g) Rauch *et al.* (1993). (h) Petitjean *et al.* (1993b). (j) Giallongo *et al.* (1993). (k) Cristiani *et al.* (1995). (l) Songaila *et al.* (1995). (m) This work.

the case for the CNQ (Section 2.3.2), and similarly here it is concluded that the incompleteness is caused mostly by either S/N ratio or line blending effects. It may be that the fall-off in line density at low column densities partially reflects a real feature of the  $\log N$  distribution, but S/N effects and line blanketing will still cause some incompleteness.

By comparing the effects of the line blanketing corrections between the three objects, it can be seen that they become more significant with larger line samples. Analysing the differences for samples of different numbers of lines would be a complex procedure, perhaps requiring detailed simulations. However, it appears that for samples of  $\gtrsim 1000$  lines the corrected value  $\beta'$  would be greater than the uncorrected value  $\beta$  by an amount larger than the uncertainty estimate. No samples assembled so far are of this size, but future calculations combining the line lists of several objects (which may not be too far distant, with the advent of the 10 m Keck Telescope) will need to address this problem.

In the case of Q2348–147, correction for the line blanketing effect also made a simple power law a significantly better fit to the column density distribution. (It made no difference to the Q2206–199N result, and judging the significance for the Q1101–264 data is difficult because of the small line sample.) Since a similar result was found by Carswell *et al.* (1987), it seems probable that not correcting for line blanketing could cause a power law distribution to appear to be some more complex form. Line blanketing has a greater effect on lines with smaller column densities, so the overall effect would be an apparent flattening of the distribution at low values of  $\log N$ . This is precisely what was observed by Carswell *et al.*, prompting them to propose a distribution with a conspicuous “knee”, and was also seen by Petitjean *et al.* (1993b). The results of the present study indicate that caution must be exercised, and line blanketing corrected for, before invoking such a complication, although they do not rule out the possibility of a knee in the distribution.

It should be noted that the result of Webb *et al.* (1992), which implied a flattening of the column density distribution below  $\log N = 13.75$  (assuming no Gunn-Peterson absorption at  $z_{\text{abs}} \sim 4$ ) using a different analysis method, may also be affected by line blanketing. It is not clear how well the model used by Webb *et al.* simulated and accounted for the effects of line blanketing. If it did not, then their result may be partially explained by this effect.

Although correcting for line blanketing leads to a better fit to a single power law in several cases, it does not change the value of  $\beta$  greatly. The early determinations of  $\beta \sim 1.7$  were more biased by the inclusion of high column density lines than line blanketing, and it has been shown that blanketing is not responsible for the significantly lower values of  $\beta$  found here and by Giallongo *et al.* (1993). Giallongo *et al.* stated that they did not correct for line blanketing, but from their own estimates and the calculations reported here, it is likely that their value of  $\beta = 1.53 \pm 0.02$  would become  $1.54\text{--}1.55 \pm 0.02$  after correction, still consistent with the Q2348–147 measurement.

The measurements of Cristiani *et al.* (1995), however, are significantly lower than  $\beta = 1.5$ . In this case the object is at a very high redshift ( $z_{\text{em}} = 3.66$ ) and

the line density in the spectrum is higher than that of any other object (except Q2000–330, which is at a higher redshift still). With such a high line density, the fraction of the wavelength coverage blanketed by strong lines will be higher than in lower redshift spectra and the blanketing correction will be greater. It is likely that such a correction would significantly increase the best estimates of  $\beta$ , making the values of Cristiani *et al.* closer to or consistent with  $\beta \sim 1.5$  for  $\log N \lesssim 15$ . The value of  $\beta = 1.46$  reported by Songaila *et al.* (1995) had no uncertainty quoted, and the method used to calculate this value is not described in their paper.

### Implications for Other Work

The conclusion of this work on the Lyman  $\alpha$  forest column density distribution is that the lines within the range  $13.0 \lesssim \log N \lesssim 15.0$  follow a power law distribution with index  $\beta = 1.55 \pm 0.05$  for  $1.5 < z_{\text{abs}} < 3.5$ . This is inconsistent with earlier research which gave  $\beta \sim 1.7$ , but consistent with more recent work in which the validity of including lines with  $\log N \gtrsim 15$  has been questioned.

This result may explain the discrepancies found by Barcons and Webb (1991, discussed in Section 6.2) *without* appealing to clustering of Lyman  $\alpha$  clouds. It is more likely, though, that the finding of Barcons and Webb is a symptom of both the lower intrinsic  $\beta$  value for low column density clouds *and* some level of small-scale clustering of the Lyman  $\alpha$  clouds.

A value of  $\beta \sim 1.55$  also throws some doubt on the claim of Webb *et al.* (1992) that significant Gunn-Peterson HI absorption may be present at  $z_{\text{abs}} \sim 4$ . Webb *et al.* found a best fit to their data with  $\beta \sim 1.3$  for  $\log N < 13.75$  when no Gunn-Peterson absorption was assumed. At  $z_{\text{abs}} \sim 4$  there are certainly numerous Lyman  $\alpha$  clouds, so line blanketing will be severe, though it is not clear how badly this will affect determinations of  $\beta$ . If it does make a significant difference then the required value of  $\beta \sim 1.3$  will be underestimated and the measurement of  $\beta \sim 1.55$  may be low enough to explain their results without requiring any Gunn-Peterson absorption.

## 6.3 Redshift Evolution

The number density of Lyman  $\alpha$  clouds evolves strongly with redshift, with the clouds becoming less numerous at lower redshifts. This was first established quantitatively by Murdoch *et al.* (1986) as discussed in Section 1.5.3. The most important parameter used to describe the cloud number evolution is  $\gamma$ , defined in Equation 1.14, and reproduced here:

$$\frac{dN}{dz} \propto (1+z)^\gamma. \quad (6.3)$$

The best estimate of Murdoch *et al.* for the power law index was  $\gamma = 2.17 \pm 0.36$  for  $1.50 < z_{\text{abs}} < 3.78$ . Murdoch *et al.* also demonstrated the existence of an “inverse effect” (discussed in Section 1.5.4), in which a significant trend for Lyman  $\alpha$  lines

to become *less* numerous at higher redshifts was seen in the spectra of *individual* QSOs. They showed this effect was confined to regions of space physically near the QSOs and, by removing absorption lines within the Lyman  $\alpha$  emission lines from the sample, they calculated a corrected value of  $\gamma = 2.31 \pm 0.40$ . This was further refined to  $\gamma = 2.36 \pm 0.40$  by Bajtlik *et al.* (1988) after more detailed corrections.

Parnell and Carswell (1988) studied the effects on  $\gamma$  of line blending in intermediate-resolution spectra. They produced realistic simulations of absorption spectra with S/N ratio 15 for a variety of input  $\gamma$  values. Their results showed that the measured value of  $\gamma$  was systematically lower than the input value by an amount approximately equal to the  $1\sigma$  measurement uncertainties, but they concluded that the line blending did *not* greatly affect the observed value of  $\gamma$  and that intermediate resolution spectra were adequate to determine the redshift evolution index. In a similar study, Liu and Jones (1988) claimed that line blending in intermediate-resolution spectra caused systematic underestimates of  $\gamma$  and that  $\gamma$  would be underestimated by a greater amount in samples with lower  $W_0$  cut-offs. Trèvese *et al.* (1992) reached a similar conclusion, except they found that  $\gamma$  was *overestimated* at high  $W_0$  cut-offs and underestimated at low ones. They pointed out that this effect could cause a spurious trend of increasing  $\gamma$  with increasing line-strength.

Lu *et al.* (1991) compiled a sample of 950 Lyman  $\alpha$  lines with  $1.7 < z_{\text{abs}} < 3.8$  and  $W_0 > 0.36 \text{ \AA}$  from the spectra of 38 QSOs and performed several statistical tests on it. Without correcting for the proximity effect, they found a power law with  $\gamma = 2.37 \pm 0.26$  was a good fit to the data. However, they also found strong evidence for the reality of the proximity effect and, after correcting for it by removing lines within  $8h^{-1} \text{ Mpc}$  of each QSO's emission redshift, concluded the best value of  $\gamma$  for the redshift range covered was  $2.75 \pm 0.29$ . Lu *et al.* also explored the possibility that the redshift evolution followed a broken power law, with the slope steepening below  $z_{\text{abs}} \sim 2.3$ . Although such a description gave a better fit to the data, there was no evidence to suggest the single power law form was inadequate.

Giallongo (1991) presented evidence for a differential redshift evolution in the number density of Lyman  $\alpha$  clouds, in the sense that higher column density clouds (producing lines of higher  $W_0$ ) evolved more slowly. Using data from four QSOs, Giallongo determined  $\gamma = 2.91 \pm 0.99$  for lines with  $0.14 < W_0 < 0.2 \text{ \AA}$ ,  $\gamma = 1.05 \pm 0.85$  for  $0.3 < W_0 < 0.5 \text{ \AA}$ , and an intermediate value of  $\gamma$  for the intermediate subsample. This was claimed as evidence of a continuous trend which might extend to metal line clouds, which have very high Lyman  $\alpha$  equivalent widths and do not appear to evolve with redshift at all. This issue is discussed in detail in Section 6.5, but it should be noted that Giallongo's finding is not well supported by further research, with the main objection being that the data sample was small and inhomogeneous.

Bechtold (1994) presented intermediate-resolution ( $65\text{--}100 \text{ km s}^{-1}$ ) data for 34 QSOs with  $2.739 < z_{\text{em}} < 4.111$  and compiled a sample of 2792 Lyman  $\alpha$  lines from these data and 44 other QSO spectra published in the literature. After removing regions within  $8h^{-1} \text{ Mpc}$  of  $z_{\text{em}}$  for each object, the value of  $\gamma$  for lines with  $W_0 \geq 0.32 \text{ \AA}$  was found to be  $1.80 \pm 0.25$ . This was significantly lower than the best estimate of Lu *et al.*, and probably more reliable because of the more homogeneous

and much larger line sample. Bechtold noted, however, that  $\gamma$  is likely to be a function of redshift and the differences may have been caused by differences in the redshift coverage of the samples. In particular, there was tentative evidence for a steepening of the evolutionary index at  $z_{\text{abs}} \lesssim 2.5$ , in agreement with the break in the power law proposed by Lu *et al.* Since Bechtold's data were weighted towards high- $z$  QSOs, such a change in the evolutionary index with  $z_{\text{abs}}$  would have produced a lower estimate of  $\gamma$  than the sample of Lu *et al.*

Bechtold also noted that the estimates of  $\gamma$  from her sample showed a monotonic trend to smaller values when the  $W_0$  cut-off was lowered. This could imply that weaker lines evolve more slowly than stronger ones or, as pointed out by Bechtold, may be an artefact produced by line blending or variable S/N effects.

### High Resolution Studies

The earliest studies of QSO absorption lines at high resolution ( $\sim 10 \text{ km s}^{-1}$ , CLPW, PHSM) did not contain enough lines to perform an informative analysis of the redshift distribution of weak lines.

Giallongo *et al.* (1993) examined the evolution of line density in high-resolution spectra of the three objects PKS 2126–158, Q0014+813 (Rauch *et al.*, 1992), and Q1101–264 (CLPW). Selecting lines with column densities above the completeness limit and below a level where saturation makes deconvolving blends difficult, they calculated  $\gamma = 2.21 \pm 0.05$  for  $13.3 \leq \log N \leq 14.8$ . This was not considered inconsistent with the value of  $\gamma = 2.75 \pm 0.29$  determined by Lu *et al.* (1991) at lower resolution, because of the tendency to overestimate  $\gamma$  using such data (Trèvese *et al.*, 1992).

Giallongo *et al.* (1993) also attempted to determine if there was differential evolution as a function of column density. They found  $\gamma = 2.53 \pm 0.52$  for lines with  $13.3 \leq \log N \leq 13.78$  and  $\gamma = 1.83 \pm 0.17$  for lines with  $13.78 < \log N \leq 16.0$ . This was taken as evidence for differential evolution in the same sense as claimed by Giallongo (1991), with weaker lines evolving more rapidly. Just as in the older study, however, the sample of Giallongo *et al.* was small and inhomogeneous in resolution.

Cristiani *et al.* (1995) added their high-resolution ( $14 \text{ km s}^{-1}$ ) data for Q0055–269 and also data for Q2206–199N (Rauch *et al.*, 1993) to the sample of Giallongo *et al.* (1993). They found  $\gamma = 2.47 \pm 0.44^7$  for lines with  $13.3 \leq \log N \leq 14.5$ . Dividing their sample in a manner similar to that of Giallongo *et al.*, they found  $\gamma = 2.51 \pm 0.12$  for lines with  $13.3 \leq \log N \leq 13.8$  and  $\gamma = 1.86 \pm 0.21$  for  $13.8 < \log N \leq 17.0$ . These are close to the values of Giallongo *et al.*, but the uncertainty estimates appear inconsistent, given that Cristiani *et al.* used a superset of Giallongo *et al.*'s data.

---

<sup>7</sup>The uncertainty in this value of  $\gamma$  is  $\sim 9$  times larger than that quoted by Giallongo *et al.* (1993) for their value, which was based on a subset of Cristiani *et al.*'s data. Given the number of lines in each analysis, it seems likely that the uncertainty in Giallongo *et al.*'s value of  $\gamma = 2.21 \pm 0.05$  has been severely underestimated.

If the high-resolution results of Giallongo *et al.* and Cristiani *et al.* reveal a real tendency for weaker Lyman  $\alpha$  lines to evolve more rapidly than stronger ones, it would be consistent with the unification models of Tytler (1987a) and Giallongo (1991), which are discussed in detail in Section 6.5. As mentioned already, though, the number of QSOs observed at high resolution is small and the data are far from uniform in completeness and sampling of redshift space.

### Lyman $\alpha$ Clouds at Low Redshift

With the launch of the *Hubble Space Telescope* (HST), spectroscopy of the Lyman  $\alpha$  forest could be extended far enough into the ultraviolet to study Lyman  $\alpha$  clouds at redshifts  $z_{\text{abs}} \sim 0$ . The first results from the Goddard High-Resolution Spectrograph (GHRS), on the  $z_{\text{em}} = 0.158$  QSO 3C 273, were presented by Morris *et al.* (1991). These are the only high-resolution data to date on the Lyman  $\alpha$  forest at low redshift.

The GHRS provides spectral resolutions down to  $\sim 0.08 \text{ \AA}$  ( $20 \text{ km s}^{-1}$  at low redshift) and the Lyman  $\alpha$  forest is relatively sparse in the spectrum of 3C 273, making line deconvolution straightforward because there is no appreciable line blending. The rest equivalent width completeness limit for Lyman  $\alpha$  lines is therefore comparable to that for AAT UCLES data. Morris *et al.* found 14 probable Lyman  $\alpha$  lines in their highest-resolution data. They noted that an extrapolation from the value of  $\gamma$  for high-redshift data (Murdoch *et al.*, 1986; Bajtlik *et al.*, 1988) significantly underestimated the number of clouds observed. As they noted, however, the high-redshift data referred to lines with much greater equivalent widths.

Morris *et al.* also combined their data with CLPW's high-resolution data for Q1101–264 to determine a value of  $\gamma = 0.79 \pm 0.37$  for clouds with  $W_0 \geq 50 \text{ m\AA}$  over the redshift range  $0.02 < z_{\text{abs}} < 2.14$ <sup>8</sup>. Citing the contrast with the value of  $\gamma = 2.36 \pm 0.40$  obtained by Bajtlik *et al.* at high redshift, Morris *et al.* concluded that “there is a significant decrease in the rate at which the Lyman  $\alpha$  forest thins out, occurring at some redshift less than  $\sim 2$ ”.

An alternative explanation, not mentioned by Morris *et al.*, is that the rate of number density evolution may vary with line equivalent width (or cloud column density). This is a possible explanation because their results were based on lines mostly with  $W_0 < 400 \text{ m\AA}$ , while the lines used by Bajtlik *et al.* were exclusively with  $W_0 > 360 \text{ m\AA}$ . Morris *et al.* found *no* Lyman  $\alpha$  lines with  $W_0 > 360 \text{ m\AA}$  in their 3C 273 spectrum, which is consistent with the prediction extrapolated from the result of Bajtlik *et al.*. The data did not favour either this explanation or the one proposed by Morris *et al.*. One also needs to be careful of drawing too strong a conclusion from a data set containing only a single low-redshift and a single high-redshift sightline. If either sightline is not representative of the distribution of Lyman  $\alpha$  clouds at its redshift, it will bias the estimate of  $\gamma$ . Many sightlines at each redshift are needed to reduce this effect.

<sup>8</sup>Much of this  $z_{\text{abs}}$  range was not actually covered by the data. 3C 273 provided data with  $0.02 < z_{\text{abs}} < 0.16$  and Q1101–264 provided data with  $1.82 < z_{\text{abs}} < 2.14$ .

Bahcall *et al.* (1993) presented first results from the HST Quasar Absorption Line Key Project, including data from 37 QSOs with  $0.158 < z_{\text{em}} < 1.270$ . Thirteen of these objects were observed at spectral resolutions of  $1.1\text{--}2.0 \text{ \AA}$  ( $180\text{--}330 \text{ km s}^{-1}$  at  $z_{\text{abs}} \sim 0.5$ )<sup>9</sup> and used to compile a sample of 104 Lyman  $\alpha$  lines with  $0.003 < z_{\text{abs}} < 0.977$ . Excluding lines within  $3000 \text{ km s}^{-1}$  of the respective QSO emission redshifts (corresponding to a generous  $30\text{--}11h^{-1} \text{ Mpc}$  for  $z = 0.0\text{--}1.0$  respectively) to eliminate the proximity effect, Bahcall *et al.* calculated a best fit  $\gamma = 0.30 \pm 0.61$  from their data. Restricting the sample to lines above the completeness limit of  $W_0 = 0.32 \text{ \AA}$  gave a value of  $\gamma = 0.50 \pm 0.77$ , consistent with no evolution of the Lyman  $\alpha$  cloud number density between redshifts of 1 and 0. Kolmogorov goodness-of-fit tests showed that both these samples were compatible with the simple power law fits.

Bahcall *et al.* combined their data with the sample of high-redshift lines assembled by Lu *et al.* (1991) to investigate the behaviour of  $\gamma$  over a large redshift baseline. Using a uniform completeness limit of  $W_0 \geq 0.36 \text{ \AA}$ , they found  $\gamma = 1.72 \pm 0.15$ , but with a Kolmogorov goodness-of-fit probability of only 0.07. They took this as marginal evidence for a break in the evolutionary index, in the same sense as proposed by Morris *et al.* (1991). Using the subset of Lu *et al.*'s sample with  $z_{\text{abs}} < 2.16$ , the best fit index was  $\gamma = 0.96 \pm 0.23$ . Bahcall *et al.* noted that this was consistent with the suggested steepening in the distribution at  $z_{\text{abs}} \sim 2.3$  proposed by Lu *et al.* (because the number of clouds with  $z_{\text{abs}} < 2.16$  would then be less than expected from the higher redshift power law, so a fit using these data and the HST data should produce a smaller value of  $\gamma$  than one using all the high- $z$  data).

Bechtold (1994) used a much larger sample of high- $z$  lines, combined with the HST data of Bahcall *et al.*, to determine that a power law with best fit  $\gamma = 1.29 \pm 0.14$  was an acceptable fit to all the data with  $W_0 \geq 0.32 \text{ \AA}$  in the range  $0.003 < z_{\text{abs}} < 4.111$ .

### 6.3.1 Calculations of $\gamma$

The AAT UCLES data for the objects Q1101–264 and Q2348–147 presented here, together with those of Q2206–199N (PHSM) and *Hubble Space Telescope* (HST) Goddard High-Resolution Spectrograph (GHRS) data of 3C 273 (Morris *et al.*, 1991), were used to examine the value of  $\gamma$  and its behaviour in various samples of Lyman  $\alpha$  lines. All these data have spectral resolutions of  $\sim 0.08 \text{ \AA}$ , which allows the detection of absorption lines with rest equivalent widths an order of magnitude or more below the completeness limits of intermediate-resolution studies<sup>10</sup>. The aim

<sup>9</sup>Only preliminary, lower resolution observations of the remaining 24 objects had been made at the time.

<sup>10</sup>For 3C 273 this spectral resolution corresponds to a velocity resolution of  $20 \text{ km s}^{-1}$ , whereas for the higher redshift objects it corresponds to  $\sim 7 \text{ km s}^{-1}$ . As mentioned in Section 6.3, the sparseness of the Lyman  $\alpha$  forest at low redshift means very few lines are blended, so profile fitting is easier and the detection limit is lower than for a spectrum of similar velocity resolution at high redshift.

**Table 6.3** Absorption redshift ranges in each of the objects used to calculate  $\gamma$ . The number of Lyman  $\alpha$  lines in the given  $z_{\text{abs}}$  and  $W_0$  ranges for each object are also listed.

Object	$z_{\text{abs}}$ range	Number of lines		Reference
		$25 \leq W_0 < 100 \text{ m}\text{\AA}$	$100 \leq W_0 < 400 \text{ m}\text{\AA}$	
3C 273	0.008–0.155	8	5	Morris <i>et al.</i> (1991)
Q1101–264	1.789–2.132	28	21	This work
Q2206–199N	2.072–2.541	21	34	(PHSM)
Q2348–147	2.067–2.919	140	130	This work

of this study was to examine more closely the redshift evolution of Lyman  $\alpha$  lines with  $W_0 \lesssim 400 \text{ m}\text{\AA}$ , first looked at by Morris *et al.*.

With intermediate-resolution data, a large QSO sample is needed to obtain reasonably certain values of  $\gamma$ , because the number of strong ( $W_0 \gtrsim 400 \text{ m}\text{\AA}$ ) Lyman  $\alpha$  lines per spectrum is small (Bechtold, 1994, for example). However, the power-law column density distribution of Lyman  $\alpha$  clouds ensures that many more weaker Lyman  $\alpha$  lines are detectable in high-resolution spectra than strong lines. Therefore relatively few QSO spectra are needed for a similar study of the evolution of the weak lines. This is fortunate, since high-resolution data exist only for a handful of objects so far.

The GHRS spectrum of 3C 273 was included in the sample to provide a long redshift baseline for the calculation of  $\gamma$ . The high-redshift objects span only  $1.789 < z_{\text{abs}} < 2.919$ , while the addition of 3C 273 extends the range of  $z_{\text{abs}}$  to 0.008 (although without continuous redshift coverage). Unfortunately, there are relatively few lines detected in the 3C 273 spectrum (13 in the samples defined below), so the uncertainty added by Poissonian noise in the line density at low redshift is considerable. Since the 3C 273 GHRS spectrum is the *only* high-resolution low-redshift spectrum available, however, there is no choice but to proceed by assuming its sightline is typical of those at such redshifts and applying appropriate caution in interpreting the results.

The redshift ranges covered by the spectra and the numbers of Lyman  $\alpha$  lines in each spectrum are given in Table 6.3. The upper ends of the redshift ranges have been calculated to be the  $z_{\text{abs}}$  at which an object on the line of sight is  $8h^{-1}$  Mpc from the respective QSO. This is to avoid any possible biasing of the  $\gamma$  calculations by the proximity effect (see Section 1.5.4). The lower end of the 3C 273 range is dictated by the difficulty in measuring HI equivalent widths within the damping wings of Galactic Lyman  $\alpha$  absorption. The two lines detected by Morris *et al.* within the damping wing are not included in this analysis. The lower ends of the ranges for the other objects correspond simply to the blue limits of the wavelength coverage. The echelle spectra of Q1101–264, Q2206–199N, and Q2348–147 have some small gaps in the redshift ranges covered.

The value of  $\gamma$  was calculated for various combinations of QSOs, and different rest equivalent width ranges. The largest equivalent width range chosen was  $25 \leq W_0 < 400 \text{ m}\text{\AA}$ . The samples are reasonably complete above the lower cut-off of  $25 \text{ m}\text{\AA}$ <sup>11</sup>.

<sup>11</sup>The true completeness limit is  $W_0 \sim 50 \text{ m}\text{\AA}$ . A slightly lower value was chosen here to take

**Table 6.4** Calculated ML values of  $\gamma$  for various samples of Lyman  $\alpha$  lines. The Kolmogorov-Smirnov goodness-of-fit probabilities for the fitted power law are shown in parentheses for the high-redshift objects.

Objects	Sample equivalent width limits		
	$25 \leq W_0 < 400 \text{ m}\text{\AA}$	$25 \leq W_0 < 100 \text{ m}\text{\AA}$	$100 \leq W_0 < 400 \text{ m}\text{\AA}$
1101/2206	$1.5 \pm 1.6$ (0.14)	$0.4 \pm 2.9$ (0.24)	$3.2 \pm 2.1$ (0.33)
1101/2348	$1.95 \pm 0.61$ (0.00)	$2.10 \pm 0.84$ (0.04)	$2.11 \pm 0.91$ (0.12)
2206/2348	$1.30 \pm 0.80$ (0.00)	$2.2 \pm 1.2$ (0.00)	$0.2 \pm 2.0$ (0.00)
1101/2206/2348	$2.39 \pm 0.61$ (0.00)	$2.73 \pm 0.89$ (0.00)	$2.34 \pm 0.87$ (0.00)
3C 273/1101	$0.78 \pm 0.31$	$0.61 \pm 0.40$	$0.81 \pm 0.49$
3C 273/2206	$0.62 \pm 0.28$	$0.19 \pm 0.37$	$1.04 \pm 0.43$
3C 273/2348	$1.10 \pm 0.22$	$1.00 \pm 0.28$	$1.24 \pm 0.33$
3C 273/1101/ 2206/2348	$1.25 \pm 0.25$	$1.09 \pm 0.33$	$1.47 \pm 0.39$

Notes:

“1101” refers to Q1101–264.

“2206” refers to Q2206–199N.

“2348” refers to Q2348–147.

The  $400 \text{ m}\text{\AA}$  upper limit is a somewhat arbitrary choice, but was chosen to be close to the lower limits typically used in studies of redshift evolution using intermediate resolution data (Sargent *et al.*, 1980; Murdoch *et al.*, 1986; Tytler, 1987b; Lu *et al.*, 1991; Giallongo, 1991; Bahcall *et al.*, 1993; Bechtold, 1994). In a sample of just four QSOs there are only a few Lyman  $\alpha$  lines above this limit. Values of  $\gamma$  were also calculated for subsamples divided by equivalent width. The value of  $100 \text{ m}\text{\AA}$  was chosen as the division between the subsamples because it is close to the median  $W_0$  for each of the objects, resulting in samples of roughly equal size.

The maximum likelihood method of Murdoch *et al.* (1986) was used to calculate the values and uncertainties of  $\gamma$  for the various samples. The results are shown in Table 6.4.

In each case, the redshift range over which the calculation was performed was discontinuous because of the large redshift gap between 3C 273 and the other objects, and the inter-order gaps in the echelle spectra. The calculation of  $\gamma$  by the ML method correctly accounts for this fact. Also, Kolmogorov-Smirnov tests were performed on the groupings of high-redshift QSOs to determine the goodness-of-fit of the observed line distributions to a power law.

Additionally, there is a line blanketing effect (discussed in Section 2.3.2) in which

advantage of the large number of extra lines which are still detected just below the completeness limit. All the extra lines used because of this lower limit are still detected with  $W_0 \geq 6\sigma_{W_0}$ . The rest equivalent width completeness limits are similar for each object, and it is known that there is no strong dependence of  $\gamma$  with line strength, so any inaccuracies in the calculations of  $\gamma$  caused by this approach will be minimal. The larger line sample allows improved accuracy in the  $\gamma$  calculations. There are about twice as many lines with  $25 \leq W_0 < 100 \text{ m}\text{\AA}$  than with  $50 \leq W_0 < 100 \text{ m}\text{\AA}$ , so the uncertainty on  $\gamma$  with the larger sample is  $\sim \sqrt{2}$  times smaller than for the smaller sample.

strong lines *not* included in any given sample may obscure weaker lines which would otherwise have been included in the sample. This effect would be expected to change the observed numbers of weak lines most when the line density is high, *i.e.* at high redshifts. Therefore a systematic error might be expected in which weak lines appear less numerous at higher redshifts, resulting in an artificially low apparent value of  $\gamma$ . To compensate for this effect, zones around each such strong line where weaker lines might be present but undetectable were determined visually and excluded from the ML analysis. Tests showed that ignoring this correction generally changed the calculated values of  $\gamma$  by  $< 0.01$ , so some inaccuracies in judging the excluded zones (or even if this correction is ignored altogether) make no significant difference to the values shown in Table 6.4.

### 6.3.2 Discussion of $\gamma$ Results

From the results quoted in Table 6.4, it is clear that a larger sample of high-resolution spectra is needed before values of  $\gamma$  can be determined accurately for samples of Lyman  $\alpha$  lines with  $W_0 < 400$  mÅ. The  $1\sigma$  uncertainties are large and the value of  $\gamma$  is not consistent between samples derived from the spectra of different objects. Additionally, many of the Kolmogorov probabilities are too low ( $< 0.05$ ) for the fitted power law to be acceptable as a good fit to the form of the line distribution.

In particular, the Kolmogorov probabilities for the Q1101–264/Q2206–199N pairing are high enough to accept the power law fit, while for all the other pairings, and the triplet of all high-redshift QSOs, the only other acceptably high probability was for the  $100 \leq W_0 < 400$  mÅ sample for the Q1101–264/Q2348–147 pairing. This could be taken as evidence that one or more of the three sightlines is atypical in the number of Lyman  $\alpha$  lines detected—a possibility discussed further under the heading *High-Redshift Pairings* in this Section.

There are a few trends which can be seen, however. The inclusion of the 3C 273 data generally gives lower values of  $\gamma$  than the calculations without them. This trend was first noticed by Morris *et al.* (1991), as discussed in Section 6.3. Morris *et al.* interpreted this result as evidence that the sharp decrease in Lyman  $\alpha$  cloud number density with lower redshift slowed down considerably at low redshifts. However, in coming to this conclusion they were forced to compare  $\gamma$  results from a strong line ( $W_0 > 360$  mÅ) sample at high-redshift (Bajtlik *et al.*, 1988) with their result on weak lines.

The results quoted here use high-resolution data exclusively, so the samples are homogeneous in rest equivalent width, and the trend of a lower  $\gamma$  when the 3C 273 data are included is still present. In particular, the result for all three high-redshift QSOs in the full  $W_0$  range is  $\gamma = 2.39 \pm 0.61$  ( $1.79 < z_{\text{abs}} < 2.92$ ), which is significantly different from the result including 3C 273 of  $\gamma = 1.25 \pm 0.25$  ( $0.01 < z_{\text{abs}} < 2.92$ ). If we accept that the sightlines being studied are typical of those at the appropriate redshifts<sup>12</sup>, this does imply a significant decrease in the

<sup>12</sup>See Section 8.2 for a detailed discussion of this assumption and its validity.

rate of number density evolution of low  $W_0$  Lyman  $\alpha$  clouds at some redshift less than 2. This result does not, however, say anything about the rate of evolution of clouds with  $W_0 > 400 \text{ m}\text{\AA}$ . As discussed in Section 6.3, the absence of strong lines in the 3C 273 spectrum is consistent with a single power law of  $\gamma \sim 2.3$  for such lines in the range  $0.0 < z_{\text{abs}} < 2.1$ .

### Differential Evolution

The slowing of the cloud number evolution may be greater for the weaker clouds. The  $25 \leq W_0 < 100 \text{ m}\text{\AA}$  subsamples show a greater difference between the values of  $\gamma$  for the high-redshift QSO data and those of the full set of objects than the  $100 \leq W_0 < 400 \text{ m}\text{\AA}$  subsamples. The uncertainties are large enough that the  $\gamma$  values could be equal in both  $W_0$  subsamples, but the differences in the best estimates are suggestive of a differential rate of number density evolution, in the sense that weaker clouds thin out more slowly than stronger clouds at  $z_{\text{abs}} \lesssim 2$ .

The best estimates of  $\gamma$  for the pairings of the data of each high-redshift QSO with the 3C 273 data also show slower evolution for the weak subsamples compared to the strong subsamples. That this trend exists in each pairing of the 3C 273 data with those of a high-redshift QSO is evidence in favour of its reality. A trend of slower evolution for weaker lines is contrary to the findings of Giallongo (1991), Giallongo *et al.* (1993), and Cristiani *et al.* (1995) (described briefly in Section 6.3 and discussed in greater detail in Section 6.5). The present sample of lines is smaller than the ones used in these previous studies, but is much more homogeneous, comprising data from four QSOs with similar resolutions and completeness limits. Also, the earlier studies retained saturated lines, which are difficult to deblend and therefore to count accurately, when measuring  $\gamma$  for their high  $W_0$  subsamples<sup>13</sup>. I have defined subsamples to avoid saturated lines, thereby minimising this problem.

There is, of course, always a possibility that the result of the present study has been caused by a line-blending or S/N-related effect. Liu and Jones (1988) and Trèvese *et al.* (1992) pointed out that line blending can impose an artificial trend of stronger evolution for stronger lines. However, their results were based on intermediate-resolution spectra and say nothing about any possible effects on high-resolution spectra, where blends can more readily be deconvolved, as noted by Giallongo (1991). The effect of line-blending should be minimal when examining only high-resolution data, at least at redshifts  $z \lesssim 3$ .

If the lowest  $W_0$  Lyman  $\alpha$  clouds detected in these spectra do indeed thin out more slowly than higher  $W_0$  clouds, this presents an intriguing puzzle. A first impression would be that more massive clouds are likely to have longer lifetimes than less massive ones (since they would take longer to ionise or disperse), so their numbers should decrease more slowly than those of the less massive clouds. However, the column density of a given cloud will also change with time. Clouds with high  $N(\text{H I})$  (and hence  $W_0$ ) at high redshift will contain less neutral hydrogen over time,

<sup>13</sup>They actually used a column density cut-off to define their subsamples, but the qualitative result is the same.

so the low  $N(\text{HI})$  clouds seen at low redshifts will not correspond to clouds of similar column density at high redshift. The high- $z$ , low- $N(\text{HI})$  clouds will “fade away”, to be replaced by similarly fading, higher  $N(\text{HI})$  clouds. This scenario leaves clouds with low  $W_0$  at low- $z$ , but very few with high  $W_0$ .

The column density evolution of individual clouds has been discussed by Murdoch *et al.* (1986). Firstly, it is important to note that the high  $W_0$  clouds being considered fall on the saturated part of the curve-of-growth. In terms of rest equivalent width, saturation depends strongly on the  $b$  value of the cloud—an approximate relation for typical velocity dispersions ( $b \sim 10\text{--}50 \text{ km s}^{-1}$ ) is that clouds with

$$W_0 \gtrsim 0.01 \left( \frac{b}{\text{km s}^{-1}} \right) \text{ \AA} \quad (6.4)$$

will be saturated. Saturated line profiles change very little in  $W_0$  with quite large changes in cloud column density. For example, a cloud with  $b = 30 \text{ km s}^{-1}$  evolving from  $\log N = 16$  to  $\log N = 15$  will change only from  $W_0 = 0.60 \text{ \AA}$  to  $W_0 = 0.47 \text{ \AA}$ . This means that saturated clouds which change in  $W_0$  by a substantial amount over time must have their neutral hydrogen column densities changing by large factors. If it is true that clouds evolve from  $W_0 \sim 0.4 \text{ \AA}$  to  $W_0 \sim 0.1 \text{ \AA}$ , then their  $N(\text{HI})$  must be depleted by two or more orders of magnitude. Murdoch *et al.* showed that their intermediate-resolution data implied a strong power law evolution in the column density of individual clouds:

$$N(\text{HI}) \propto (1 + z)^\eta, \quad (6.5)$$

with  $\eta \sim 6$ , consistent with theoretical models of Ikeuchi and Ostriker (1986). If such rapid column density evolution continues into the linear part of the curve-of-growth, then clouds with  $W_0 \lesssim 0.1 \text{ \AA}$  will have very short lifetimes as detectable absorbers.

There is now good evidence to suggest that the rate of Lyman  $\alpha$  cloud evolution changes with redshift, with  $\gamma \sim 0.3$  at  $z_{\text{abs}} \sim 0$  (Bahcall *et al.*, 1993) but  $\gamma \sim 2$  at  $z_{\text{abs}} > 2$  (Bechtold, 1994). Additionally, there is a possible break at  $z_{\text{abs}} \sim 2.3$ , with  $\gamma$  being smaller above this redshift. Some progressive estimates of  $\gamma$  from the literature and this work are illustrated in Figure 6.4. It seems likely that the Lyman  $\alpha$  clouds evolve at a moderate rate from  $z_{\text{abs}} = 4.1$  to  $\sim 2.3$ , then evolve more rapidly for some time until, at  $z_{\text{abs}} \sim 1\text{--}2$ , the rate of evolution slows considerably. It is not clear whether  $\gamma$  is also a function of column density, and if so in what sense. There is no intrinsic reason for  $\gamma$  to be constant across several orders of magnitude of column density—indeed it would not be surprising if the evolution rate varied—but any differential evolution has not yet been firmly established.

It may be possible that low column density absorbers are partially replenished over time, resulting in an apparent slowing of their evolution. Morris and van den Bergh (1994) demonstrated that low- $N$  absorbers could be produced in tidal debris built up in small clusters of galaxies. They went on to show that such tidal debris could be a major source of Lyman  $\alpha$  absorbers at low redshifts. If the majority of low- $z$  absorbers have been produced by such methods only recently, then the

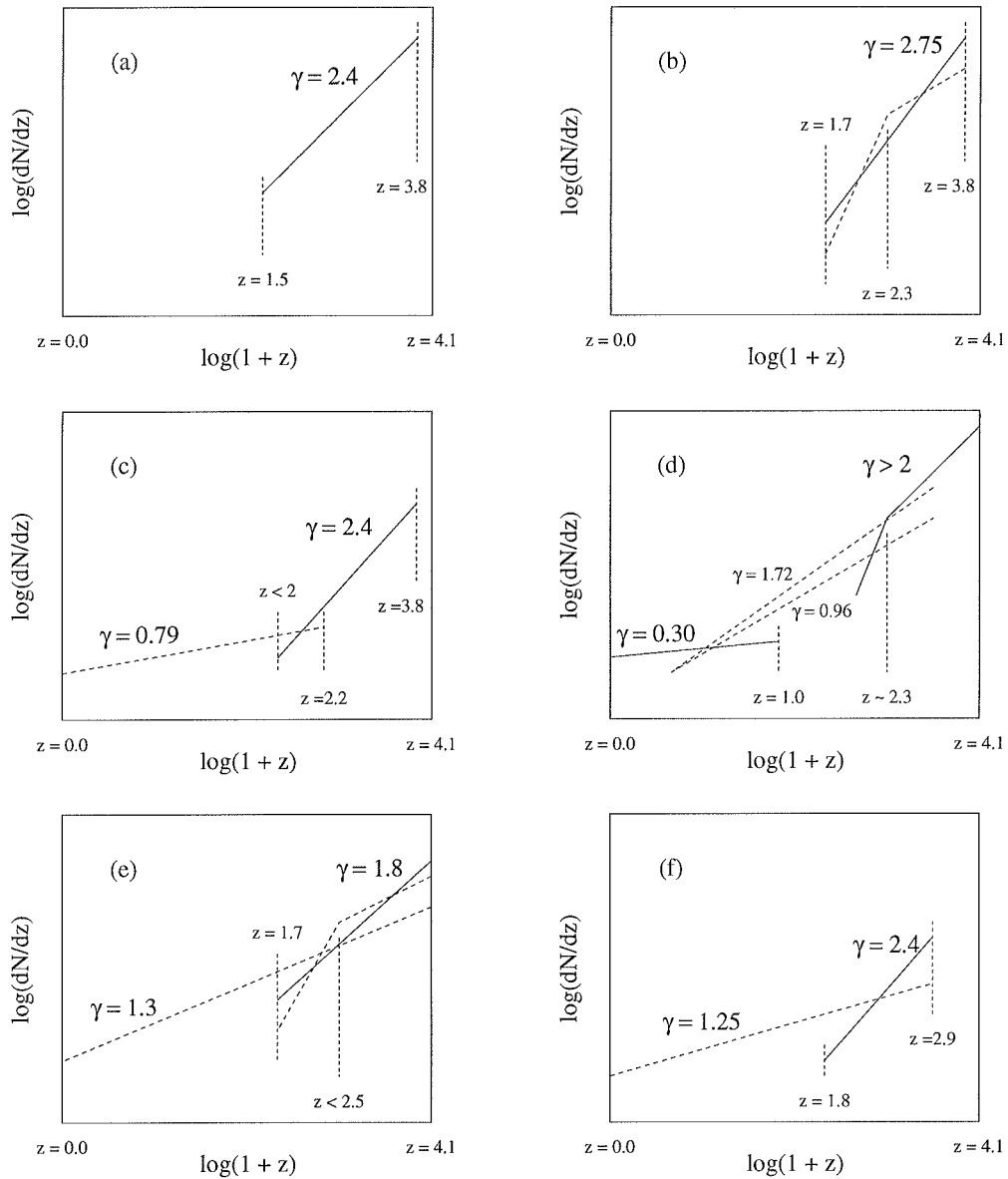


**Figure 6.4** “Cartoon” illustrations of progressive  $\gamma$  estimates. Each panel shows estimates of  $\gamma$  by a certain author, plotted as straight lines on logarithmic axes. Solid lines show  $\gamma$  estimates based on data covering the entire redshift range labelled; dashed lines show either tentatively detected breaks in the power law (panels b and e) or  $\gamma$  estimates for long redshift baselines using data at each end (panels c, e, f). Panels: (a) Murdoch *et al.* (1986), as corrected for the proximity effect by Bajtlik *et al.* (1988). (b) Lu *et al.* (1991). (c) Morris *et al.* (1991), (d) Bahcall *et al.* (1993). (e) Bechtold (1994). (f) This work.

evolution rate of high- $z$  absorbers may not slow down as much as the data seem to indicate.

### High-Redshift Pairings

An interesting point to note from the results given in Table 6.4 is that the  $\gamma$  values for the data from pairs of the high-redshift QSOs span a large range. The values for the full  $25 \leq W_0 < 400 \text{ m\AA}$  samples are reasonably consistent, but the best estimates for the two  $W_0$  subsamples in each pairing show no consistent pattern at all.

For the Q1101–264/Q2348–147 pairing, the  $W_0$  subsamples give almost identical values of  $\gamma$ . In contrast, the Q1101–264/Q2206–199N pairing gives  $\gamma = 0.4, 3.2$  for the weak and strong subsamples respectively, while the Q2206–199N/Q2348–147 pairing gives  $\gamma = 2.2, 0.2$ . The uncertainties are large, so no real inferences can be drawn, but the values show clearly the differences in the characters of the three spectra.

Relative to the other two spectra, that of Q2206–199N contains an overabundance of strong Lyman  $\alpha$  lines and a paucity of weak ones. Since Q2206–199N is intermediate in redshift between Q1101–264 and Q2348–147, the trends seen between Q1101–264 and Q2206–199N are seen in the opposite sense between Q2206–199N and Q2348–147. The weak lines, for example, appear to evolve strongly between Q2348–147 and Q2206–199N, but not at all between Q2206–199N and Q1101–264, whereas the strong lines show the opposite behaviour. This also explains the poor Kolmogorov-Smirnov goodness-of-fit probabilities for the power laws fitted to most of the sets of combined data.

This behaviour does not serve to reveal the true nature of the Lyman  $\alpha$  cloud evolution in the range  $2 < z_{\text{abs}} < 3$ , but rather shows the difficulties of inferring evolutionary properties from such a small sample of objects. The results in Table 6.4 could imply that the sightline to Q2206–199N is somehow atypical of sightlines covering the same redshift interval. It is also possible that any combination of the three sightlines studied probes atypical volumes of high-redshift space. A much larger number of sightlines is needed to obtain a representative sampling of the cloud properties. The problem of significant differences between individual sightlines is discussed further in Section 8.2.

## 6.4 The Velocity Dispersion Distribution

The distribution of velocity dispersions among Lyman  $\alpha$  clouds is potentially a very useful tool for determining physical properties of the absorbers. Equation 1.8 relates the measured  $b$  value to the temperature of the absorbing gas and the degree of bulk motion (turbulence, rotation, etc.) present. Since any bulk motion adds in quadrature to the thermal velocity dispersion, the measured  $b$  value of a line provides an upper limit on the temperature of the absorber.

The temperature of the Lyman  $\alpha$  clouds is a parameter which can also be investigated theoretically. The first physical model for Lyman  $\alpha$  clouds was proposed by Sargent *et al.* (1980, SYBT), who assumed the clouds were in pressure equilibrium with a hot intergalactic medium. As discussed in Section 1.6, this model required cloud temperatures of  $T \sim 3 \times 10^4$  K, corresponding to a minimum velocity dispersion of  $b \sim 22 \text{ km s}^{-1}$ . The typical number density and neutral fraction of hydrogen in the model were  $n(\text{H}) \sim 10^{-4} \text{ cm}^{-3}$  and  $n(\text{HI})/n(\text{H}) \sim 10^{-4}$  respectively, and the cloud diameter was assumed to be  $d \sim 10 \text{ kpc}$ .

### Low- $b$ Lyman $\alpha$ Lines

The first evidence for the existence of low- $b$  Lyman  $\alpha$  lines was found by Chaffee *et al.* (1983). They observed a small section of the Lyman  $\alpha$  forest of the QSO PHL957 at  $0.2 \text{ \AA}$  ( $12 \text{ km s}^{-1}$ ) resolution, finding a line with  $b = 14.5 \pm 2.5 \text{ km s}^{-1}$ . The line may have been an unidentified metal line, but if not it implied a Lyman  $\alpha$  cloud temperature  $T < 17000 \text{ K}$ . Such a temperature cannot be reconciled with the simplest physical models of the clouds because photoionisation equilibrium with the metagalactic ionising flux demands  $T \sim 3 \times 10^4 \text{ K}$ , as calculated by SYBT.

Carswell *et al.* (1984) later observed Q1101–264 at  $0.25 \text{ \AA}$  ( $20 \text{ km s}^{-1}$ ) resolution, finding several lines with  $b = 10\text{--}20 \text{ km s}^{-1}$  which could not be attributed to metals. However, the poor S/N ratio of the data did not constrain any fits to be confidently less than  $19 \text{ km s}^{-1}$ , corresponding to a cloud temperature  $T = 2 \times 10^4 \text{ K}$ , so this was not strong evidence for the existence of clouds cooler than the pressure-confined limits. Carswell *et al.* also pointed out that the large range of velocity dispersions evident in Lyman  $\alpha$  clouds ( $b \sim 15\text{--}55 \text{ km s}^{-1}$ ) was inconsistent with the joint hypotheses of pressure-confinement by the IGM and thermal equilibrium with the background ionising flux from QSOs. They raised the possibility that turbulence contributed significantly to the highest  $b$  values measured.

Pettini *et al.* (1990, PHSM) presented  $0.09 \text{ \AA}$  ( $7 \text{ km s}^{-1}$ ) resolution spectra of Q2206–199N, in which they found *most* Lyman  $\alpha$  lines had  $b < 20 \text{ km s}^{-1}$  and several had  $b < 10 \text{ km s}^{-1}$ . The median velocity dispersion was  $17 \text{ km s}^{-1}$ . In contrast to previous studies, PHSM fitted only a subset of the Lyman  $\alpha$  lines seen in the spectrum with Voigt profiles. The line sample was defined to include only those lines with “sufficiently well-defined profiles” which were not saturated. Lines with complex profiles were excluded because of the difficulty of deblending multiple components accurately. Saturated lines were excluded because the line parameters have large uncertainties (see Section 1.3.1).

PHSM applied their temperature constraints to an equilibrium photoionisation model and deduced that the coolest clouds seen in their data would have to be relatively dense ( $n(\text{H}) \sim 1 \text{ cm}^{-3}$ ) and neutral ( $n(\text{HI})/n(\text{H}) \sim 0.5$ ). This implied a linear size along the line-of-sight of  $d < 10^{-4} \text{ pc}$ , in stark contrast to the transverse size  $d \sim 10\text{--}50h^{-1} \text{ kpc}$  and more deduced from common absorption in spectra of gravitationally lensed images of QSOs (Foltz *et al.*, 1984; Smette *et al.*, 1992; Smette *et al.*, 1995, for example, see Section 1.6.1). The existence of lines with  $b$  values as

low as those seen in PHSM's data was seen as a serious problem for the cloud models proposed up to that time.

The discrepancy between observation and theory brought to light by PHSM resulted in several new models of the Lyman  $\alpha$  clouds, among them:

- **Expansion-cooled clouds.** Duncan *et al.* (1991) showed that clouds not in equilibrium with their surroundings, but expanding and cooling adiabatically, could become cool enough to be consistent with PHSM's observations, while remaining large enough to satisfy the transverse size constraints placed by QSO pair studies. Petitjean *et al.* (1993a) elaborated on the model, showing that velocity dispersions as low as  $b = 10 \text{ km s}^{-1}$  can be produced in lines of sight passing through the outer parts of large, expansion-cooled clouds.
- **Clouds cooled by the presence of heavy elements and molecular hydrogen.** Donahue and Shull (1991) presented such a model, but noted that it did not lead to clouds as large as the limits from observations of QSO pairs.
- **Cloud ionisation by dark matter decay.** Sciama (1991) showed that a model in which cosmological dark matter (specifically  $\tau$ -neutrinos) decays into photons can produce a metagalactic ionising spectrum with a shape that leads naturally to cool Lyman  $\alpha$  clouds. However, searches for a signature of this decay have failed (Davidsen *et al.*, 1991; Fabian *et al.*, 1991; Miralda-Escudé and Ostriker, 1992).

Rauch *et al.* (1993) pointed out that the selection criteria imposed by PHSM may have biased their results by preferentially excluding lines with large velocity dispersions. They identified some of the narrow Lyman  $\alpha$  lines in PHSM's data with metal absorption and also showed with simulations that fitting profiles to noisy data can produce spuriously low  $b$  values<sup>14</sup>. Rauch *et al.* concluded there was little evidence in PHSM's data for Lyman  $\alpha$  lines with  $b < 10 \text{ km s}^{-1}$  and that it was unlikely there were many lines with  $b < 15 \text{ km s}^{-1}$ . However, their analyses contained some flaws, such as lines being fitted in the known positions of simulated lines even when the S/N ratio of the simulated spectrum placed the line well below the detection limit. This procedure resulted in several of the spuriously low  $b$  values reported. In a real spectrum such lines would not be claimed, so the biases reported by Rauch *et al.* are somewhat exaggerated.

There have been further examples of narrow Lyman  $\alpha$  lines. Carswell *et al.* (1991, CLPW) found lines with  $b < 15 \text{ km s}^{-1}$  in the spectrum of Q1101–264, though not as many as PHSM found in their Q2206–199N spectrum. Rauch *et al.* (1992) found 12% of the Lyman  $\alpha$  lines in the spectrum of Q0014+813 had  $b < 20 \text{ km s}^{-1}$ , but the resolution of their spectrum did not allow lower  $b$  values to be established.

Giallongo *et al.* (1993) found that 36% of the Lyman  $\alpha$  lines in the spectrum of PKS 2126–158 had  $b < 20 \text{ km s}^{-1}$  and 14% had  $b < 10 \text{ km s}^{-1}$ . Even taking into account the possibility of unidentified metal lines and the fitting biases demonstrated

---

<sup>14</sup>A similar study has been carried out in this thesis, on the Cloudy Night QSO data, with similar results. See Chapter 3.

by Rauch *et al.* (1993), Giallongo *et al.* concluded there was a substantial number of narrow lines which could not be explained by equilibrium models. Cristiani *et al.* (1995) reached a similar conclusion in their study of Q0055–269, finding 25% of the Lyman  $\alpha$  lines in the spectrum with  $b < 20 \text{ km s}^{-1}$  and 12% with  $b < 10 \text{ km s}^{-1}$ .

In a high resolution study of the  $z_{\text{em}} = 4.5$  QSO BR 1033–0327, Williger *et al.* (1994) extended the redshift baseline for Lyman  $\alpha$  forest work beyond  $z_{\text{abs}} \sim 4$ . Their work produced some intriguing results:

- The  $b$  distribution of the Lyman  $\alpha$  clouds with  $3.7 < z_{\text{abs}} < 4.5$  showed a significant excess at values  $\sim 20 \text{ km s}^{-1}$  over distributions found at smaller redshifts.
- The proximity effect in this QSO implies a Lyman limit background flux at  $z \sim 4.2$  of  $J_{\nu} \sim 1\text{--}3 \times 10^{-22} \text{ erg cm}^{-2} \text{ s}^{-1} \text{ Hz}^{-1} \text{ sr}^{-1}$ , a factor of  $\sim 10$  lower than most estimates at  $z \sim 2.5$ . Williger *et al.* proposed this lower flux as a possible cause for the lower  $b$  values observed.

Although initial evidence for the existence of low- $b$  Lyman  $\alpha$  lines was tentative and data analysis effects are known to bias measured  $b$  values somewhat, the continued presence of significant numbers of low- $b$  lines in recent high-quality data indicates that there are certainly some Lyman  $\alpha$  lines with  $b \sim 10\text{--}20 \text{ km s}^{-1}$ . Therefore at least some of the clouds cannot conform to a simple equilibrium photoionisation model and a more complex physical description is required.

### The $b$ – $N$ Correlation

The possible existence of a correlation between the velocity dispersion and column density of Lyman  $\alpha$  lines first came to prominence with the study of Q2206–199N by PHSM. They showed there was a strong correlation between the values of  $b$  and  $\log N$  for the absorbing clouds. PHSM went on to state that there was no immediate physical basis for expecting cloud temperature to increase systematically with  $N(\text{H I})$ . They concluded it was more likely that the correlation was caused by an increase in macroscopic motions with  $N(\text{H I})$ . This then suggested the possibility that *all or most* of the clouds had temperatures similar to those implied by the lowest  $b$  values:  $T \sim 5000\text{--}10\,000 \text{ K}$ .

In their re-analysis of PHSM’s Q2206–199N data, Rauch *et al.* (1993) also examined the reality of the  $b$ – $N$  correlation. Their simulations showed that a set of lines with uncorrelated  $b$  and  $N$  parameters and typical S/N ratios would produce an artificial correlation when fitted using their automated line-fitting techniques. However, they did not quantify the strength of the induced correlation and the flaws mentioned above (page 121 in Section 6.4) were also present in this study. An analysis of this effect has also been performed on the Cloudy Night QSO data in Chapter 3, using interactive fitting procedures, and a full discussion of its implications for the possible reality of a  $b$ – $N$  correlation is presented in Section 6.4.3.

No more rigorous studies of the possible correlation have been published, and it has been neither conclusively proven nor falsified. However, several authors have

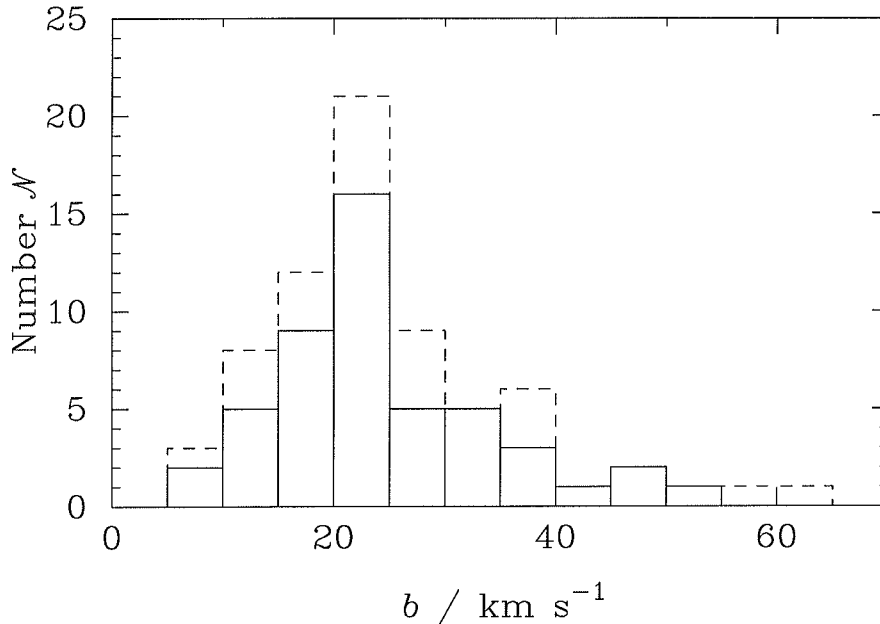


**Figure 6.5** Distribution of velocity dispersions for Lyman  $\alpha$  lines in the spectrum of Q1101–264. The solid histogram shows the lines with well-determined parameters, the dashed histogram shows all the Lyman  $\alpha$  lines.

pointed out the conspicuous absence of Lyman  $\alpha$  lines with high column densities and low velocity dispersions (Carswell *et al.*, 1984; PHSM; CLPW; Giallongo *et al.*, 1993; Cristiani *et al.*, 1995). Low  $b$  values appear to be present only in low column density HI clouds, and this behaviour must have some physical basis related to their morphology and/or confinement.

#### 6.4.1 Velocity Dispersion Distribution Results

Just as in the analysis of HI column densities, there are some absorption lines for which accurate velocity dispersions are difficult to obtain. The  $b$  values of lines in the saturated part of the curve-of-growth are not well-constrained by profile fitting, and some unsaturated lines are either too noisy or too heavily blended to allow  $b$  to be determined confidently. The Voigt profile parameters of saturated lines in the spectra of Q1101–264 and Q2348–147 are not given in the line lists (Tables B.6 and B.8 in Appendix B), while the parameters of lines which are ill-determined because of noise or blending are given but marked as uncertain.

The distribution of  $b$  values for the Lyman  $\alpha$  lines measured in the spectra of Q1101–264 and Q2348–147 are shown in Figures 6.5 and 6.6 respectively. In each case, the well-determined  $b$  values are shown as a solid histogram and the overlaid dashed histogram shows the distribution including the uncertain values.

Adding the uncertain  $b$  values to the distribution does not change the overall shape greatly. The main difference for both objects is the addition of a few points

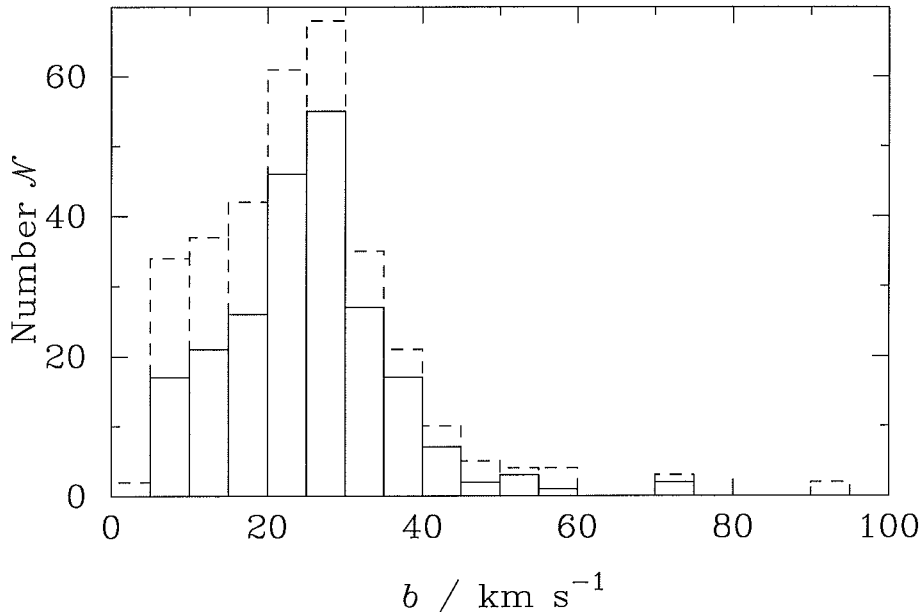


**Figure 6.6** Distribution of velocity dispersions for Lyman  $\alpha$  lines in the spectrum of Q2348–147. The solid histogram shows the lines with well-determined parameters, the dashed histogram shows all the Lyman  $\alpha$  lines.

with  $b$  higher than any of the well-determined  $b$  values. These large velocity dispersions are the result of fitting a single component to broad, noisy features in the spectra. Such features could be blends of narrower components, but this cannot be determined without data of higher S/N ratios. Given that very few of the well-determined fits have  $b > 40 \text{ km s}^{-1}$ , it is likely that the lines fitted with these high  $b$  values are indeed blends.

Another effect is that a large fraction of the lines in the spectrum of Q2348–147 with  $b < 20 \text{ km s}^{-1}$  have ill-determined fit parameters. This is primarily because the S/N ratio of the spectrum is poor blueward of Lyman  $\beta$  emission and narrow lines appear in noisy areas, where the line shapes become distorted and difficult to fit confidently. Broader lines in noisy regions cover more pixels, so the line shape is easier to discern.

The median and mean velocity dispersions for the full samples of Lyman  $\alpha$  lines in Q1101–264 and Q2348–147, as well as those for the subsamples of lines with well-determined parameters, are shown in Table 6.5, together with some values from other authors. The values of  $b_{\text{median}}$  and  $b_{\text{mean}}$  for the QSOs studied here are remarkably similar, near  $24 \text{ km s}^{-1}$ . Giallongo *et al.* (1993) and Cristiani *et al.* (1995) found similar values in their studies of PKS 2126–158 and Q0055–269. The values for Q2206–199N are significantly lower. The sightline to this object may probe an atypical region of space<sup>15</sup>. The median and mean  $b$  in the study of

<sup>15</sup>The issue of non-representative sightlines has been raised in Section 6.3.2. It is discussed in more detail in Section 8.2.

**Table 6.5** Median and mean velocity dispersions for samples of Lyman  $\alpha$  lines from the literature and in the spectra of Q1101–264 and Q2348–147.

Object	$z_{\text{abs}}$ range	Sample	No. lines	$b_{\text{median}}$ (km s $^{-1}$ )	$b_{\text{mean}}$ (km s $^{-1}$ )	Ref. <sup>1</sup>
Q2206–199N	2.07–2.56		41	17	17.3 $\pm$ 1.4	a
Q1101–264	1.84–2.15		70	33	33.9 $\pm$ 1.7	b
Q0014+813	2.70–3.27		166	33	36.0 $\pm$ 1.2	c
PKS 2126–158	2.91–3.17		97	26	26.7 $\pm$ 1.5	d
Q0055–269	2.96–3.54		249	26	28.4 $\pm$ 0.9	e
Q1101–264	1.79–2.15	All Lyman $\alpha$	70	23	24.5 $\pm$ 1.3	f
		Well-determined	49	23	24.0 $\pm$ 1.4	
Q2348–147	2.07–2.94	All Lyman $\alpha$	328	23	24.3 $\pm$ 0.7	
		Well-determined	224	25	24.7 $\pm$ 0.7	

Notes:

<sup>1</sup> References: (a) PHSM. (b) CLPW. (c) Rauch *et al.* (1992). (d) Giallongo *et al.* (1993). (e) Cristiani *et al.* (1995). (f) This work.

Q1101–264 by CLPW and the study of Q0014+813 by Rauch *et al.* (1992) stand out as anomalously high. These two studies used identical, automated data reduction techniques, which differ from those of the other studies, so the difference in  $b$  values may be a systematic effect imposed by the analysis procedures.

The higher redshift lines in the spectrum of Q2348–147 show no significant difference in mean velocity dispersion to the lower redshift lines of Q1101–264, so there is no evidence from these data for any evolution in typical  $b$  values with epoch. It would be difficult to investigate this possibility by combining the results of this work with those published elsewhere because of the differences in data reduction methods used. Nonetheless, an examination of the data in Table 6.5 reveals the possibility of a weak trend in the sense of  $b$  becoming smaller at lower redshift. The mean  $b$  values for PKS 2126–158, Q0055–269, Q1101–264 (from this work), and Q2348–147 are all consistent with such a trend. The anomalous values from Q2206–199N, Q1101–264 (from CLPW), and Q0014+813 do not conform to the possible trend set by the other data, but the Q1101–264 (CLPW) and Q0014+813  $b_{\text{mean}}$  values alone show a trend in the same sense. Overall, the data are too sparse to allow a confident statement of any evolutionary effect on Lyman  $\alpha$  cloud velocity dispersions.

With coverage of the Lyman  $\beta$  region of Q2348–147, there is a chance of confirming the identity of some narrow lines as H I. Unfortunately, the Lyman  $\beta$  region is quite noisy and none of the Lyman  $\beta$  lines corresponding to unsaturated Lyman  $\alpha$  lines with  $b < 20$  km s $^{-1}$  can be detected. The only possible confirmation of narrow H I lines occurs in the saturated Lyman  $\alpha$  feature at 4443 Å (lines 278–280 in Table B.8 and Figure A.5). In Lyman  $\beta$  this feature breaks up into three components near 3749 Å (lines 6–8), with velocity dispersions  $b = 10 \pm 2, 10 \pm 2, 19 \pm 3$  km s $^{-1}$  respectively. These lines appear to be constrained reasonably, but the noise level

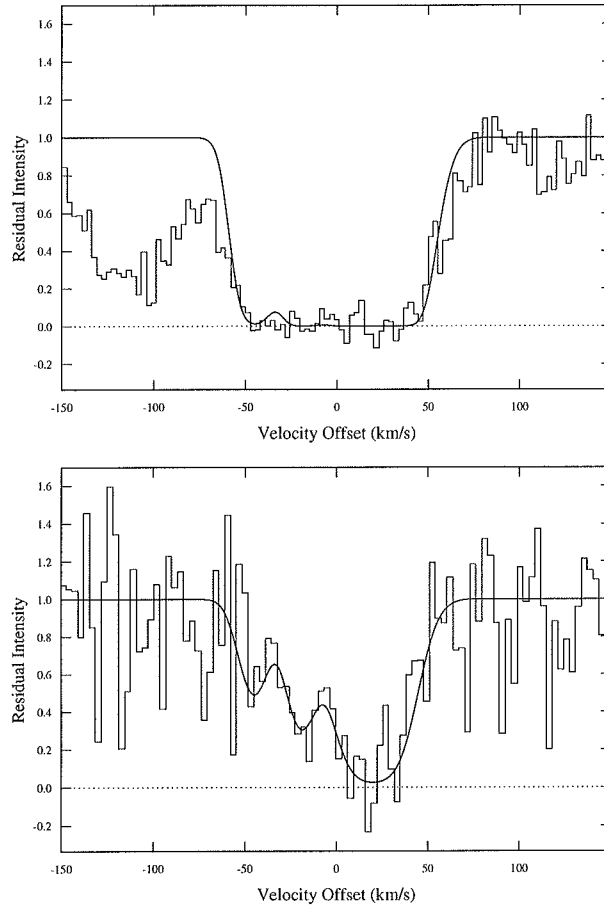


**Figure 6.7** Fits to the Lyman  $\alpha$  and Lyman  $\beta$  lines which show narrow Lyman  $\beta$  lines in the spectrum of Q2348–147. *Top:* The saturated Lyman  $\alpha$  complex at 4443 Å, with three-component fit as given in Table B.8. *Bottom:* The corresponding Lyman  $\beta$  region, near 3749 Å, plotted on the same velocity scale, showing the three components in Lyman  $\beta$ .

near the Lyman  $\beta$  lines is high. It is possible that the velocity dispersions have been underestimated, but it is difficult to reconcile the data with  $b$  values as high as  $20 \text{ km s}^{-1}$  for lines 6 and 7. The fits to these lines are shown in Figure 6.7.

The general absence of lines with high column density and low velocity dispersion evident in all published QSO spectra to date means that data of higher S/N ratio are needed to secure a Lyman  $\beta$  confirmation for a single narrow Lyman  $\alpha$  line.

#### 6.4.2 $b$ – $N$ Correlation Results

The results of the  $b$ – $N$  correlation analyses for Q1101–264 and Q2348–147 are presented below.

**Table 6.6** Results of regression analyses between the measured  $b$  and  $\log N$  values for the Lyman  $\alpha$  lines in the spectra of Q1101–264 and Q2348–147. Note that the uncertainties in the fit parameters are correlated.

$b = A + B \log N$					
Object	Sample	No. lines	$A$	$B$	$r$
Q1101–264	All Lyman $\alpha$	70	$-145 \pm 11$	$12.7 \pm 0.5$	0.456
	Well-determined	49	$-151 \pm 15$	$13.1 \pm 0.5$	0.537
Q2348–147	All Lyman $\alpha$	328	$-160 \pm 5$	$13.5 \pm 0.3$	0.560
	Well-determined	224	$-154 \pm 5$	$13.0 \pm 0.4$	0.640

$N = A' b^{B'}$					
Object	Sample	No. lines	$A'$	$B'$	$r$
Q1101–264	All Lyman $\alpha$	70	$(9 \pm 8) \times 10^6$	$4.7 \pm 0.4$	0.545
	Well-determined	49	$(18 \pm 17) \times 10^6$	$4.6 \pm 0.5$	0.588
Q2348–147	All Lyman $\alpha$	328	$(11 \pm 5) \times 10^6$	$4.7 \pm 0.1$	0.555
	Well-determined	224	$(4 \pm 2) \times 10^6$	$5.1 \pm 0.2$	0.592

### Q1101–264

Various sets of the lines detected in the spectrum of Q1101–264 are shown plotted on the  $b$ – $\log N$  plane in Figure 6.8. Correlation analyses were carried out on the full set of Lyman  $\alpha$  lines and the subset with well-determined parameters (*i.e.* those not marked as uncertain in Table B.6). The results are shown in Table 6.6.

### Q2348–147

Various sets of the lines detected in the spectrum of Q2348–147 are shown plotted on the  $b$ – $\log N$  plane in Figure 6.9. Correlation analyses were carried out on the full set of Lyman  $\alpha$  lines and the subset with well-determined parameters (*i.e.* those not marked as uncertain in Table B.8). The results are shown in Table 6.6.

## 6.4.3 Discussion of Velocity Dispersion Results

The results of the velocity dispersion analysis serve to reinforce the important fact that there do appear to be Lyman  $\alpha$  lines with  $b \sim 10$ – $20 \text{ km s}^{-1}$ —too low to be explained by standard models of photoionised Lyman  $\alpha$  clouds in pressure equilibrium with a hot, tenuous IGM.

The study of the Cloudy Night QSO (Chapters 2 and 3) showed that, although some spuriously low  $b$  values could be produced by the line fitting procedures, the majority (66%) of fitted  $b$  values were within the uncertainty estimates and only 11% of the  $b$  values were underestimated by more than twice the uncertainty. In the full samples of Lyman  $\alpha$  lines fitted in the spectra of Q1101–264 and Q2348–147, 35%

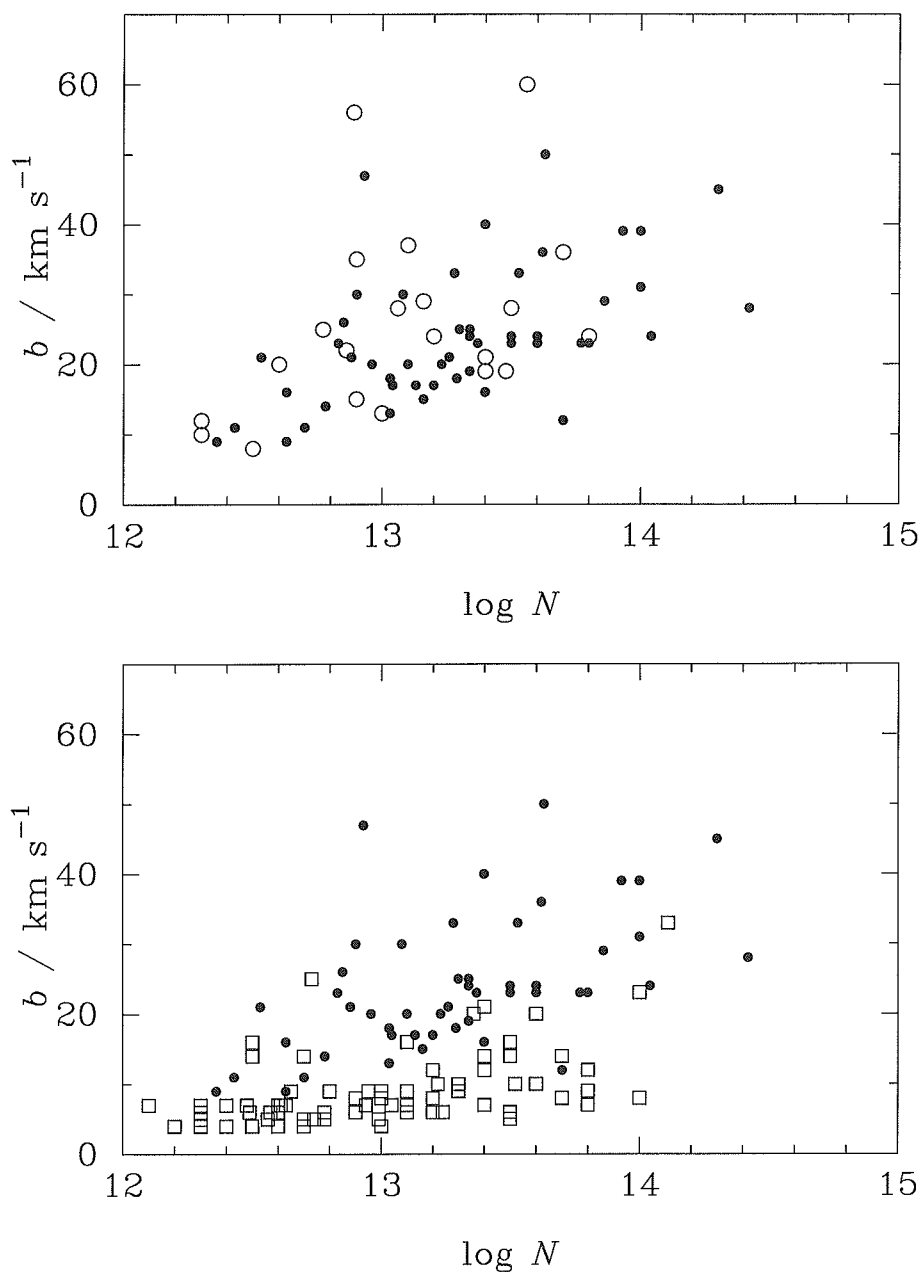


**Figure 6.8** Plot of line parameters from the spectrum of Q1101–264 in the  $b$ – $\log N$  plane. *Top:* Solid circles show Lyman  $\alpha$  lines with well-determined fits, open circles show Lyman  $\alpha$  lines with parameters marked as uncertain in Table B.6. *Bottom:* Solid circles show Lyman  $\alpha$  lines with well-determined fits, open squares show metal lines with well-determined fits. The  $\log N$  values for the metal lines are those which would be measured assuming the lines were caused by H I, *i.e.*  $\log N_{\text{Ly}\alpha}$  as given by Equation 2.2.

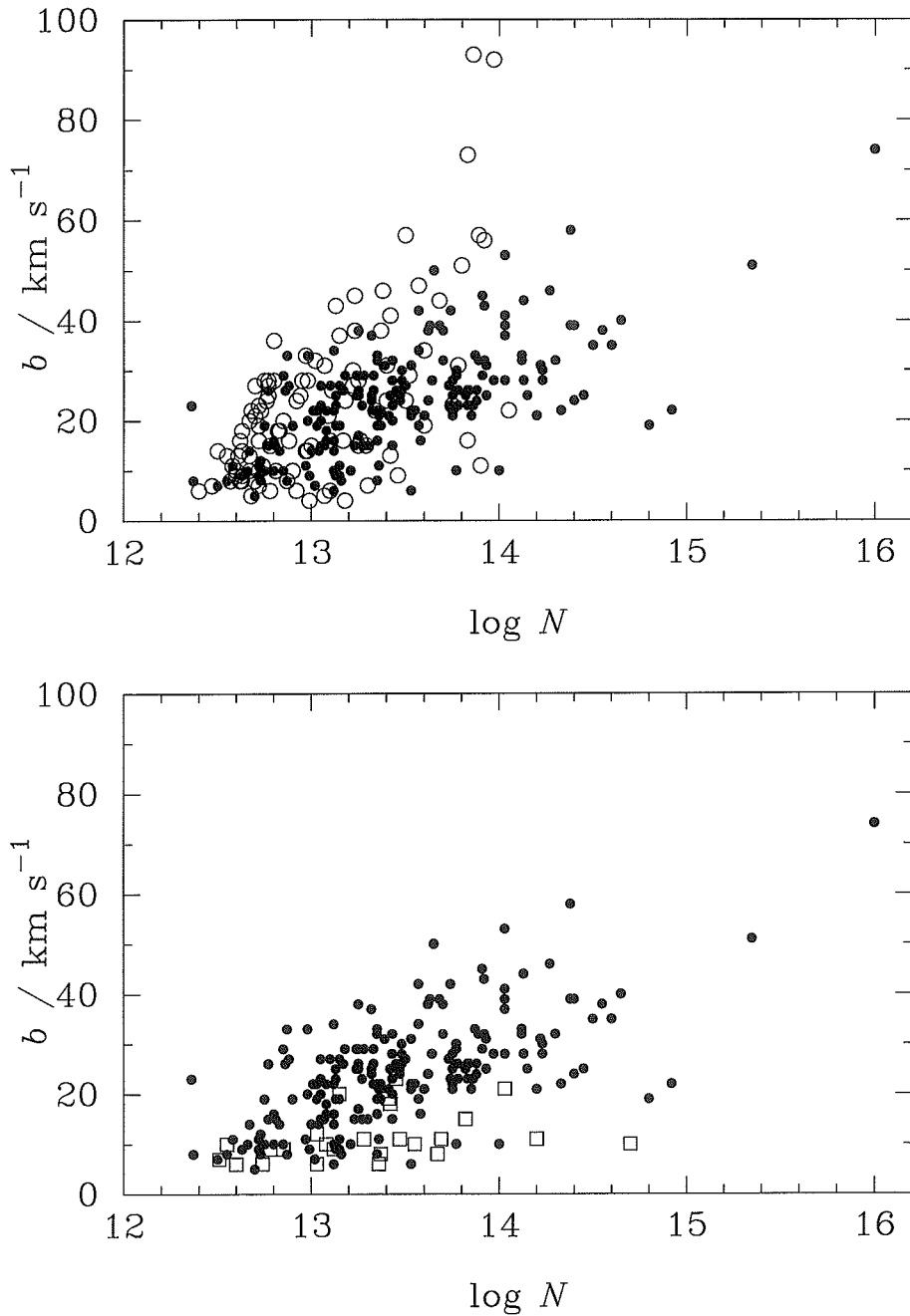


**Figure 6.9** Plot of line parameters from the spectrum of Q2348–147 in the  $b$ – $\log N$  plane. *Top*: Solid circles show Lyman  $\alpha$  lines with well-determined fits, open circles show Lyman  $\alpha$  lines with parameters marked as uncertain in Table B.8. *Bottom*: Solid circles show Lyman  $\alpha$  lines with well-determined fits, open squares show metal lines with well-determined fits. The  $\log N$  values for the metal lines are those which would be measured assuming the lines were caused by H I, *i.e.*  $\log N_{\text{Ly}\alpha}$  as given by Equation 2.2.

and 33% had  $b < 20 \text{ km s}^{-1}$ , respectively<sup>16</sup>. Giallongo *et al.* (1993) and Cristiani *et al.* (1995) found similar fractions of lines with  $b < 20 \text{ km s}^{-1}$  in recent work with good quality spectra. It is highly unlikely that all of these narrow lines could have been measured inaccurately, even given the known biases in profile fitting.

The CNQ study also showed that the largest likely amount of contamination of a Lyman  $\alpha$  sample by unidentified metal lines is  $\sim 20\%$ . Even assuming this extreme amount of metal contamination, the samples of Lyman  $\alpha$  lines for Q1101–264 and Q2348–147, as well as the samples of Giallongo *et al.* (1993) and Cristiani *et al.* (1995), contain substantially more lines with  $b < 20 \text{ km s}^{-1}$  than can be accounted for by unidentified metals.

Perhaps the strongest evidence for the reality of low- $b$  lines is the complex of lines constrained by Lyman  $\beta$  in the spectrum of Q2348–147 presented in Figure 6.7. This, together with the results of many authors over the past few years seems to indicate that low- $b$  lines do exist. Theoretical models must be able to explain velocity dispersions  $b \sim 10\text{--}20 \text{ km s}^{-1}$  in order to have any chance of successfully describing the physical state of the Lyman  $\alpha$  clouds.

### $b$ – $N$ Correlation Results

All of the Lyman  $\alpha$  line samples analysed show a significant correlation between  $b$  and  $\log N$ . The probabilities of observing the measured correlation coefficients in uncorrelated data are all exceedingly small ( $\ll 10^{-5}$ ). However, the results of Section 3.7.2 show that selection effects and measurement errors can substantially increase the apparent level of correlation between the line parameters.

The data for the Cloudy Night QSO (CNQ) and for Q1101–264 and Q2348–147 had similar S/N ratios and were analysed using the same techniques for line selection and profile fitting, so it is reasonable to assume that any biases present in the reduced data will be of similar magnitude. The correlation coefficients between  $b$  and  $\log N$  for the two real QSOs are similar in magnitude to those for the CNQ. The probabilities that uncorrelated data could give rise to such high correlation coefficients are also related to the number of data points in the samples. A value of  $r$  derived from a larger data sample has a smaller probability of occurring by chance than the same value derived from a smaller sample, and hence is more statistically significant as an indicator of correlation.

Of the CNQ and two real QSOs, the data sample from Q1101–264 was the smallest and also gave the smallest values of  $r$ . The observed correlation of  $b$  and  $\log N$  for this object is therefore no more significant than that seen for the CNQ. Since it has been shown that much of the correlation observed in the CNQ data is an artefact of the analysis procedure<sup>17</sup>, there is no evidence to support the hypothesis that the  $b$  and  $\log N$  values of Lyman  $\alpha$  lines in the spectrum of Q1101–264 are correlated. The S/N ratio of the Q1101–264 spectrum is somewhat higher than

<sup>16</sup>For the well-determined subsamples, the figures are 29% and 33%, respectively.

<sup>17</sup>The  $b$  and  $\log N$  values of the Lyman  $\alpha$  lines in the CNQ spectrum were actually correlated, as discussed in detail in Section 3.7.

that of the CNQ, so it is likely the line parameters were determined more accurately than those in the CNQ spectrum. However, there is still no firm evidence to suggest that the line parameters are *not* correlated at some level.

The data sample for Q2348–147 is larger than that for the CNQ, with a similar mean S/N ratio, and also produces a higher correlation coefficient, implying a correlation of much greater significance. The  $b$  and  $\log N$  data for Q2348–147 therefore suggest a stronger correlation than exists in the CNQ data. The CNQ data are known to be correlated, so this is evidence for the existence of an intrinsic correlation between  $b$  and  $\log N$  in the Lyman  $\alpha$  lines along the sightline to Q2348–147. This correlation is implied *despite the fact that selection and line-fitting effects are known to produce an apparent correlation*, because these effects are present in the analyses of both the CNQ and Q2348–147. It is difficult, however, to assess the strength of such an intrinsic correlation except perhaps by more extensive simulations.

It is important to note there is general agreement on the fact that there are no Lyman  $\alpha$  lines of large column density ( $\log N \gtrsim 13.5$ ) and low velocity dispersion ( $b \lesssim 20 \text{ km s}^{-1}$ ). This has been confirmed by several authors (Giallongo *et al.*, 1993; Cristiani *et al.*, 1995, for example). The selection effects and measurement errors studied by Rauch *et al.* (1993) and in Chapter 3 of this thesis cannot account for this observed absence of low- $b$ , high- $N$  Lyman  $\alpha$  lines. That there are so few lines with  $b < 20 \text{ km s}^{-1}$  and  $\log N > 13.5$ , while there are substantial numbers with  $b < 20 \text{ km s}^{-1}$  and  $\log N < 13.5$ , implies there must be some physical relationship between  $b$  and  $N$ . The challenge is to quantify and interpret this relationship correctly.

### Possible Causes of a $b$ – $N$ Correlation

The existence of an observed correlation between  $b$  and  $N$  requires an explanation. Some possibilities are examined below.

- The correlation may be entirely an artefact of the line fitting procedures. This position was argued by Rauch *et al.* (1993), based on their analyses of simulated data. However, their analysis techniques contained flaws (described on page 121). The similar but more thorough analysis of the Cloudy Night QSO presented in Chapters 2 and 3 and the data of Q2348–147 indicate that there is a significant correlation between  $b$  and  $N$  which is not simply an artefact of the fitting procedure.
- The thermal velocity dispersion of the Lyman  $\alpha$  clouds covers a relatively small range, say  $10$ – $20 \text{ km s}^{-1}$ , and bulk motions of the clouds contribute the remainder. PHSM put forward this hypothesis, claiming that it was more reasonable for bulk motions, rather than temperature, to be correlated with cloud mass. If this is the case, a physical model which produces uniformly low temperature clouds is required. The only such models imply clouds of very small dimensions ( $< 1 \text{ pc}$ ), in contrast to growing evidence that the sizes are

$\gtrsim 10h^{-1}$  kpc (Foltz *et al.*, 1984; Smette *et al.*, 1992, for example) and possibly as large as  $50h^{-1}$  kpc (Smette *et al.*, 1995).

- The Lyman  $\alpha$  clouds have outer regions cooled by adiabatic expansion, with hotter interiors. In this model, detailed by Petitjean *et al.* (1993a), gravity dictates the density profile of the clouds and the core remains at ionisation equilibrium temperatures  $T > 2 \times 10^4$  K while the outer regions expand with surface speeds  $v = 5\text{--}15 \text{ km s}^{-1}$  and cool to  $T \sim 5000$  K. With such clouds, both  $b$  and  $N$  decrease as the line of sight passes further from the centre of the cloud.

The expanding surface model of Petitjean *et al.* (1993a) also explains the existence of Lyman  $\alpha$  lines with  $b$  as low as  $10 \text{ km s}^{-1}$ , while being consistent with the cloud sizes inferred from studies of correlated absorption in the lines of sight to gravitationally lensed QSOs and QSO pairs. The model does require the *ad hoc* assumption of some dark matter to provide a deep enough gravitational potential to confine the clouds to a diameter  $20h^{-1} < d < 50h^{-1}$  kpc, consistent with best fits to the observations of Sargent *et al.* (1982), Shaver and Robertson (1983), and Foltz *et al.* (1984). If no dark matter is present, the cloud diameters become  $\sim 130h^{-1}$  kpc, nearly three times greater than the  $2\sigma$  lower limit of  $50h^{-1}$  kpc calculated by Smette *et al.* (1995).

A possible problem for the expanding cloud model is that the proposed surface speeds are high enough to disperse the clouds on a timescale of  $\sim 10^9$  years. Since there are still observable Lyman  $\alpha$  clouds at  $z_{\text{abs}} \sim 0$  (Morris *et al.*, 1991), expanding clouds must be replenished or their rate of expansion must slow down at low redshifts. If the IGM expands adiabatically, then its pressure  $P_{\text{IGM}}$  drops with decreasing redshift according to  $P_{\text{IGM}} \propto (1+z)^5$  (Duncan *et al.*, 1991). This might be expected to imply a considerable slowing of the expansion speeds over time, but Petitjean *et al.* (1993a) consider the expansion speed and external pressure to be virtually independent over the range  $1.8 < z < 2.5$ , so the effects at lower redshifts are not clear.

Given the constraints placed on the Lyman  $\alpha$  clouds from observations over the past few years, the expanding cloud model of Petitjean *et al.* appears to give the best description for the physical conditions of the clouds. The true situation, however, is likely to be more complex than any of the models so far put forward.

## 6.5 How Many Populations of Clouds?

The idea of unifying various groups of objects so they can be studied as a single population is a powerful one. To this end, Tytler (1987a), and later Giallongo (1991) published results claiming to unify the populations of Lyman  $\alpha$  clouds and metal line systems into a single population with consistent properties. Their results relied on measurements and interpretations of the distributions of Lyman  $\alpha$  lines.

Tytler argued for a single population based on a determination of an apparently smooth power law of constant slope  $\beta$  (defined in Equation 6.1) describing the neutral hydrogen column density distribution of Lyman  $\alpha$  clouds, Lyman limit systems (LLS) and metal line clouds. However, Bechtold (1987) criticised Tytler's method of estimating column densities for LLS. Using refined estimates, Bechtold showed a single power law was a poor fit to the  $\log N$  distribution, as subsequently verified by Sargent *et al.* (1989) and Lu *et al.* (1991). Carswell *et al.* (1987) and Webb *et al.* (1992) noted a distinct break in the distribution, with the slope becoming flatter at low values of  $\log N$ . Petitjean *et al.* (1993b) found a single power law was a very poor fit to the  $\log N$  distribution, and even a double power law did not appear to be satisfactory. Petitjean *et al.* concluded the distribution was highly complex, unlike Tytler's single power law hypothesis.

Giallongo (1991) supported the concept of a unified absorber population by presenting evidence that higher column density clouds (producing lines of higher  $W_0$ ) evolved in redshift more slowly than lower  $N(\text{HI})$  clouds. Giallongo assembled a sample of lines from the spectra of Q2000–330 (Carswell *et al.*, 1987), Q0420–388 (Atwood *et al.*, 1985), Q2206–199N (PHSM), and Q1101–264 (CLPW). After removing lines within  $8h^{-1}$  Mpc of each QSO to avoid the proximity effect, the calculated values of  $\gamma$  (defined in Equation 6.3) were  $2.91 \pm 0.99$  for  $0.14 < W_0 < 0.2 \text{ \AA}$ ,  $1.05 \pm 0.85$  for  $0.3 < W_0 < 0.5 \text{ \AA}$ , and an intermediate value for the intermediate subsample. Such a trend of less rapid evolution for stronger lines was required if the population was to be unified with the metal line clouds, which have Lyman  $\alpha$  lines of still higher  $W_0$  and which show no significant redshift evolution.

Giallongo's finding of differential evolution is not well supported. Trèvese *et al.* (1992) used a large sample of data from the literature to show that differential evolution apparently occurs in the sense of stronger lines evolving more rapidly than weaker ones (the opposite of Giallongo's finding), but then argued that this was a spurious effect caused by line blending at intermediate spectral resolutions (in agreement with the findings of Liu and Jones, 1988). They concluded the true variation of  $\gamma$  would remain uncertain until more high-resolution data became available.

Srianand and Khare (1994) criticised Giallongo's result because it was based on only four QSO sightlines, with no overlap in  $z_{\text{abs}}$ , so peculiarities in individual sightlines would grossly affect the global result<sup>18</sup>. Srianand and Khare demonstrated this with several four-QSO subsamples of their eight-QSO sample, deriving differential evolution in both senses from different subsamples<sup>19</sup>. With their full sample, they concluded  $\gamma$  was higher for stronger Lyman  $\alpha$  lines, contrary to Giallongo's result. Bechtold (1994) also found that  $\gamma$  was higher for stronger lines, in a sample of 34 intermediate-resolution QSO spectra, but conceded the result may be caused by line blending, as described by Liu and Jones (1988). However, the HST spectrum of 3C 273 obtained by Morris *et al.* (1991) extended the redshift baseline down to

<sup>18</sup>It is also worth noting that Giallongo's sample was far from homogeneous, using data of resolutions from  $7\text{--}35 \text{ km s}^{-1}$ , and that there is significant incompleteness in the range  $0.14 < W_0 < 0.2 \text{ \AA}$  used for one of the  $\gamma$  calculations.

<sup>19</sup>See also Section 8.2, which discusses the effects of differences between QSO sightlines.

$z_{\text{abs}} \sim 0.1$ , and Bechtold noted her results were consistent with the numbers and strengths of Lyman  $\alpha$  lines seen in those data.

Despite these problems, Tytler and Giallongo stated their major reservation about the unified scheme was the difference in clustering properties between the Lyman  $\alpha$  and metal line clouds. This is discussed in more detail in Section 7.1.4, in the Chapter on Lyman  $\alpha$  cloud clustering.

Some support for at least partial unification was presented by Lanzetta *et al.* (1995), who found galaxies associated with several Lyman  $\alpha$  forest clouds at low redshift (see Section 1.6.2). Since metal line systems are generally believed to arise in galaxy haloes, this implies that some Lyman  $\alpha$  clouds could belong to the same general class of objects. However, there are still problems with a fully unified picture, and it remains likely that a significant fraction of Lyman  $\alpha$  clouds arises in a class of objects distinct from that of the metal line clouds.

### 6.5.1 Different Populations of Clouds

Another intriguing possibility suggested by earlier work and strengthened by the present study is that the Lyman  $\alpha$  clouds may belong to more than a single population of objects. The accumulated evidence is presented below.

- Petitjean *et al.* (1993b) presented a model of the column density distribution of Lyman  $\alpha$  clouds. In order to reproduce the features of the observed  $N$  distribution, they required three distinct populations of clouds, corresponding to different physical models, overlapping in their  $N$  ranges.
- Calculations of the cloud number density evolution parameter  $\gamma$  based on high- $z$  observations and the low- $z$  HST data of Morris *et al.* (1991) suggest that there may be differential evolution of the Lyman  $\alpha$  clouds with column density. This has been discussed in detail in Section 6.3. Any differential evolution of absorbers with column density may be a consequence of the existence of distinct populations of clouds, either because of different physical conditions or because some clouds are being partially replenished over time, as suggested by Morris and van den Bergh (1994).
- Observations of fields around HST spectroscopic target QSOs by Lanzetta *et al.* (1995) showed that a fraction of at least  $0.35 \pm 0.10$  and more likely  $0.65 \pm 0.18$  of Lyman  $\alpha$  forest systems at  $z_{\text{abs}} < 1$  are associated with extended haloes of luminous galaxies. However, there were also several Lyman  $\alpha$  systems which could not be associated with galaxies, and Morris *et al.* (1993) found a clear case of a Lyman  $\alpha$  absorber in the line of sight to 3C 273 with no galaxy brighter than an absolute blue magnitude  $M_B = -18$  within  $3.8h^{-1}$  Mpc. It appears therefore that some Lyman  $\alpha$  absorbers are associated with galaxies while others are not.
- Evidence for the reality of the correlation between the  $b$  and  $N$  values of Lyman  $\alpha$  clouds was presented in Section 6.4. It may be that the correlation does

not arise from correlated physical properties of the clouds, but rather reflects the different properties of two or more populations of absorbing objects. If there is a mixture of clouds confined by pressure or by the gravitational potentials of dark matter haloes and adiabatically expanding clouds, for example, the confined clouds will produce absorption lines with  $b \geq 22 \text{ km s}^{-1}$ , while the expanding clouds will produce lower  $b$  value lines. Perhaps the amount of dark matter required to confine the clouds gravitationally is present in clouds with  $\log N > 13.5$  and not in some lower  $N$  clouds. This could account for the absence of lines with  $b < 20 \text{ km s}^{-1}$  and  $\log N > 13.5$ .

- The results of this thesis on the clustering of low column density Lyman  $\alpha$  clouds along the sightline to Q1101–264 (described in Chapter 7) suggest that there is some difference between the clustering properties of high- and low- $N$  clouds. This might be expected if the lowest  $N$  clouds detected in the spectrum of Q1101–264 trace a population distinct from the higher  $N$  clouds. Morris and van den Bergh (1994) showed that low- $N$  absorbers may arise in tidal debris in small galaxy clusters. If this is the case, one would expect this population of absorbers to show some clustering.

All of these results point to the existence of distinct classes of Lyman  $\alpha$  absorbers. It is likely that no single model can adequately explain all of the observational features of the Lyman  $\alpha$  forest, and indeed none so far has been able to do so. A good description of the absorber properties requires a model with multiple populations, such as that of Petitjean *et al.* (1993b), and even this may be too simple a scheme to describe every type of absorber seen in the Lyman  $\alpha$  forest.

## 6.6 Summary

The distributions of the Lyman  $\alpha$  cloud column densities and velocity dispersions, as well as the number density of clouds with redshift, have been examined using data from Q2206–199N (PHSM), Q1101–264, Q2348–147, and data of similar quality from the literature.

The column density distributions for the three QSOs were fitted to Equation 6.1. Q2348–147 provided the tightest constraint, with a power law index of  $\beta = 1.55 \pm 0.05$  for unsaturated Lyman  $\alpha$  lines above the completeness limit. This value has been corrected for the line blanketing effect, which was shown to alter significantly the measured value of  $\beta$  when the data sample consisted of several hundred lines or more. No evidence was found for a change in the value of  $\beta$  with redshift over the range  $1.79 < z_{\text{abs}} < 2.94$ .

The best estimate of  $\beta$  was significantly lower than the previously accepted canonical value of  $\beta \sim 1.7$  (Carswell *et al.*, 1987, CLPW), but consistent with new work at high spectral resolution by Giallongo *et al.* (1993) and possibly consistent with results of Cristiani *et al.* (1995) and Songaila *et al.* (1995) (depending on the magnitudes of the unaccounted-for line blanketing effect and unstated uncertainty,

respectively, in these studies). This lower value of  $\beta$  may be sufficient to account for the observations of Barcons and Webb (1991) and Webb *et al.* (1992) without appealing to clustering of Lyman  $\alpha$  clouds or Gunn-Peterson H I absorption at  $z_{\text{abs}} \sim 4$ , respectively, as invoked by those studies.

The distribution of the Lyman  $\alpha$  cloud number density with redshift was examined over the range  $0.008 < z_{\text{abs}} < 2.919$  using the three QSOs studied in this work plus the data of Morris *et al.* (1991) from the low-redshift QSO 3C 273. The fitted values of the evolutionary index  $\gamma$  (defined in Equation 6.3) had large uncertainties, but the inclusion of the 3C 273 data produced a significantly lower value of  $\gamma$  than using the high redshift data alone. This confirmed, using data of similar spectral resolutions, a trend reported by Morris *et al.* but based on data of disparate resolutions. It implies that the rapid rate of disappearance of the Lyman  $\alpha$  clouds observed at high redshifts slows down markedly at low redshifts.

A suggestion that clouds forming lower equivalent width lines evolve more slowly than clouds forming higher  $W_0$  lines was found, though this could not be established with the limited data set. Such a trend, if demonstrated conclusively, would provide important clues to the physical processes involved in the evolution of the Lyman  $\alpha$  clouds.

The velocity dispersion distributions of Q1101–264 and Q2348–147 were analysed. A substantial fraction of the fitted Lyman  $\alpha$  lines had  $b < 20 \text{ km s}^{-1}$ , consistent with recent work by Giallongo *et al.* (1993) and Cristiani *et al.* (1995), and too low to be explained by standard photoionisation models of Lyman  $\alpha$  clouds in pressure equilibrium with a hot intergalactic medium. Additionally, the coverage of the Lyman  $\beta$  region of the Q2348–147 spectrum provided the strongest evidence yet for the reality of H I absorption lines with  $b \sim 10 \text{ km s}^{-1}$ —a strong Lyman  $\alpha$  line was seen to be composed of at least three narrow components in the corresponding Lyman  $\beta$  feature.

The possible correlation of cloud velocity dispersion and column density was explored. Considering the results of the Cloudy Night QSO simulation (Chapters 2 and 3), the data from Q2348–147 provided evidence for the reality of some correlation between the two parameters, even taking into account the biases introduced in the line fitting procedures. The existence of low velocity dispersions and a correlation between  $b$  and  $N(\text{H I})$  support the cloud model of Petitjean *et al.* (1993a), in which the outer regions of the clouds expand adiabatically.

Consideration was given to the possibility that there may be more than one population of Lyman  $\alpha$  clouds. Evidence collected from the literature and from work presented in this thesis suggests the existence of at least two, and possibly more, distinct populations of objects which give rise to the Lyman  $\alpha$  forest absorption lines. Separate populations are required to explain observations such as those of Morris *et al.* (1993) and Lanzetta *et al.* (1995), which show that some Lyman  $\alpha$  clouds are associated with luminous galaxies while others are not, and multiple populations would naturally lead to the results seen in other analyses.

Overall, the properties of the Lyman  $\alpha$  forest clouds studied in this work point to a physical model with multiple populations of clouds, at least some of which are

not in a confined equilibrium state. The full picture of the physical conditions of the clouds is certainly more complicated and not yet fully understood, but a good deal of progress has been made with the recent wave of high resolution observations.

# Chapter 7

## Clustering in the Lyman $\alpha$ Forest

### 7.1 Introduction

The first analysis of the clustering properties of Lyman  $\alpha$  clouds was performed by Sargent *et al.* (1980) (SYBT). They had a sample of five QSOs, two observed at a spectral resolution of  $0.6 \text{ \AA}$  FWHM and three at  $\sim 1.5 \text{ \AA}$  FWHM<sup>1</sup>. The QSO spectra contained absorption features from Lyman  $\alpha$  systems in the range  $1.7 < z_{\text{abs}} < 3.3$ .

SYBT introduced the two-point correlation function (Peebles, 1980, and also defined and discussed in Section 7.2) as a means of studying clustering of Lyman  $\alpha$  clouds. They determined that there was no significant clustering in their sample on all scales<sup>2</sup> ranging from  $\sim 1.5\text{--}150h^{-1}$  Mpc (velocity splittings<sup>3</sup> of  $300\text{--}30\,000 \text{ km s}^{-1}$ ). This result was in sharp contrast to the strong clustering seen in galaxy distributions at low redshift (Bahcall, 1988, and references therein) and the expected galaxy correlation function at the redshifts examined. It was also strikingly different to the clustering properties of the metal line systems seen in the spectra of the same QSOs, which were strongly clustered on scales up to  $\sim 2h^{-1}$  Mpc.

Based on this finding, SYBT conjectured that the Lyman  $\alpha$  clouds formed “a genuine intergalactic population unconnected with galactic haloes”. The metal line systems were expected to arise in galactic haloes, where metal enrichment through stellar processing would have taken place, based on their obvious spatial clustering (Bahcall, 1975; Sargent, 1977). It was clear (at the time) that the metal and Lyman  $\alpha$  systems formed two populations, with distinctly different properties.

The dramatic difference in the clustering properties of the Lyman  $\alpha$  and metal

---

<sup>1</sup>SYBT state in their paper that the AAT Cassegrain spectra have a resolution of  $0.8 \text{ \AA}$  FWHM, but this figure is inconsistent with the camera and gratings used.

<sup>2</sup>All distances in this Chapter are comoving distances calculated for an Einstein-de Sitter cosmology with a Hubble parameter  $H_0 = 100h \text{ km s}^{-1} \text{ Mpc}^{-1}$ . An Einstein-de Sitter cosmology is a standard Friedman cosmology with deceleration parameter  $q_0 = 1/2$ . See Section 7.2 for a definition of comoving distances.

<sup>3</sup>Instead of using comoving distances, many authors refer to “velocity splittings”, which are apparent differences in velocity caused by the Hubble flow. Velocity splittings are defined in Section 7.2.

line systems became firmly established with further analyses of the Lyman  $\alpha$  systems by Carswell and Rees (1987), Bechtold (1987), Bechtold and Schectman (1989), and Webb and Barcons (1991) and of the metal systems by Young *et al.* (1982), Crofts (1985), Sargent *et al.* (1988), and Heisler *et al.* (1989). It is important to note that these studies all used intermediate-resolution data, and the Lyman  $\alpha$  line samples were complete only down to a limiting rest equivalent width of  $W_0 \sim 0.36 \text{ \AA}$ .

Another implication of the apparent lack of clustering in the Lyman  $\alpha$  forest is the constraint it places on pressure fluctuations in the intergalactic medium (IGM). Assuming the Lyman  $\alpha$  clouds are pressure confined, Webb and Barcons (1991) showed the random distribution of clouds implied a maximum IGM pressure fluctuation of  $\Delta P/P \lesssim 0.14$  ( $2\sigma$  upper limit) on scales  $\gtrsim 1.5h^{-1} \text{ Mpc}$  ( $\gtrsim 300 \text{ km s}^{-1}$ ).

### 7.1.1 Small-Scale Clustering of Lyman $\alpha$ Clouds

Although it is generally accepted that the Lyman  $\alpha$  clouds do not cluster nearly as strongly as metal line systems, there have been several claims and counter-claims of significant structure in the cloud distribution.

Webb (1987) claimed a detection of weak but significant clustering on scales  $\lesssim 1.5 \text{ Mpc}$  ( $300 \text{ km s}^{-1}$ ) using high-resolution spectra ( $\sim 0.25 \text{ \AA}$  FWHM) of 13 QSOs with Lyman  $\alpha$  systems in the range  $1.9 < z_{\text{abs}} < 2.8$ . Webb's study was the first to use such high spectral resolution, which allowed the separations of closely spaced absorption lines (within  $\sim 4 \text{ \AA}$ ) to be discerned. Any structure on these scales is missed at lower resolutions because of line blending. The strength of the clustering signal measured by Webb, although formally significant, was much less than that measured for either metal line absorption systems or luminous galaxies at low redshift.

Webb's measurement was supported by Barcons and Webb (1991) with a sample of lines with  $W_0 \geq 0.36 \text{ \AA}$  from 20 QSOs and Chernomordik (1995) with a sample of lines with  $\log N(\text{H I}) \geq 14$  (corresponding to  $W_0 \gtrsim 0.2 \text{ \AA}$  for lines with  $b \sim 20\text{--}30 \text{ km s}^{-1}$ )<sup>4</sup> from three QSOs. Barcons and Webb used their result to explain an observed discrepancy between the equivalent width distributions of Lyman  $\alpha$  lines in intermediate- and high-resolution spectra. An enhancement of line blending at small separations in intermediate-resolution spectra caused by the claimed small-scale clustering was shown to be able to account for the differences in the  $W_0$  distributions. Barcons and Webb took this as further indirect evidence for the reality of Webb's clustering claim<sup>5</sup>.

There has also been criticism of Webb's result. Bechtold and Schectman (1989)

<sup>4</sup>Unfortunately, different authors are not consistent in choosing either equivalent width, column density, or even velocity dispersion limits when defining their samples. These three variables share a non-linear relationship which is explained in Section 1.3.1.

<sup>5</sup>An alternative explanation for the differences in the  $W_0$  distributions seen by Barcons and Webb (1991) was that the column density distribution power law index  $\beta$  was  $\sim 1.5$ , significantly lower than the value of 1.7 taken from other observations. As discussed in Sections 6.2 and 6.2.2, the value  $\beta \sim 1.5$  may in fact be more accurate.

pointed out that the inclusion of a small number of metal lines in a Lyman  $\alpha$  line sample used to analyse clustering properties would create an artificial clustering signal, because the metal line clouds are strongly clustered. They conjectured that Webb's clustering detection may have been caused by contamination of the line sample by unidentified metal lines. The result by Barcons and Webb (1991), which at first sight seems to be strong evidence in favour of small-scale Lyman  $\alpha$  clustering, may also be subject to the effects of unidentified metal lines (though what effect this would have on their calculations is unclear). Additionally, the sample of high-resolution data used by Barcons and Webb was small, consisting of only 2 QSOs at spectral resolution  $\sim 0.5 \text{ \AA}$ , Q0420–388 ( $z_{\text{em}} = 3.12$ ) (Atwood *et al.*, 1985) and Q2000–330 ( $z_{\text{em}} = 3.78$ ) (Carswell *et al.*, 1987), and one at  $\sim 0.1 \text{ \AA}$  resolution, Q1101–264 ( $z_{\text{em}} = 2.14$ ) (Carswell *et al.*, 1991). As discussed in Sections 6.3.2 and 8.2, the sightlines to these objects may be far from typical. The simulations by Barcons and Webb, using these data as inputs, could therefore have produced misleading results. Finally, as discussed in Sections 6.2 and 6.2.2, the column density power law index  $\beta = 1.7$  assumed by Barcons and Webb in their calculations may be incorrect. Overall, the evidence presented for small-scale clustering in the sightlines to samples of QSOs is suggestive but not compelling.

### Clustering Detection by Cross-Correlations

Crotts (1989) measured the cross-correlation function for Lyman  $\alpha$  clouds in the sightlines to four closely spaced QSOs (within an area of sky  $440''$  in diameter; with  $1.9 < z_{\text{abs}} < 2.6$ ) and claimed a detection of significant clustering for separations  $\lesssim 0.7h^{-1} \text{ Mpc}$  ( $100 \text{ km s}^{-1}$ ). This detection was claimed for lines with  $W_0 > 0.4 \text{ \AA}$ , and Crotts stated that a sample with a lower equivalent width limit of  $W_0 > 0.2 \text{ \AA}$  did not show clustering. The spectral resolution of Crotts's data was fairly low:  $1.8\text{--}3.6 \text{ \AA}$  FWHM.

Webb (1989) rightly criticised Crotts's study as inconclusive because of its poor use of statistics, but neglected to point out that his conclusion was derived entirely from a visual inspection of the two-point cross-correlation function, with no attempt made to calculate uncertainty estimates or significance levels. When one considers that Crotts's result derives from such an analysis of a histogram in which most of the bins contain 2–6 data points<sup>6</sup>, one can only conclude that the claim is dubious at best.

In a study similar to that of Crotts, Elowitz *et al.* (1995) found no significant correlations between Lyman  $\alpha$  clouds with  $1.66 < z_{\text{abs}} < 1.90$  on the lines of sight to a different group of four QSOs. Their observations were at slightly higher resolution than those of Crotts ( $1.0\text{--}2.0 \text{ \AA}$  FWHM), but of poorer S/N ratio.

<sup>6</sup>Other histograms presented in Crotts (1989) have bins in which the *full* span of counts is 0–6 and 0–3! This is a dramatic example of choosing bins which are far too small to be meaningful. At these low counts, the Poisson noise is of the same order as any possible signal, so drawing reliable conclusions is next to impossible.

### Clustering in Single QSO Sightlines

An intriguing detection of small-scale clustering was presented by Rauch *et al.* (1992) in a study of the  $z_{\text{em}} = 3.38$  QSO 0014+813 at a resolution of  $0.4 \text{ \AA}$ . Their full sample of 295 Lyman  $\alpha$  lines showed no evidence for clustering, but the two-point correlation function for a subsample consisting of lines with velocity dispersions  $b \leq 20 \text{ km s}^{-1}$  showed a  $2.6\sigma$  excess of line pairs with  $\Delta v \leq 250 \text{ km s}^{-1}$  (corresponding to  $\sim 1.3h^{-1} \text{ Mpc}$ ) and marginal evidence for clustering to  $\sim 1000 \text{ km s}^{-1}$  ( $\sim 5h^{-1} \text{ Mpc}$ ). Rauch *et al.* considered it unlikely that the clustering signal was caused by unidentified metal lines. Although the existence of weak clustering on small scales in the Lyman  $\alpha$  forest was reasonably well accepted at the time<sup>7</sup>, all previous clustering detections were based on studies of several QSOs. Rauch *et al.*'s result was the first claimed detection of clustering in the clouds along a single sightline. Other single high-resolution spectra had not shown any evidence of clustering (Pettini *et al.*, 1990). It is important to note that, because of the apparent correlation of  $b$  with  $\log N(\text{HI})$  in Rauch *et al.*'s data<sup>8</sup>, their low  $b$  lines tended to have low  $\log N(\text{HI})$  values. In other words, they had found a trend for stronger clustering with decreasing line strength.

Cristiani *et al.* (1995) presented a seemingly contradictory result, based on a  $0.3 \text{ \AA}$  FWHM resolution spectrum of Q0055–269 ( $z_{\text{em}} = 3.66$ ). In a sample of 178 Lyman  $\alpha$  lines with  $\log N(\text{HI}) \geq 13.3$  (corresponding to  $W_0 \gtrsim 0.1 \text{ \AA}$  for lines with  $b \gtrsim 15 \text{ km s}^{-1}$ ) they measured a  $5.7\sigma$  detection of clustering on scales  $\lesssim 1.7h^{-1} \text{ Mpc}$  ( $350 \text{ km s}^{-1}$ ). For a subsample with  $\log N(\text{HI}) \geq 13.8$  ( $W_0 \gtrsim 0.2 \text{ \AA}$  for  $b \gtrsim 20 \text{ km s}^{-1}$ ) they claimed a stronger clustering signal on the basis of the magnitude of the two-point correlation function in a (differently sized!) bin with  $\Delta v < 100 \text{ km s}^{-1}$  ( $\lesssim 0.5h^{-1} \text{ Mpc}$ ). They thus claimed a trend of stronger clustering with *increased* line strength, stating that this was consistent with the expectation that Lyman  $\alpha$  clouds with higher  $N(\text{HI})$  (and hence higher mass) should be more strongly clustered because of gravitational interactions.

The inconsistency between the results of Rauch *et al.* and Cristiani *et al.* can be resolved as follows: Although Cristiani *et al.*'s strong line sample had a higher correlation function value than their full line sample, the uncertainty was also higher and it was only a  $4.9\sigma$  detection (compared to  $5.7\sigma$  for the full sample). In addition, the calculated uncertainties were based on Poissonian statistics, which become increasingly unreliable when the correlation function magnitude becomes larger (see Section 7.2.2), and the method of calculating the correlation function itself was not optimal (see the subsection *The Importance of Using the Observed Number of Lines* on page 147). A recalculation of the correlation functions, using Cristiani *et al.*'s published line list and improved uncertainty estimates (Mo *et al.*, 1992a, see also Section 7.2.2) was performed; the results are given in Table 7.1. The results show that the clustering signal, although stronger for the  $\log N(\text{HI}) \geq 13.8$  subsample in

<sup>7</sup>Based on the results of Webb (1987) and Barcons and Webb (1991), but see the criticisms of their results earlier in this Section.

<sup>8</sup>This effect is discussed in Section 6.4.

**Table 7.1** Recalculation of two-point correlation functions from the data of Cristiani *et al.* (1995).

Sample	Velocity scale	$\xi$	Significance
$\log N \geq 13.3$	$\Delta v < 150 \text{ km s}^{-1}$	$0.40 \pm 0.16$	$2.5\sigma$
	$\Delta v < 350 \text{ km s}^{-1}$	$0.92 \pm 0.29$	$3.2\sigma$
$\log N \geq 13.8$	$\Delta v < 150 \text{ km s}^{-1}$	$0.87 \pm 0.38$	$2.3\sigma$
	$\Delta v < 350 \text{ km s}^{-1}$	$1.66 \pm 0.59$	$2.8\sigma$

Notes:

 $150 \text{ km s}^{-1}$  corresponds to  $\sim 0.7h^{-1} \text{ Mpc}$  at  $z \sim 3.5$ . $350 \text{ km s}^{-1}$  corresponds to  $\sim 1.7h^{-1} \text{ Mpc}$  at  $z \sim 3.5$ .

each of the two velocity ranges, is less significant in each case because of the higher uncertainties. Also, the significance of the clustering is substantially less than that claimed by Cristiani *et al.*, because of the different (and more reliable) uncertainty estimates. In fact, given the recalculated uncertainties, the clustering detections become only marginal.

### 7.1.2 Voids in the Lyman $\alpha$ Cloud Distribution

Apart from studying the overall clustering properties of the Lyman  $\alpha$  cloud population, using the two-point correlation function or similar tools, there has been something of an “industry” built around the finding and statistical analysis of so-called “voids” in the cloud distribution. In this sense, a void is a contiguous region of the sampled sightline containing no absorbers and, in some way, indicative of a non-uniform cloud distribution.

Carswell and Rees (1987) found no evidence for voids in the distribution of Lyman  $\alpha$  lines with  $\log N(\text{HI}) \gtrsim 13.5$  in intermediate-resolution spectra of Q0420–388 (Atwood *et al.*, 1985) ( $2.59 < z_{\text{abs}} < 3.08$ ) and PKS 2000–330 (Carswell *et al.*, 1987) ( $3.21 < z_{\text{abs}} < 3.75$ ). Crofts (1987), however, found a void of comoving size  $\sim 30h^{-1} \text{ Mpc}$  with a claimed 99% significance when analysing the same data. The different conclusions of these authors demonstrates the need for care when using post-hoc statistics to examine the significance of voids.

Ostriker *et al.* (1988) presented a critical reappraisal of the significance of the void claimed by Crofts. Ostriker *et al.* demonstrated that the *a priori* probability of detecting a gap in the Lyman  $\alpha$  line distribution as large as, or larger than, the gap found by Crofts was  $\sim 45\%$ . Going on to examine a sample of 18 QSOs from Bajtlik *et al.* (1988) ( $1.7 < z_{\text{abs}} < 3.8$ ,  $W_0 \geq 0.36 \text{ \AA}$ ), Ostriker *et al.* concluded there was no evidence for any voids inconsistent with a Poissonian line distribution in any object. Bechtold and Schectman (1989) added a comment that “structure” perceived by the human eye is often merely a psychological effect imposed on random data and demonstrated this with a diagram (similar to Figure 7.6 later in this Chapter). The unspoken implication was that Crofts’s result was more due to wishful thinking than

good statistics.

Crotts (1989) rebutted the critique of Ostriker *et al.*, claiming they had not corrected properly for line blending effects. In the same paper, Crotts also presented new evidence for a void of lines with  $W_0 > 0.4 \text{ \AA}$  of size  $\sim 30h^{-1} \text{ Mpc}$  at  $z = 2.4$ . Employing an unexplained probability calculation, Crotts claimed an *a priori* probability of  $\sim 4 \times 10^{-3}$  for finding such a void in a random distribution of Lyman  $\alpha$  clouds.

Duncan *et al.* (1989) addressed the problem of line blending by developing a theoretical model of the blending effects and a statistical method for dealing with them. They concluded there was only marginal evidence in published data for the existence of voids. Based on the data published to that time, Duncan *et al.* calculated the filling factor of any voids of size  $10\text{--}70h^{-1} \text{ Mpc}$  to be  $< 20\%$  with 99% confidence.

A separate re-analysis of the “void” in the Q0420–388 spectrum was presented by Bi *et al.* (1989). Using a different statistical technique, they concluded the Crotts (1987) gap was a real departure from a random distribution with 98% confidence.

Bechtold (1990) complicated the debate over the Q0420–388 void by showing there were detectable Lyman  $\alpha$  lines within the Crotts gap. Given her higher S/N data of the object, Bechtold found the largest observable gap of absorption features to have a  $\sim 60\%$  probability of occurring by chance.

Cristiani *et al.* (1995) found two voids of size  $\sim 20h^{-1} \text{ Mpc}$  in the spectrum of Q0055–269. They used Monte Carlo simulations to establish the probability of seeing a single void of such size as  $\sim 2\%$ , but then erroneously used this figure to calculate a joint probability of  $\sim 2 \times 10^{-4}$  for seeing both gaps in the one spectrum<sup>9</sup>. A more accurate probability could have been obtained by examining their ensemble of simulations for instances of two gaps.

### 7.1.3 Enhanced Ionisation Zones

Kovner and Rees (1989) adopted a theoretical approach to so-called “clearings” in the Lyman  $\alpha$  forest—wavelength intervals containing only lines of reduced column densities—caused by ionisation from a compact radiation source near the line of sight. They estimated one such clearing should be present in each 5–10 QSO sight-lines, but Duncan *et al.* (1989) concluded that the filling factor of clearings would be  $\sim 10^{-4}$  and they would therefore be very difficult to find unless pairs of QSOs with very small separations on the sky were examined specifically.

In a study of a tight grouping of four QSOs, Crotts (1989) found no evidence for increased ionisation in the vicinity of the foreground QSOs and concluded that these, if not all, QSOs produced no isotropic ionising radiation sufficient to produce clearings.

---

<sup>9</sup>It is not clear how Cristiani *et al.* obtained a joint probability  $2 \times 10^{-4} < (0.02)^2$ . Perhaps it was by lowering the probability of the second gap to account for the established existence of the first gap, but this is not explained.

Soon afterwards, Bechtold (1990) presented tentative evidence for voids caused by foreground ionising sources in two QSOs, Q1623+269 ( $z_{\text{em}} = 2.61$ ) (Sargent *et al.*, 1982) and Q0302–003 ( $z_{\text{em}} = 3.29$ ). The spectrum of each QSO contains a gap of Lyman  $\alpha$  absorption features centred near the emission redshift of a nearby foreground QSO. Using the empirical line density function of Duncan *et al.* (1989), corrected for line blending, Bechtold calculated the probabilities of these voids existing by chance as 36% and 0.3% respectively. Bechtold concluded the first case could have been a redshift coincidence between a void of no real significance and the foreground QSO, but the second probability was low enough to suggest that enhanced ionisation had played a part in the formation of the void.

Dobrzycki and Bechtold (1991) used a Monte Carlo simulation technique to recalculate the chance probability of finding a void of the size of that seen in the spectrum of Q0302–003. This technique is far more robust than appealing to the (ill-determined) line density function, and produced a probability of  $\sim 2 \times 10^{-4}$ , indicating the void was highly significant. Dobrzycki and Bechtold noted the foreground QSO was displaced in redshift from the void by  $\Delta z \sim 0.05$ , corresponding to a comoving distance of  $\sim 9h^{-1}$  Mpc. This was used as evidence either for anisotropic UV emission from the foreground QSO (a view supported by the findings of Crotts, 1989) or for a recent “turning on” of the foreground QSO (because of light-travel time effects).

### 7.1.4 Other Developments

Since SYBT discovered the lack of any strong clustering of the Lyman  $\alpha$  clouds, this fact has been used as evidence of their intrinsic difference to the metal line system clouds.

When Tytler (1987a), and later Giallongo (1991) published results claiming a unified population of Lyman  $\alpha$  clouds and metal line systems (see Section 6.5), their major reservation was the difference in clustering properties of the two groups of objects. Addressing the problem the clustering data posed to their theories, Tytler and Giallongo proposed that the clustering strength of the Lyman  $\alpha$  clouds may also increase with increasing cloud mass (and hence column density). Such a trend was subsequently reported by Cristiani *et al.* (1995) but, as already pointed out (Section 7.1.1), the reliability of the result is not well established. As discussed in Section 6.5, there are also other reasons for doubting the existence of a unified cloud population, so there is no reason to require such a clustering trend.

The recent finding of Lanzetta *et al.* (1995) that at least  $0.35 \pm 0.10$  of Lyman  $\alpha$  forest systems at  $z_{\text{abs}} \lesssim 1$  arise in luminous galaxies (see Section 1.6.2) also has consequences for the clustering properties of the Lyman  $\alpha$  clouds. Since galaxies are known to cluster strongly, one would expect that associated Lyman  $\alpha$  clouds would also display such clustering. Lanzetta *et al.* present some possible explanations for this observational discrepancy. Firstly, they state that the extended gaseous envelopes of galaxies which give rise to Lyman  $\alpha$  absorption systems might not be present in regions of high galaxy density, as first proposed by Morris *et al.* (1993).

Secondly, the sample of low-redshift Lyman  $\alpha$  clouds so far observed is not sufficient to detect clustering of the expected strength, and the Lyman  $\alpha$  clustering strength may also be weakened by clouds which are not associated with galaxies. Lanzetta *et al.*'s result does not apply to high-redshift Lyman  $\alpha$  clouds, so the weakness of clustering there is not problematic.

## 7.2 The Two-Point Correlation Function

One of the simplest statistics used in studying the clustering properties of astronomical objects is the two-point correlation function,  $\xi$  (Peebles, 1980). In terms of comoving distance, the two-point correlation function is defined by

$$\xi(d, \Delta d) = \frac{N_{\text{obs}}(d, \Delta d)}{N_{\text{exp}}(d, \Delta d)} - 1, \quad (7.1)$$

where  $N_{\text{obs}}(d, \Delta d)$  is the number of pairs of objects observed with comoving separations between  $d$  and  $d + \Delta d$ , and  $N_{\text{exp}}(d, \Delta d)$  is the number of such pairs expected in a random spatial distribution of such objects. The ‘‘pairs of objects’’ are simply all possible pairings of two distinct objects in the sample. For a sample of  $n$  objects, the number of such pairs is

$$N_{\text{pairs}} = \binom{n}{2} = \frac{n(n-1)}{2}. \quad (7.2)$$

Many researchers calculate single sightline correlation functions in terms of ‘‘velocity splittings’’ given by

$$\Delta v = \frac{c|z_2 - z_1|}{1 + (z_1 + z_2)/2}, \quad (7.3)$$

where  $z_1$  and  $z_2$  are the redshifts of a pair of objects. This calculation is based on an assumption that the redshift differences are due to real differences in velocity, rather than to the cosmic expansion. It should be noted, though, that some small redshift differences between absorption features may be caused by peculiar velocities. If such objects are at the same cosmological redshift, then Equation 7.3 correctly gives the peculiar velocity difference, when  $\Delta v \ll c$ .

Instead of velocity splittings, I have consistently used comoving distance (in a specific cosmology) because for the most part the redshift differences being considered are too large to be caused by reasonable peculiar velocities. The distances used are those appropriate to an Einstein-de Sitter cosmology with a Hubble parameter  $H_0 = 100h \text{ km s}^{-1} \text{ Mpc}^{-1}$ . The comoving distance between two objects at redshifts  $z_1$  and  $z_2$  in such a cosmology is given by

$$d = \frac{2c}{H_0} \left| \frac{1}{\sqrt{1+z_1}} - \frac{1}{\sqrt{1+z_2}} \right|. \quad (7.4)$$

The practice of some authors of using only a small-distance approximation of this equation has been avoided.

### 7.2.1 Producing Two-Point Correlation Functions

Calculating a two-point correlation function from a set of observed data is not always straightforward. Counting the number of object pairs with separations lying within any given range is easy enough. Determining the number of expected pairs from a random distribution is a different matter. Producing a theoretical function for the expected random distribution may be possible in simple cases, but in others may not be practical. In particular, the case of absorption lines in spectra is especially problematical.

The problem with QSO absorption spectra is that the detection sensitivity for absorption lines is far from uniform across the spectral range, for the following reasons:

- The S/N ratio varies with wavelength.
- If one is interested in the correlation function of only a subset of the absorption lines, such as the Lyman  $\alpha$  lines, the metal lines, or even a subsample of one of these groups selected by some criterion, then the presence of the other lines raises the possibility that some lines of interest may be blanketed by lines not in the sample and so missed. (Additionally, there is the complication of separating the samples, such as the metals from the Lyman  $\alpha$  lines; see Section 5.2.)
- Lines in close proximity may be blended to such a degree that they appear as a single line.
- For echelle spectra, there are often distinct gaps in the wavelength coverage between the echelle orders.

In order to account for these effects, the expected random distributions for all correlation functions in this thesis were calculated by Monte Carlo simulations.

In each simulation, the pseudo-random number generating routine `ran1` from Press *et al.* (1988) was used to produce a uniform random deviate bounded by the lower and upper wavelength limits of the spectrum in question. Any deviate satisfying any of the following criteria was rejected:

- If the deviate lay within visually determined exclusion zones near lines not included in the correlation analysis (such as metal system lines, or Lyman  $\alpha$  lines not included in a subsample). Such zones were judged to be the regions near such lines where other lines possibly present would not be detected because of being subsumed into the structure of the absorption feature. Tests showed that any small uncertainties in judging these exclusion limits, or even ignoring them altogether, made almost no discernible difference to the outcome.
- If the deviate lay within a pre-determined wavelength separation from an already generated random deviate in the same simulation. This separation was chosen to be slightly smaller than the smallest observed wavelength separation. Removing this correction significantly affected the results only in the first comoving separation bin ( $0-5h^{-1}$  Mpc or  $0-10h^{-1}$  Mpc in the plots shown

in this Chapter), increasing the value of  $\xi$ , and variations in the chosen cut-off affected this bin proportionately.

- If the deviate lay within any of the inter-order gaps of the real echelle spectrum.

Unfortunately, the S/N ratio effect is much more difficult to deal with. Doing so would require an assessment of the S/N ratio at each point in the spectrum and varying the probability density function as some appropriate function of the S/N ratio. Since the effort required is large and the expected improvement in accuracy slight, this was not done.

Another effect with possible consequences for the correlation results is that the number of Lyman  $\alpha$  lines per unit redshift is known to evolve strongly with redshift (see Section 6.3). A number density power law of the form

$$\frac{d\mathcal{N}}{dz} \propto (1+z)^\gamma, \quad (7.5)$$

with  $\gamma \sim 2$  forms a satisfactory fit to most published data with  $W_0 \gtrsim 0.2 \text{ \AA}$  (but note the possibility that  $\gamma$  may be a function of  $z_{\text{abs}}$  and  $W_0$ ; Section 6.3). Again, this change in number density with redshift could be taken into account when assigning random line positions by changing the probability density function of the random deviate being used. However, this complicates the task and the correlation function is almost totally insensitive to the value of  $\gamma$  used. Cristiani *et al.* (1995) confirm that a choice of  $\gamma = 0$ , corresponding to a uniform random deviate as used here, produces values of  $\xi$  within 0.02 of those produced when  $\gamma \sim 2$ . Any possible improvement in accuracy by adopting the empirical number density variation is thus insignificant, since the uncertainties in the values of  $\xi$  calculated here are an order of magnitude or more larger than this value.

When a number of satisfactory deviates equal to the number of real absorption lines in the analysis had been produced, the number of simulated line pairs in each comoving separation bin were counted. This process was repeated many times and the mean simulated pair count in each bin was used as  $N_{\text{exp}}(d, \Delta d)$ .

The entire simulation process needed to be performed for each sample of lines, and for each choice of comoving distance bin size. In each set of simulations for a given sample and bin size, a different value was chosen for the seed integer of the routine `ran1`, and the routine was not reseeded during the calculation of any set.

### The Importance of Using the Observed Number of Lines

It is important to note that in each simulation the number of randomly chosen lines was equal to the number observed in the appropriate data sample. A possible alternative would have been to use a number of lines consistent with an empirical line density function calculated from observations of several QSOs. Webb and Barcons (1991) used this method when confirming the lack of structure on scales  $\gtrsim 1.5h^{-1} \text{ Mpc}$  while Webb (1987) and Barcons and Webb (1991) did not state which method they used when reporting and confirming, respectively, significant clustering

signals on scales  $\lesssim 1.5h^{-1}$  Mpc. Cristiani *et al.* (1995) used an empirical line density function derived from their data for Q0055–269 alone.

The expected number of line pairs in each bin,  $N_{\text{exp}}(d, \Delta d)$ , is a strong function of the number of lines in the spectrum because for  $n$  lines the number of line pairs is  $O(n^2)$ , from Equation 7.2. Therefore, if the number of lines in the simulations used to calculate  $N_{\text{exp}}(d, \Delta d)$  is not equal to the number observed in the spectrum being examined, a serious under- or over-estimation of the value of  $\xi$  may result. For example, if a given sightline contains more than the mean number of lines estimated from the empirical function (but still within a reasonable statistical fluctuation and distributed randomly), the number of observed line pairs in each bin will, on average, be greater than the empirically expected value and  $\langle \xi \rangle$  will be  $> 0$  merely as an artefact of the calculation rather than because of any real clustering. This has also been pointed out qualitatively by Bechtold (1990).

The magnitude of this effect can be estimated by differentiating Equation 7.2 and taking finite differences to give:

$$\Delta N_{\text{pairs}} \simeq (n - 1/2)\Delta n. \quad (7.6)$$

For a Poisson distribution, typically  $\Delta n \simeq \sqrt{n}$ , giving

$$\frac{\Delta N_{\text{pairs}}}{N_{\text{pairs}}} \simeq \frac{2\sqrt{n}(n - \frac{1}{2})}{n(n - 1)} \sim \frac{2}{\sqrt{n}}, \quad (7.7)$$

taking a large  $n$  approximation for the final expression. Now, a first approximation for the  $1\sigma$  uncertainties in  $\xi$  is given by the Poissonian expression in the expected number of line pairs,

$$\sigma(N_{\text{exp}}(d, \Delta d)) = \sqrt{N_{\text{exp}}(d, \Delta d)} \quad (7.8)$$

(this expression is similar to one often used to derive uncertainties for  $\xi$ , which is discussed in Section 7.2.2). Since Equation 7.7 also applies to the number of line pairs in *each* bin (*i.e.* we can replace the subscript “pairs” with the subscript “exp” and add the bin specifier), we see that

$$\frac{\Delta N_{\text{exp}}(d, \Delta d)}{N_{\text{exp}}(d, \Delta d)} \simeq 2 \frac{\sigma(N_{\text{exp}}(d, \Delta d))}{N_{\text{exp}}(d, \Delta d)}. \quad (7.9)$$

So, if the number of lines used in simulations to calculate the values of  $N_{\text{exp}}(d, \Delta d)$  comes from some empirical function and not the number of lines actually observed in the particular spectrum being analysed, a typical variation in the number of lines seen in the spectrum will result in a mean systematic error in  $\xi$  of twice the expected uncertainty! The importance of using the observed number of lines for each calculation is clear.

## 7.2.2 Uncertainty Estimates in Correlation Functions

As with all experimental quantities, it is necessary to have some idea of the uncertainties when measuring a value for the two-point correlation function.

If the distribution of absorption lines in a spectrum is Poissonian, then (using the notation from Equation 7.1) the variance in the number of observed line pairs is

$$\text{var}(N_{\text{obs}}(d, \Delta d)) = N_{\text{obs}}(d, \Delta d) \quad (7.10)$$

(this is similar to Equation 7.8, except here we are concerned with the observed numbers of line pairs, not with possible variation in the expected numbers). It follows from Equation 7.1 that the standard deviation of the two-point correlation function is

$$\sigma(\xi(d, \Delta d)) = \frac{\sqrt{N_{\text{obs}}(d, \Delta d)}}{N_{\text{exp}}(d, \Delta d)}. \quad (7.11)$$

This calculation assumes a Poissonian distribution (*i.e.*  $N_{\text{obs}}(d, \Delta d) \sim N_{\text{exp}}(d, \Delta d)$ ), so this can also be written as

$$\sigma(\xi(d, \Delta d)) \simeq (N_{\text{obs}}(d, \Delta d))^{-\frac{1}{2}} \simeq (N_{\text{exp}}(d, \Delta d))^{-\frac{1}{2}}. \quad (7.12)$$

This expression is used by some authors to calculate uncertainties in the value of  $\xi$ , but it is clear that it only holds when  $\xi \sim 0$ . When clustering is present, a different uncertainty calculation should be used.

Mo *et al.* (1992a) demonstrated that when weak clustering ( $|\xi| \lesssim 1$ ) is present, a more accurate formula for the  $1\sigma$  uncertainty in the correlation function is

$$\sigma(\xi(d, \Delta d)) = \left[ N_{\text{obs}}(d, \Delta d) + \frac{4(N_{\text{obs}}(d, \Delta d))^2}{n} \right]^{\frac{1}{2}} (N_{\text{exp}}(d, \Delta d))^{-1}, \quad (7.13)$$

where  $n$  is the total number of lines in the sample. Mo *et al.* dubbed this expression the “ensemble” uncertainty, to distinguish it from the Poissonian uncertainty. By comparing Equations 7.11 and 7.13, it can be seen that the Poissonian expression underestimates the uncertainties in  $\xi$  when weak clustering is present. It is therefore likely that some of the weak clustering results reported in the literature are slightly less significant than claimed—most fail to mention how their uncertainties are calculated or state that they are Poissonian.

When the clustering signal is strong ( $|\xi| \gtrsim 1$ ), the calculation of uncertainties becomes more difficult. Barrow *et al.* (1984) suggested using the method of bootstrap resampling (Efron and Tibshirani, 1986, and references therein) to estimate uncertainties in  $\xi$ .

The bootstrap method applied to the two-point correlation function involves forming a large number of “resamplings” of the data. Each resampling is a set of  $n$  absorption lines (with  $n$  equal to the actual number of lines in the data), chosen from the real line wavelengths at random, with replacement (*i.e.* each line may be chosen multiple times). The value of  $\xi$  is calculated for each resampling, and the standard deviation of  $\xi$  over all the resamplings is taken as the estimate for the  $1\sigma$  uncertainty in the value of  $\xi$  calculated from the real data.

Mo *et al.* (1992a) showed that bootstrap calculations provide good two-point correlation function uncertainties when  $|\xi| \gtrsim 1$ , but overestimate the uncertainties

when  $|\xi| \lesssim 1$ . They also derived an analytical formula for estimating the bootstrap uncertainties without performing the resampling calculations.

For the two-point correlation functions calculated in this Chapter, the following uncertainty estimates were used:

- When the calculated value of  $\xi(d, \Delta d)$  for a given bin was  $< 1$ , the ensemble uncertainty given by Equation 7.13 was used.
- When the calculated value of  $\xi(d, \Delta d)$  for a given bin was  $\geq 1$ , bootstrap resampling was used to calculate an uncertainty. Generally 200 resamplings were used. The formula given by Mo *et al.* to estimate the bootstrap uncertainty was not used.

The resulting  $1\sigma$  uncertainty is plotted as a positive deviation from  $\xi = 0$  in all the correlation function plots in this Chapter. The Poissonian uncertainties (Equation 7.11) are also shown on each plot, as a negative deviation from  $\xi = 0$ . The Poissonian uncertainties are included because they are accurate when  $\xi \sim 0$ , and for comparison purposes with other published correlation function plots.

A point to note is that none of the uncertainty estimates are accurate when  $\xi \sim -1$ . This is because the number of line pairs in the bin is very small. When  $\xi = -1$ , there are no line pairs at all, and all the uncertainty estimates become zero, which is clearly incorrect.

### 7.2.3 The Cloudy Night Result

A two-point correlation function clustering analysis was performed on the Cloudy Night QSO before Jenkins revealed any of the simulation's secret input parameters. This was done as a test of the reliability of both the computer programs used and of the correlation function as a method of determining the clustering properties of a sample of absorption lines.

The two-point correlation function was calculated for the sample of 224 Lyman  $\alpha$  lines in the CNQ. 5000 Monte Carlo simulations were used to generate the values of  $N_{\text{exp}}(d, \Delta d)$ . Regions excluded as viable positions for randomly produced wavelength values were the echelle inter-order gaps, zones near identified metal lines, and zones within  $0.03 \text{ \AA}$  of random wavelengths already generated in the current individual simulation. The result, for comoving distance bin sizes of  $5h^{-1} \text{ Mpc}$  and  $10h^{-1} \text{ Mpc}$  is shown in Figure 7.1.

Upon examination of Figure 7.1, especially the lower panel, it appears that almost all of the bins have values of  $|\xi|$  less than the uncertainty estimates produced by the ensemble/bootstrap method described in Section 7.2.2. This may seem unexpected, since the estimates are meant to be  $1\sigma$  uncertainties and even a random distribution should show some deviations greater than this. However, as discussed in Section 7.2.2, the ensemble uncertainties only become accurate when the line distribution is weakly clustered, *i.e.* not random. When  $|\xi| \sim 0$ , as is the case here, the Poisson uncertainties provide better uncertainty estimates. In fact, it is likely that the best uncertainties lie somewhere between the Poisson and ensemble estimates.

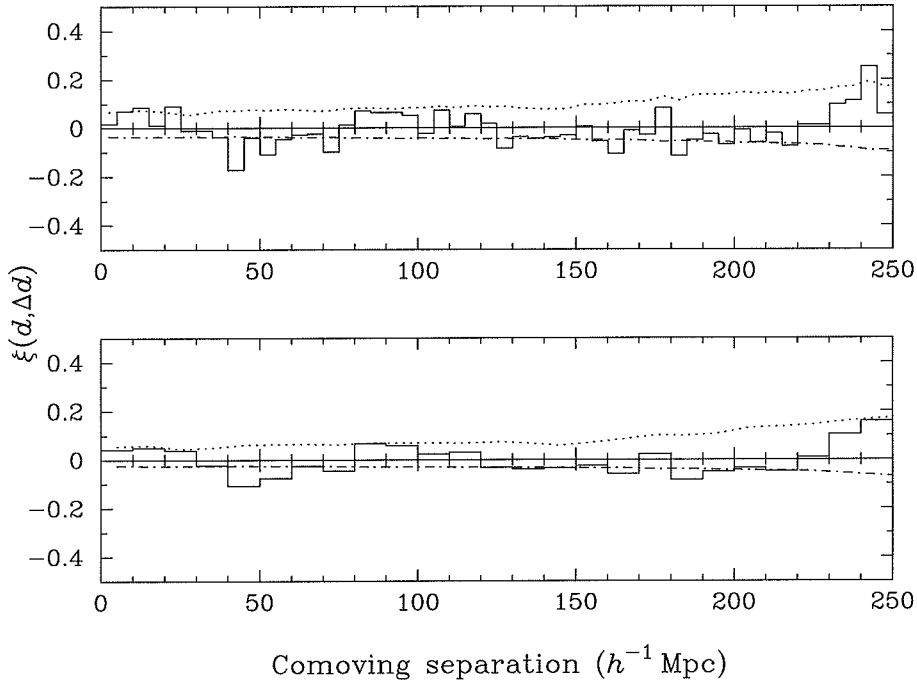


**Figure 7.1** Two point correlation function for the 224 Lyman  $\alpha$  lines in the CNQ. The dotted line shows the  $1\sigma$  uncertainty in  $\xi$  as estimated by a combination of ensemble uncertainties and the bootstrap method, using 200 random trials, as described in Section 7.2.2. The dot-dashed line shows the  $1\sigma$  uncertainty as estimated by Poissonian statistics, plotted as a negative value below the  $\xi$ -axis for clarity. The upper panel has a bin size of  $5h^{-1}$  Mpc; the lower panel has a bin size of  $10h^{-1}$  Mpc.

A Monte Carlo technique was used to estimate the significance of any possible clustering signal in the two-point correlation function. The same number of lines as were detected, 224, were distributed randomly on an echelle format spectrum duplicating the wavelength coverage of the CNQ. The two-point correlation function and  $\chi^2$  value for a bin size of  $5h^{-1}$  Mpc were calculated, and the process repeated many times. The  $\chi^2$  values of these simulations were then compared to the observed  $\chi_{\text{obs}}^2$  to see what fraction satisfied the relation  $\chi^2 \geq \chi_{\text{obs}}^2$ . This fraction would be an estimate of the probability of seeing a two-point correlation function with the observed deviations from  $\xi = 0$  in a random line distribution. It was decided beforehand that a probability  $< 5\%$  would be taken as evidence of a non-random line distribution.

In 10 000 simulations, a total of 2540 met the condition  $\chi^2 \geq \chi_{\text{obs}}^2$ . The probability of seeing the observed deviations from  $\xi = 0$  in a random line distribution is therefore  $\sim 25\%$  and there is no evidence to suggest the distribution is non-Poissonian.

The sample of Lyman  $\alpha$  lines was split into two subsamples of 112 lines each, defined as the subsets of lines with rest-frame equivalent widths  $W_0$  either less than or greater than the median  $W_0$  of  $48.5 \text{ m}\text{\AA}$  respectively. This was done to provide

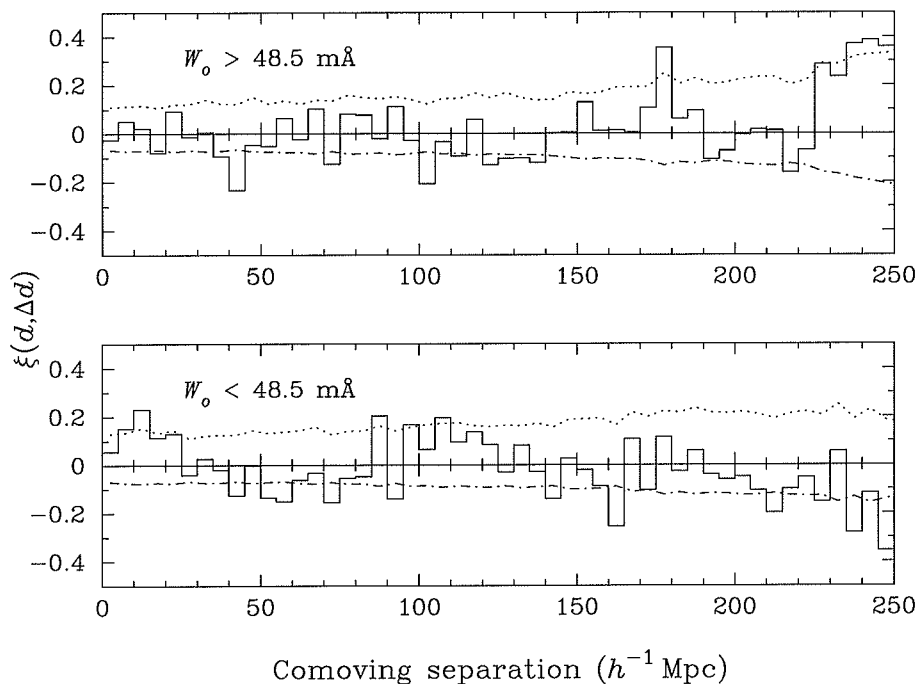


**Figure 7.2** Two point correlation functions for the 112 Lyman  $\alpha$  lines in the CNQ with  $W_0 > 48.5 \text{ m}\text{\AA}$  and  $W_0 < 48.5 \text{ m}\text{\AA}$  respectively. The dotted and dot-dashed lines are as described in Figure 7.1. Both panels have a bin size of  $5h^{-1} \text{ Mpc}$ .

a test for a similar procedure done with the real data—the motivation for doing so is discussed in Section 7.3. For each subsample, 5000 Monte Carlo simulations were used to produce values of  $N_{\text{exp}}(d, \Delta d)$ . The wavelength regions excluded from each simulation were identical to those described above for this object, except for the  $W_0 < 48.5 \text{ m}\text{\AA}$  sample, where zones near the Lyman  $\alpha$  lines included in the  $W_0 > 48.5 \text{ m}\text{\AA}$  sample were also excluded. The results of these calculations are shown in Figure 7.2.

Simulations were again used to estimate the probability of observing correlation functions with magnitudes greater than that seen in the CNQ data. Of 10000 simulations, 5190 had  $\chi^2 \geq \chi_{\text{obs}}^2$  for the  $W_0 > 48.5 \text{ m}\text{\AA}$  sample and 4069 satisfied the same condition for the  $W_0 < 48.5 \text{ m}\text{\AA}$  sample. Therefore the chance probabilities are  $\sim 52\%$  and  $\sim 41\%$  respectively. This shows that, although there appears to be some form of structure in the correlation functions of the subsamples (*e.g.* the peaks at  $\sim 15h^{-1} \text{ Mpc}$  and  $\sim 110h^{-1} \text{ Mpc}$  in the  $W_0 < 48.5 \text{ m}\text{\AA}$  plot), the distribution of Lyman  $\alpha$  lines is consistent with a Poisson distribution.

The result for the full Lyman  $\alpha$  sample implies that there is no significant clustering of Lyman  $\alpha$  lines in the CNQ spectrum. The two subsamples split at the median  $W_0$  also show no evidence of clustering on any scale.

These results agree with the later revelation by Jenkins that the Lyman  $\alpha$  lines

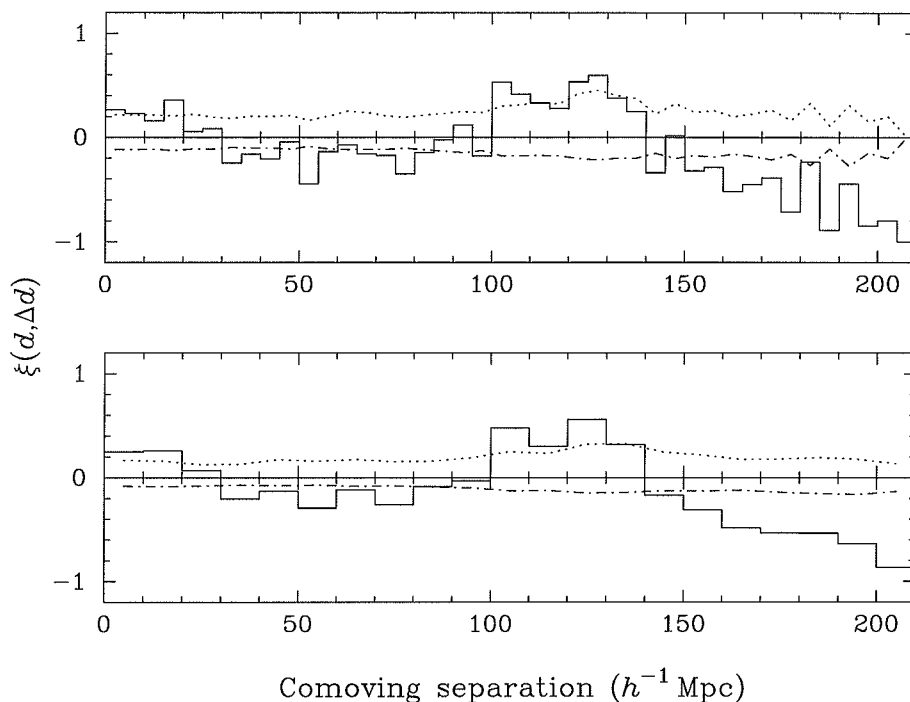


**Figure 7.3** Two-point correlation function for the 63 Lyman  $\alpha$  lines in Q1101–264. The dotted and dot-dashed lines are as described in Figure 7.1. The upper panel has a bin size of  $5h^{-1}$  Mpc; the lower panel has a bin size of  $10h^{-1}$  Mpc.

were distributed randomly according to the density distribution function

$$\frac{\partial^2 \mathcal{N}}{\partial N(\text{HI}) \partial z} = (A_1 N(\text{HI})^{-1.3} + A_2 N(\text{HI})^{-2.0})(1+z)^{2.33}, \quad (7.14)$$

with  $A_1 = 3.156 \times 10^4$  and  $A_2 = 8.436 \times 10^{13}$ . Therefore there is no obvious discrepancy between the results of the correlation function analysis on realistic data and the true clustering properties of the same data. The process of analysing and extracting the Lyman  $\alpha$  lines from a noisy spectrum has not added any spurious clustering features.

### 7.3 Clustering in Q1101–264

In the spectrum of Q1101–264 there are 63 absorption features which have been attributed to Lyman  $\alpha$ . The two-point correlation function for these lines was calculated using 5000 Monte Carlo simulations to generate values of  $N_{\text{exp}}(d, \Delta d)$ . Wavelength regions excluded from the simulations were as described for the CNQ calculation (Section 7.2.3). The resulting correlation function, for comoving distance bin sizes of  $5h^{-1}$  Mpc and  $10h^{-1}$  Mpc is shown in Figure 7.3.

### 7.3.1 Correlation Function Features in Q1101–264

An obvious feature of the two-point correlation function shown in Figure 7.3 is the groupings of consecutive bins in which  $\xi$  is exclusively positive or negative, and often several times the magnitude of the Poissonian uncertainty estimates. This behaviour is in sharp contrast to that observed in the CNQ and Q2206–199N (PHSM), where the value of  $\xi$  changes sign more frequently in adjacent bins and where the Poissonian uncertainties appear to define reasonable  $1\sigma$  deviations from  $\xi = 0$ .

The interpretation of Figure 7.3 is that the Lyman  $\alpha$  cloud distribution appears to be showing structure on scales  $> 100h^{-1}$  Mpc. In particular, the peaks in  $\xi$  at  $< 20h^{-1}$  Mpc and  $\sim 120h^{-1}$  Mpc indicate a large number of cloud pairs with such separations, while the  $\xi < 0$  regions show a relative deficit at the appropriate separations<sup>10</sup>. A natural explanation is that the clouds are clustered into “clumps” along the sightline, each clump  $\sim 20h^{-1}$  Mpc across, and separated by  $\sim 120h^{-1}$  Mpc.

These sizes are similar to clustering scales observed for other objects at the present epoch. Rich clusters of galaxies have correlation scales  $\sim 20h^{-1}$  Mpc and superclusters  $\sim 100h^{-1}$  Mpc (Bahcall, 1988, and references therein). However, the structure seen here is at  $z \sim 2$ , and in objects for which there has only been evidence of weak clustering on scales  $\lesssim 2h^{-1}$  Mpc, with one exception. Mo *et al.* (1992b) used a method based on examining the slope of the two-point correlation function (Mo *et al.*, 1992c) of the Lyman  $\alpha$  lines ( $W_0 \geq 0.36 \text{ \AA}$ ) in the spectra of four QSOs to search for large scale structures. Emphasising the power of their method, Mo *et al.* showed a  $3\sigma$  detection of a characteristic scale of  $\sim 120h^{-1}$  Mpc in the Lyman  $\alpha$  cloud distribution, as well as a  $2\sigma$  detection of a scale of  $\sim 60h^{-1}$  Mpc. The similarity of the  $\sim 120h^{-1}$  Mpc sizes in this study and Mo *et al.*'s is startling.

For the reasons discussed in Section 7.2.2, it is difficult to determine the statistical significance of the clustering signal seen in the correlation function. If the bins with  $100h^{-1} \leq d \leq 140h^{-1}$  Mpc are combined, the resulting value of  $\xi(100h^{-1}, 40h^{-1})$  is 7.6 times the corresponding Poissonian  $1\sigma$  uncertainty estimate and 3.1 times the bootstrap  $1\sigma$  uncertainty estimate, indicating a highly significant clustering detection. These determinations must be treated with caution, although one might expect them to provide upper and lower significance limits, respectively.

The same Monte Carlo technique used for the CNQ data (see Section 7.2.3) was used to better assess the significance of the apparent structure revealed in Figure 7.3. In 10 000 simulations, 219 had  $\chi^2 \geq \chi_{\text{obs}}^2$ . Therefore, the probability that the distribution seen in Figure 7.3 arose by chance is  $\sim 2.2\%$ . Since the bootstrap estimate of  $3.1\sigma$  corresponds to a normal probability of 0.2%, it can be seen that the overall probability of observing the given line distribution is greater than that of seeing the observed values of  $\xi$  in just a few bins selected for their unusual  $\xi$  values (as it should be). The probability is still small, however. Since it is  $< 5\%$ , it is taken as evidence of a non-random (*i.e.* clustered) line distribution.

<sup>10</sup>Note added in revision: This result has now been published in Hunstead *et al.* (1995).

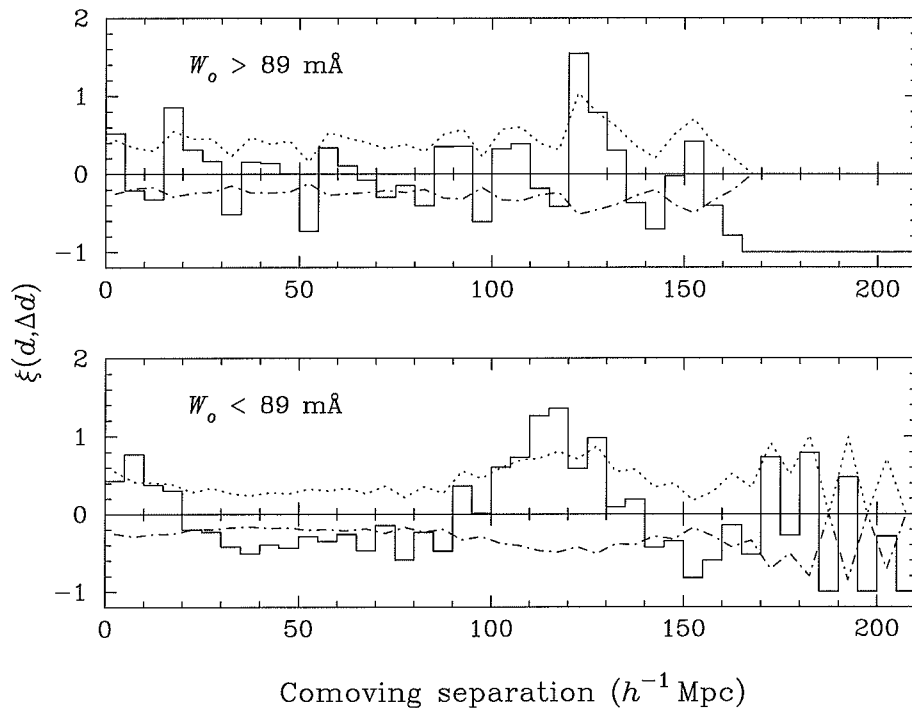


**Figure 7.4** Two point correlation functions for the 32 Lyman  $\alpha$  lines in Q1101–264 with  $W_0 > 89 \text{ m}\text{\AA}$  and 31 lines with  $W_0 < 89 \text{ m}\text{\AA}$  respectively. The dotted and dot-dashed lines are as described in Figure 7.1. Both panels have a bin size of  $5h^{-1} \text{ Mpc}$ .

### Clustering in Equivalent Width Limited Sub-Samples in Q1101–264

At first sight it seems remarkable that such a dramatic clustering signal has not been observed in two-point correlation functions before, since such large scales are adequately probed even by low-resolution spectra. However, most previous clustering analyses have been based on samples of Lyman  $\alpha$  lines which are much stronger than those considered here (typically with equivalent widths  $W_0 \geq 0.36 \text{ \AA}$ ). This implies the features detected in the two-point correlation function may be due mainly to the weak lines in the spectrum.

To test this hypothesis, the sample of 63 Lyman  $\alpha$  lines was divided at the median equivalent width ( $W_0 = 89 \text{ m}\text{\AA}$ ) and the two-point correlation function calculated separately for the two subsamples. In these calculations a correction was made for the fact that weak lines cannot be detected if they fall close to stronger ones (within  $\sim$  half the measured equivalent width) by excluding such regions from the weak line simulations. However, investigation showed this effect made an insignificant overall difference. The resulting correlation functions for the subsamples are shown in Figure 7.4.

The subsample of stronger lines shows little trace of the structure seen in Figure 7.3, whereas the weak line sample shows it clearly. Simulations were again used to assess the significance of the correlation function for both subsamples. For the  $W_0 > 89 \text{ m}\text{\AA}$  sample, 283 of 10 000 simulations yielded values of  $\chi^2 \geq \chi_{\text{obs}}^2$ , giving

a chance probability of  $\sim 2.8\%$ . For the  $W_0 < 89 \text{ m}\text{\AA}$  sample, only 30 of 10 000 simulations gave such a result, giving a best estimate chance probability of  $\sim 0.3\%$ .

The structure in the strong line distribution is significant, but less so than the result using all the lines. The major contribution to the  $\chi_{\text{obs}}^2$  value for this sample comes from the bins at  $d > 160h^{-1} \text{ Mpc}$ , where there are no line pairs (*cf.* Figure 7.5). For the weak line sample, though, the detected clustering is highly significant. It appears that the majority of the clustering signal seen in the Q1101–264 Lyman  $\alpha$  data is due to the weaker lines.

Three apparently contradictory results exist in the literature. Crotts (1989) found significant small-scale clustering in a  $W_0 > 0.4 \text{ \AA}$  sample of Lyman  $\alpha$  lines but none in a  $W_0 > 0.2 \text{ \AA}$  sample. This result was criticised on the grounds of poor statistics by Webb (1989) and Webb and Barcons (1991) found no evidence for clustering in high  $W_0$  subsamples assembled from 20 QSO spectra. The validity of Crotts’s result seems doubtful.

Another claim of structure in the Lyman  $\alpha$  forest was made by Mo *et al.* (1992b), who found *large-scale* structure (as discussed in Section 7.3.1) in a  $W_0 > 0.36 \text{ \AA}$  sample of lines. However, even if this result is correct, it does not necessarily contradict earlier results which found no large-scale structure in the Lyman  $\alpha$  forest. Mo *et al.* state that their analysis method is more sensitive than the two-point correlation function, so it could be that high  $W_0$  lines are clustered, but with a strength below that detectable by using correlation functions on the data available so far. In this case, the correlation function of the strong lines in Q1101–264 should not be expected to show any structure. Mo *et al.*’s result says nothing about weaker lines, so there is no contradiction.

The third result is that of Cristiani *et al.* (1995) (see Section 7.1.1), who found an increased tendency to cluster in high  $W_0$  subsamples from the spectrum of a single QSO. However, as discussed in Section 7.1.1, this result is open to some doubt.

The only published result similar to the one found here is that of Rauch *et al.* (1992), who found evidence for clustering of Lyman  $\alpha$  clouds with  $b \leq 20 \text{ km s}^{-1}$  in the spectrum of Q0014+813 (this paper was described in more detail in Section 7.1.1). A direct comparison with the result presented here is difficult because of Rauch *et al.*’s choice of a velocity dispersion cut-off for their subsample. An inspection of their data shows 47 of their 48 lines with  $b \leq 20 \text{ km s}^{-1}$  have  $W_0 < 100 \text{ m}\text{\AA}$ , but there are many other lines below this equivalent width limit and with  $b > 20 \text{ km s}^{-1}$ . Rauch *et al.*’s subsample is therefore essentially a subset of the lines with  $W_0 < 100 \text{ m}\text{\AA}$ . That this sample reveals significant clustering is support for weaker Lyman  $\alpha$  lines being more strongly clustered than stronger ones.

### Random Shifting of Line Positions

Further tests were done to critically assess the reality of the clustering in the Q1101–264 data. The sample of lines was subjected to a randomising process, in which each line was “shifted” in wavelength by an amount determined by a normally distributed random variable. This was done for a number of choices of the standard

deviation  $\sigma_{\text{shift}}$  of the random variable and the two-point correlation functions of the resulting line positions were calculated.

In both the full line sample and the  $W_0 < 89 \text{ m}\text{\AA}$  sample the correlation signal remained significant for  $\sigma_{\text{shift}} \lesssim 20 \text{ \AA}$ . At  $\sigma_{\text{shift}} \gtrsim 20 \text{ \AA}$  the clustering signal dropped rapidly and became consistent with a Poissonian line distribution. This can be taken to imply that the lines are produced by clouds which are clustered on a scale corresponding to separations of  $\sim 20 \text{ \AA}$ . In terms of comoving distance this is  $\sim 10h^{-1} \text{ Mpc}$ .

### Modelling the Clustering

A simple one-dimensional clustering model was devised and tested to determine some parameters of interest. The model consisted of a uniform random background of Lyman  $\alpha$  clouds, upon which were superimposed clumps of extra clouds with a gaussian distribution in comoving distance. Three model parameters were varied: Clump separation, gaussian  $\sigma$  of clumps, and peak overdensity of the clumps. Correlation functions were calculated using the model as the source of random line positions instead of a uniform deviate. In this way, the best-fitting model would produce a flat correlation function with the real data. The parameter values for the full line sample were found to be:

1. Clump separation =  $(115 \pm 10)h^{-1} \text{ Mpc}$ ;
2. Gaussian  $\sigma$  for each clump =  $(10 \pm 2)h^{-1} \text{ Mpc}$ ;
3. Peak overdensity =  $(3.0 \pm 0.5) \times \text{background}$ .

For the weak line subsample ( $W_0 < 89 \text{ m}\text{\AA}$ ), the first two parameters were unchanged, but the overdensity was now  $5.0 \pm 0.5$ . The characteristic clumping scale  $\sigma$  is consistent with the value of  $\sigma_{\text{shift}} \sim 10h^{-1} \text{ Mpc}$  measured in the subsection *Random Shifting of Line Positions* on page 156. Interestingly, the overdensities are remarkably similar to those of present-day galaxies in superclusters (Bahcall, 1988), though any causal connection between the two is unlikely.

### 7.3.2 Lyman $\alpha$ Line Positions in Q1101–264

Since the simplest interpretation of the correlation function is to postulate that the Lyman  $\alpha$  lines are clumped, the line positions should be scrutinised for any evidence of such clumping. A simple method for doing this is to indicate the positions of the detected lines with tickmarks along a wavelength axis. Further information can be added by making the length of the tickmarks proportional to the equivalent width of the corresponding line. Such a plot is shown in Figure 7.5. In this figure, the lines with  $W_0 < 89 \text{ m}\text{\AA}$  have been separated from those with  $W_0 > 89 \text{ m}\text{\AA}$  by plotting them below the axis.

Two apparent groupings of weak lines can easily be seen in the figure, near 3520 and 3760  $\text{\AA}$ . These groups of lines are at the correct separation of  $\sim 120h^{-1} \text{ Mpc}$ , and are the main cause of the  $\xi > 0$  signal seen in Figure 7.4.

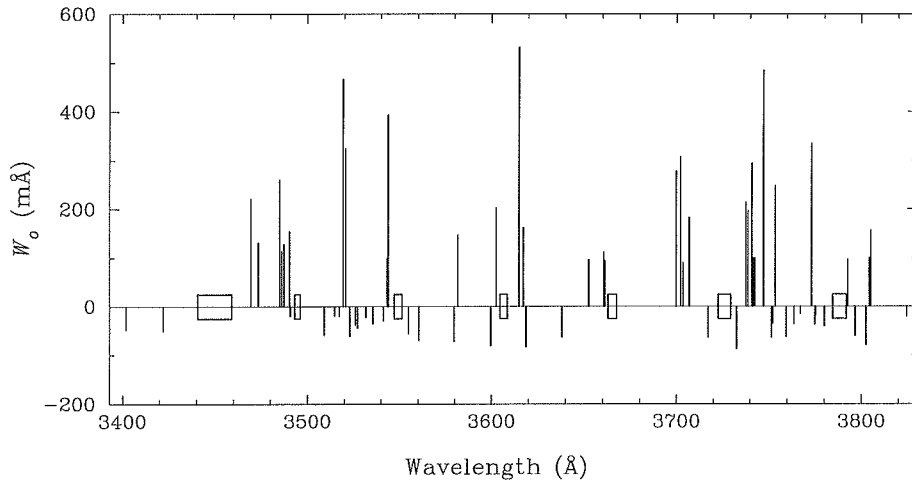


**Figure 7.5** Vertical lines marking the positions of the 63 Lyman  $\alpha$  lines identified in the spectrum of Q1101–264. The length of each line is proportional to the corresponding equivalent width. Lines with equivalent widths smaller than the median value of 89 mÅ have been plotted below the axis. There are no tickmarks on the axis. Open boxes on the wavelength axis indicate the echelle order gaps in the wavelength coverage of the Lyman  $\alpha$  forest as well as the position of the damped Lyman  $\alpha$  absorption at 3450 Å.

However, Figure 7.5 also illustrates the paucity of Lyman  $\alpha$  lines in the spectrum, emphasising the fact that the numbers are too small to produce very reliable statistics. This is especially so when the sample is split into the two subsamples. The full 63 line sample contains 1953 line pairs, but the  $W_0 < 89$  mÅ sample (31 lines) only contains 465 pairs.

While it is useful to examine the line positions visually to confirm the appearance of line clumps implied by the correlation function, one must be careful of arriving at conclusions based on such an inspection. Bechtold and Schectman (1989) have pointed out, in a similar context, that the human eye and brain are unreliable at distinguishing pattern and randomness. A purely Poissonian distribution of line positions can contain what appear to be significant clumps and voids of lines. This is illustrated in Figure 7.6, which shows ten instances of 63 lines positioned by a uniform random deviate between limits of 0 and 1. Several large “voids” can be seen, the largest covering  $\sim 11\%$  of the interval, as well as several tight groupings of many lines<sup>11</sup>. Such features are to be expected in random data—a conspicuous *lack* of them is also an indication of underlying structure (*e.g.* in a regular lattice arrangement). Judging the line positions seen in Figure 7.5 by eye is therefore only a secondary step, and no conclusions should be drawn without referring to the correlation function.

<sup>11</sup>Any other “patterns” which the viewer may detect in the Figure 7.6 are also simply the product of the random process. Particularly striking to me are diagonal strips of voids—other viewers may see other curious features. Finding order within chaos seems to be something in which the human mind excels.

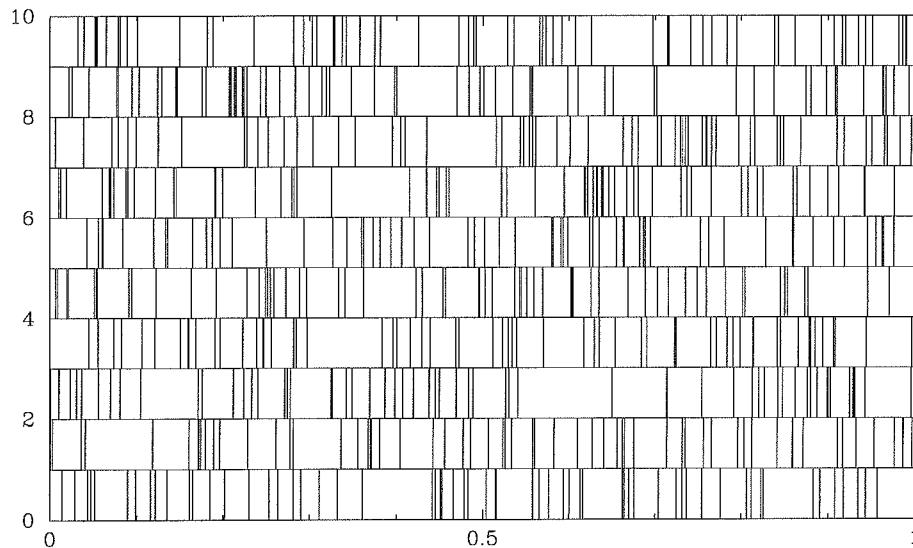


**Figure 7.6** Ten instances of random line positions, stacked vertically. Each strip shows 63 lines, positioned according to a uniform random deviate.

### 7.3.3 Discussion of Q1101–264 Clustering Result

The correlation function analyses show that the line distribution in the spectrum of Q1101–264 is highly non-random. Interpreting this result requires careful consideration. There are three different possibilities:

- The positive correlation signal is merely a statistical fluctuation. The probabilities calculated in Section 7.3 show how likely this is.
- The correlation function reveals a characteristic clustering scale in the Lyman  $\alpha$  forest cloud population.
- The clumping of clouds traces non-uniformities in the intergalactic ionising background radiation.

While clustering is a common phenomenon in astronomy, and there are now several pieces of evidence for clustering of Lyman  $\alpha$  forest clouds on small scales (Webb, 1987; Barcons and Webb, 1991; Cristiani *et al.*, 1995)<sup>12</sup>, finding groups of clouds separated by over  $100h^{-1}$  Mpc is astonishing.

The fact that the two-point correlation signal is strongest for the weaker lines in Q1101–264 is particularly surprising, if interpreted as gravitational clustering. Cristiani *et al.* (1995) found an opposite result in the spectrum of Q0055–269: Clouds with high  $N(\text{HI})$  were more strongly clustered than would be expected for gravitational clustering. The results presented here do not fit easily into such a scenario. However, as discussed in Section 7.1.1, the interpretation of Cristiani *et al.*'s results is questionable.

A more successful hypothesis for explaining the results derived here is that the distribution of clouds somehow traces the distribution of ionising radiation. Regions

<sup>12</sup>Although these findings are open to some criticism; see Section 7.1.1.

of relatively high radiation intensity will contain clouds with higher ionisation levels than those in areas of lower radiation. This can lead to inhomogeneities in the spatial distribution of  $N(\text{HI})$ .

A simplistic scenario is to imagine all Lyman  $\alpha$  clouds contain the same mass of hydrogen. In this case, clouds in high radiation areas will be highly ionised and so have relatively low neutral fractions, making the measurable quantity  $N(\text{HI})$  lower than that for clouds in low radiation zones. If this is true, clumps of low  $N(\text{HI})$  clouds would trace regions of enhanced ionising radiation—perhaps galaxy clusters or the immediate neighbourhoods of luminous QSOs.

This argument has several problems. Firstly, a situation where all astronomical objects from a class are produced with identical masses is highly artificial. Masses are more likely to range over an order of magnitude or more. Secondly, a higher photoionisation level would imply a higher temperature for the low  $N(\text{HI})$  clouds. Such a trend is not seen; in fact there is some evidence to suggest low  $N(\text{HI})$  clouds have lower mean temperatures than higher  $N(\text{HI})$  clouds (see Section 6.4).

So it appears likely that clouds with low  $N(\text{HI})$  may be genuinely less massive than high  $N(\text{HI})$  clouds. Less massive clouds are more easily ionised, because of a lack of interior shielding, and so would be expected to become fully ionised in regions of enhanced radiation, and therefore undetectable. In this picture, regions of increased ionising flux would be characterised by an underabundance of weakly absorbing clouds and, conversely, clumps of such clouds would trace regions of decreased radiation. Such areas would be voids in the distribution of luminous objects such as galaxies and QSOs.

Another observation in favour of this interpretation is the apparent lack of redshift evolution in the number density of weak lines between  $z \sim 2$  and  $z \sim 0$  (Section 6.3). This implies that the low  $N(\text{HI})$  clouds are relatively quiescent, which is more likely if they inhabit regions devoid of strong radiation sources. The higher  $N(\text{HI})$  lines, on the other hand, may inhabit areas close to strong ionising radiation sources or gravitational potentials, and be ionised, dissipated, or collapsed over time, resulting in the steep redshift evolution of such clouds.

It is also worthwhile noting the conclusions of Pierre *et al.* (1988), who studied the possibility that the weak clustering seen by Webb (1987) could be caused by a cloud distribution which has subsequently evolved to resemble the galaxy distribution seen at low redshift. They showed that the “cell walls”, in which galaxies were distributed in the CfA redshift survey (de Lapparent *et al.*, 1986; de Lapparent *et al.*, 1988), were too thin to produce the weak correlation function signal seen by Webb. A model with unrealistically thick cell walls, or small void sizes, was required to reproduce Webb’s result. Pierre *et al.* concluded that either the structures had evolved substantially between  $z \sim 2$  and  $z \sim 0$ , or that the Lyman  $\alpha$  clouds did not lie on cell walls in the same way as galaxies. This can be interpreted as evidence that the Lyman  $\alpha$  clouds inhabit the voids in the galaxy distribution, perhaps instead of the cell walls.

In the spectrum of Q1101–264 there are remarkably few Lyman  $\alpha$  lines. If the cause of the clustering signal is not an overdensity of clouds in some places, but

rather an underdensity elsewhere, then it may be that the sightline intercepts areas with unusually high levels of ionising radiation.

A search of the QSO catalogue by Hewitt and Burbidge (1993) was conducted for other QSOs with small angular separations from Q1101–264. Such objects, if they existed, could produce enhanced ionisation in regions along the sightline (such behaviour has been witnessed in the spectrum of Q0302–003 by Dobrzycki and Bechtold (1991)). No QSOs were found in the catalogue closer than six degrees from Q1101–264, far too great a distance from the sightline to have a significant effect. However, it is highly possible that QSOs closer to the sightline have not yet been detected. Also, at the gas densities indicated by the standard models of the Lyman  $\alpha$  clouds ( $n(\text{H}) \sim 10^{-4} \text{ cm}^{-3}$ ) the recombination time is long enough that clouds would remain ionised long after the radiation source had faded. The simple explanation of QSO-induced ionisation cannot therefore be ruled out.

Another interesting possibility is that the low  $N(\text{HI})$  clouds are associated with galaxies. Generally it has been assumed that galaxy haloes would give rise to absorption systems with high  $N(\text{HI})$ , but Morris and van den Bergh (1994) showed that low- $N$  absorbers could be produced in tidal debris in small clusters of galaxies. Such a population of absorbers would show similar clustering properties to galaxies. However, Morris and van den Bergh state that such tidal debris is built up over a Hubble time, so it may be unable to account for absorbers at  $z_{\text{abs}} \sim 2$ .

## 7.4 Clustering in Q2348–147

In the spectrum of Q2348–147 there are 325 absorption features which have been attributed to Lyman  $\alpha$ . The two-point correlation function for these lines was calculated using 5000 Monte Carlo simulations to generate values of  $N_{\text{exp}}(d, \Delta d)$ . Wavelength regions excluded from the simulations were as described for the CNQ calculation (Section 7.2.3). The resulting correlation function, for comoving distance bin sizes of  $5h^{-1} \text{ Mpc}$  and  $10h^{-1} \text{ Mpc}$  is shown in Figure 7.7.

The same Monte Carlo technique used for the CNQ data (see Section 7.2.3) was used to assess the significance of any structure present in Figure 7.7. In 10 000 simulations, 2614 had  $\chi^2 \geq \chi_{\text{obs}}^2$ , so the probability that the distribution seen in Figure 7.3 arose by chance is  $\sim 26\%$ . There is therefore no evidence that the Lyman  $\alpha$  line distribution in the spectrum of Q2348–147 is non-random.

### Equivalent Width Limited Sub-Samples in Q2348–147

Although no clustering signal was detected in the full Lyman  $\alpha$  line sample for Q2348–147, it was still possible that the weaker lines were clumped in a manner similar to that observed in Q1101–264. To test this, the Lyman  $\alpha$  sample was divided at the median equivalent width ( $W_0 = 95 \text{ m}\text{\AA}$ , close to the Q1101–264 median of  $W_0 = 89 \text{ m}\text{\AA}$ ) and the correlation functions of the two subsamples were calculated. The results are shown in Figure 7.8.

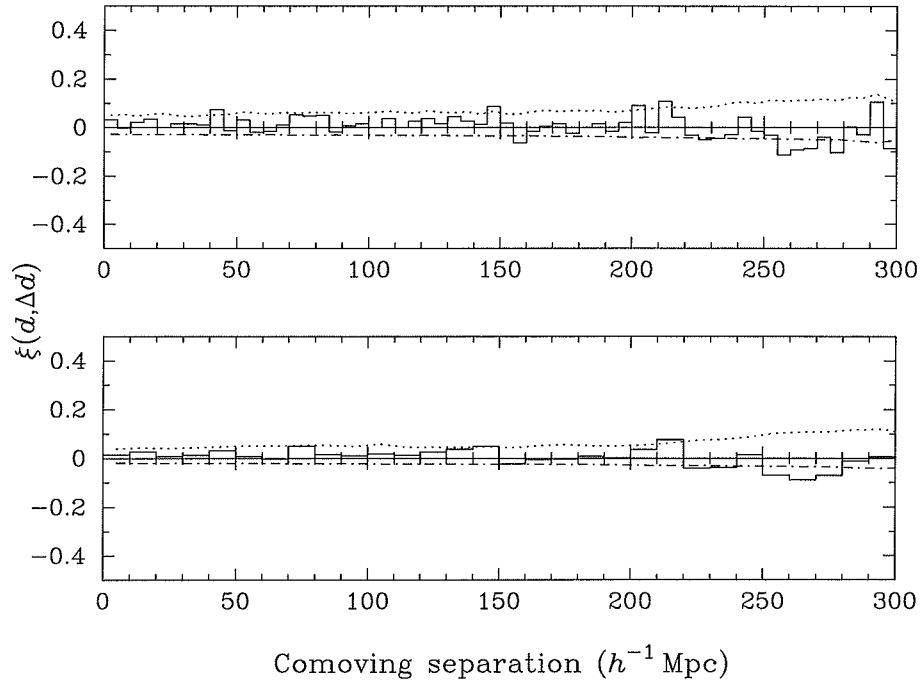


**Figure 7.7** Two point correlation function for the 325 Lyman  $\alpha$  lines in Q2348–147. The dotted and dot-dashed lines and bin sizes are as described in Figure 7.1.

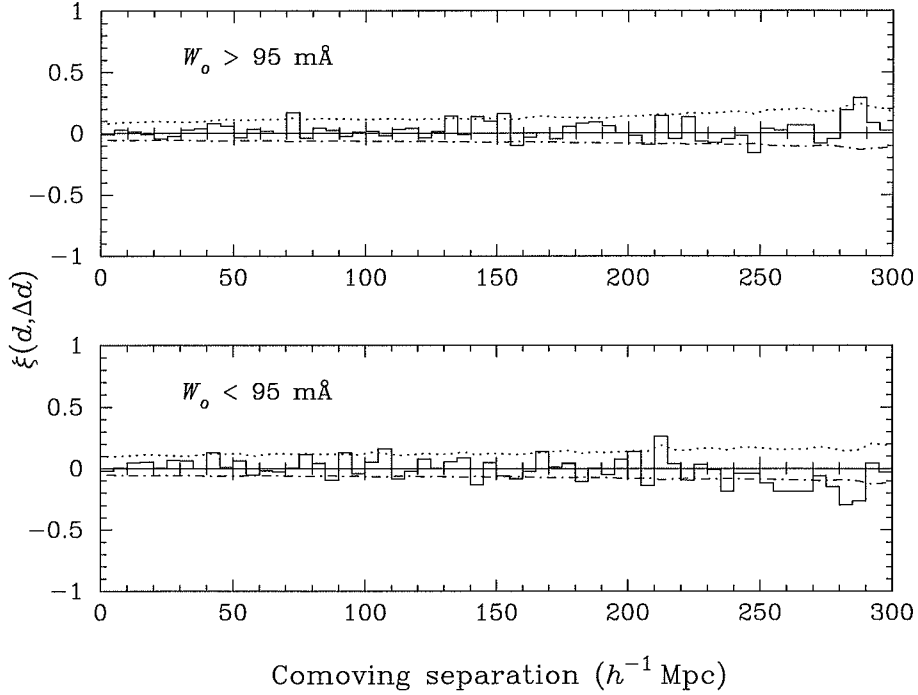


**Figure 7.8** Two point correlation functions for the 162 Lyman  $\alpha$  lines in Q2348–147 with  $W_0 > 95 \text{ mÅ}$  and 163 lines with  $W_0 < 95 \text{ mÅ}$  respectively. The dotted and dot-dashed lines are as described in Figure 7.1. The bin size is  $5h^{-1} \text{ Mpc}$ .

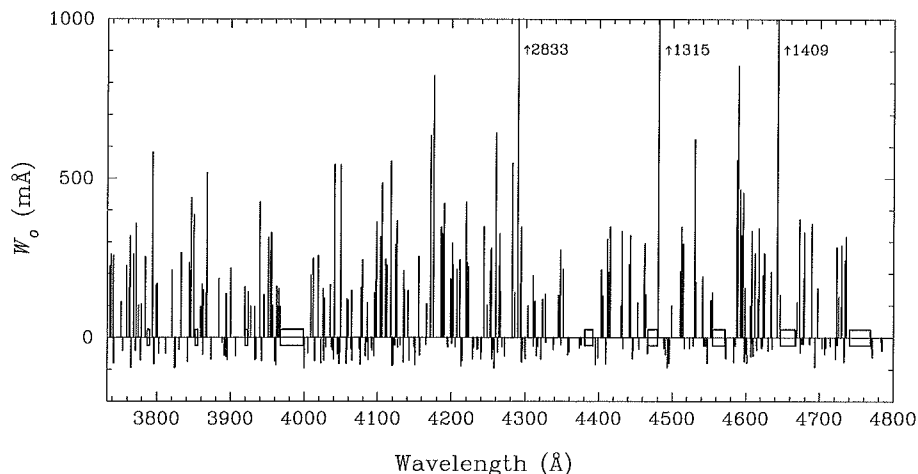


**Figure 7.9** Vertical lines marking the positions of the 325 Lyman  $\alpha$  lines identified in the spectrum of Q2348–147. The length of each line is proportional to the corresponding equivalent width. Lines with equivalent widths smaller than the median value of 95 mÅ have been plotted below the zero level. The equivalent widths of the three lines with  $W_0 > 1000$  mÅ are marked. There are no tickmarks on the axis. Open boxes on the wavelength axis indicate the echelle order gaps and the position of the damped Lyman  $\alpha$  absorption at 3990 Å. Note the wavelength coverage is complete between 4000–4380 Å.

Simulations were again used to estimate significance levels. A total of 5871 out of 10 000 simulations yielded values of  $\chi^2 \geq \chi_{\text{obs}}^2$  in the  $W_0 > 95$  mÅ sample, giving a chance probability of  $\sim 59\%$ . For the  $W_0 < 95$  mÅ sample, 2391 out of 10 000 simulations gave the same result, giving a probability of  $\sim 24\%$ . There is therefore no evidence of a non-random line distribution in either subsample.

#### 7.4.1 Lyman $\alpha$ Line Positions in Q2348–147

Following the procedure for Q1101–264 (Figure 7.5), a plot of the Lyman  $\alpha$  line positions and equivalent widths in Q2348–147 was produced. This is shown in Figure 7.9.

In this case there are some small voids and clumps apparent, but nothing as obvious as the groupings seen in Figure 7.5. However, for the reasons presented in Section 7.3.2, no conclusions will be drawn from this plot.

#### 7.4.2 Discussion of Q2348–147 Clustering Result

The apparently random distribution of the Lyman  $\alpha$  clouds along the line of sight to Q2348–147 is an interesting counterpoint to the strong evidence for clustering seen in the spectrum of Q1101–264.

The large number of lines in the Q2348–147 spectrum ( $> 5$  times the number seen in the spectrum of Q1101–264) makes it a more sensitive probe of clustering than Q1101–264. However, the Q2348–147 spectrum covers a higher redshift range

than that of Q1101–264: 2.1–2.9 compared to 1.8–2.2. Clustering of objects is expected to increase with time, so it is not surprising if higher redshift data shows less evidence of structure.

Another factor to consider is that individual sightlines may not adequately probe typical volumes of space. If the Q1101–264 sightline covers an unusual region of space, where large “bubbles” of enhanced background ionisation exist, for example, then it is not surprising that other sightlines do not show similar structures. The difficulties of using a small number of sightlines to determine large-scale properties of the matter distribution are discussed further in Section 8.2.

## 7.5 Summary

The spectra of Q1101–264 and Q2348–147 have been examined for any evidence of clustering among the Lyman  $\alpha$  clouds in their sightlines. A careful calculation of the two-point correlation functions showed evidence for a non-random distribution of the clouds along the line of sight to Q1101–264.

The sample of Lyman  $\alpha$  lines from the spectrum of Q1101–264 was divided at the median equivalent width and the lines with  $W_0 < 89 \text{ m}\text{\AA}$  were found to be responsible for most of the clustering signal seen in the correlation function. Monte Carlo simulations showed the probability of observing a correlation function  $\chi^2$  value greater than the observed  $\chi_{\text{obs}}^2$  in a sample of randomly distributed lines was  $\sim 0.3\%$ . The observations were found to be consistent with a clustering model in which gaussian clumps of Lyman  $\alpha$  clouds with  $\sigma = (10 \pm 2)h^{-1} \text{ Mpc}$  and overdensity  $3.0 \pm 0.5$  separated by  $(115 \pm 10)h^{-1} \text{ Mpc}$  were superposed on a random background distribution.

A scenario in which these observations reveal gravitational clustering of the Lyman  $\alpha$  clouds seems unlikely, since higher equivalent width clouds might be expected to have higher mass and therefore cluster more strongly than low  $W_0$  clouds. A more plausible explanation is that regions with an underabundance of low  $W_0$  clouds trace enhanced background ionising flux, possibly caused by the presence of sources such as QSOs. This is consistent with the idea that the clumps of low  $W_0$  clouds exist in voids in the galaxy distribution—areas far removed from the cell walls in which most galaxies are seen to be distributed at  $z \sim 0$ .

The spectrum of Q2348–147 showed no evidence for a non-random distribution of Lyman  $\alpha$  clouds along its line of sight. This may have been because the clustering detected in the spectrum of Q1101–264 was much less pronounced at the higher redshift of the Q2348–147 spectrum, or more likely because the regions of space probed by the sightlines do not form an adequate sampling of structures on large scales.

Further studies of the spatial Lyman  $\alpha$  cloud distribution are needed before any firm conclusions can be reached on the clustering properties of the clouds.